Université catholique de Louvain

Ecole Polytechnique de Louvain

Institute of condensed matter and nanoscience

Manufacturing and magnetic force microscopy characterization of magnetic nanowires and nanotubes

Thèse présentée en vue de l'obtention du grade

de docteur en sciences de l'ingénieur par

Muhammad Ramzan Tabasum

Membres du Jury :

Prof. Jacques Devaux, UCL, Chairman
Prof. Bernard Nysten, UCL, Co-supervisor
Prof. Luc Piraux, UCL, Co-supervisor
Prof. Alain Jonas, UCL
Prof. Benoit Hackens, UCL
Prof. Armando Encinas, San Luis Potosi, Mexico
Dr. Fatih Zighem, Université Paris 13, France

Louvain-la-Neuve: 21-08-2015

اَللّٰهُمَّ صَلِّ عَلٰى سَيِّدِنَا مُحَمَّدٍ النَّبِيِّ الْأُمِّيِّ وَعَلٰى
اٰلِهٖ وَسَلِّمْ تَسْلِيْمًا.

Acknowledgements

First and foremost I would like to thank Allah Almighty for making my dream come true. You give me the power (patience, health and wisdom) to believe in my passion and pursue my ambitions.

I want to pay sincere thanks to both Prof. Bernard Nysten and Prof. Luc Piraux who together made it possible for me to spend these precious five years in the lab with all its benefits, where I did learn so much not only about science but also life in general. My first person of contact at Université catholique de Louvain (UCL) was Prof. Alain Jonas. How I came in contact with him? The history of this PhD thesis dates back to winning the region's best student award (1999) while studying at Danish Public School in district Sialkot. This passion of winning and be the best led to an extra ordinary career achievement- two gold medals for best performance in materials engineering from university of engineering and technology (UET), Lahore, Pakistan.

As I was teaching at one of the UET's campuses (2007-2008), the curiosity to learn further not only the new technologies but also new cultures, traditions and languages motivated me to secure the European Commission's Erasmus Mundus grant to follow two years master program in functionalized advance materials engineering (FAME). The first year of my master, out of two years mobility program, was at university of Augsburg (Germany). Then for the second year of master, out of seven institutions of the FAME consortium, I chose to come to UCL. I was put in contact with Prof. Alain Jonas who is coordinator of FAME master.

I had the possibility of following academic courses at UCL and worked in interuniversity microelectronic center (IMEC) for my master thesis under the academic supervision of Prof. Bernard Nysten. Once FAME masters successfully finished, I got offers from institutes such as TU Delft and KU Leuven to pursue my PhD, I preferred to stay and worked under the supervision of Prof. Bernard Nsyten. I was confident that although I don't have hands-on experience of using the core instrument of my project i.e. magnetic force microscopy (MFM), he is someone who would guide me in a disciplined and motivating way. He has been an advisor who gave me the freedom to pursue what I think is important in my research, but at the same time, always being available when I need his expertise. This

achievement (PhD) proved that I was absolutely good at my choice. Before I use the characterizing instrument, I must have something to characterize. Prof. Luc Piraux was a helping hand to provide me the samples from his precious treasure and to put me in contact with people expert in nano manufacturing.

This work would have not been on track smoothly without the scientific involvement and friendly behavior of Dr. Fatih Zighem. I would rather say he is more than a researcher for me (official witness of my marriage if he didn't forget about it!). I am particularly indebted for his patience when explaining experimental procedures to me and pointing out which of them could be significantly used (and how!).The realization and completion of this project was only possible as a result of an excellent support from him as many of my experiments were done under his guidance. For many interesting and exciting discussions about various possibilities I want to thank Prof. Armando Encinas (Mexico).

I cannot forget my colleagues of the institute IMCN who always maintained a cheerful environment. They were always there to explain some technical or administrative stuff along with helping me improve my level of French language in a tender and polite way, *Merci!* When it comes to the Pakistani friends in Belgium, their amiable behavior and nice company enriched my social circle and never let me feel lonely. Another important part of my life at UCL during these years was spent at Islamic cultural center of Louvain-la-neuve where I felt the real meaning of Islamic brotherhood. There have been so many nice people on my way during these years, in order to not forget anyone, names of the colleagues and friends haven't been mentioned on purpose. During these five years I realized that although the experimental work of the research is done by the PhD student to finalize a thesis but love, support and encouragement from family, friends and colleagues is part and parcel for success.

I would also like to thank Jury president, Prof. Jacques Devaux and jury secretary Prof. Benoit Hackens along with my examiners Prof. Alain Jonas and Prof. Armando Encinas. Their encouraging remarks and constructive feedback helped me improve not only the technical contents but also the presentation of the text. Reviewing a thesis is a mammoth task and I am very grateful for thoughtful and detailed comments from my supervisors and from the rest of the jury.

Special thanks to Université catholique de Louvain (UCL) for awarding me the teaching assistant position (to teach and do research simultaneously). I would also like to thank University of Engineering and Technology (UET) Lahore, Pakistan, to offer me the higher studies leave to follow the FAME master and then to do PhD.

To my mother in the Heavens: I am speechless! I can barely find the words to express all the wisdom, love and support you've given me. You were number one fan of all my accomplishments and for that I am eternally grateful. My father, who himself is not an engineer, worked with engineers in Middle East when I was young. He has consistently been an inspiration to me and has encouraged me in all of my endeavors. If I am blessed to live long enough, I hope I will be as good as both of them to my children.

To my wife and children: What can I say? You are one of the main reasons that it was always GREAT during these years in Europe away from my homeland. Your sweet voices helped me overcome many of the daily fatigues. Dear wify, I am so thankful that you were with me. You are unique. Very special thanks to my parents and siblings for their faith in me and letting me pursue my dreams as I wanted. I should especially mention my sister Farzana, she is younger but full of wisdom to support me morally. I Love You Always & Forever!

Muhamamd Ramzan Tabasum

Summary

The rapid development of *Nanotechnology* that tends to progressively replace present systems with novel miniaturized devices based on nano-objects induces an increasing demand for new types of nanomaterials with different structures and improved physical properties. This leads, along with other conceivable candidates, to the production of magnetic nanowires (NWs) and nanotubes (NTs) with unique magnetic properties. These nanomaterials have potential applications in microwave devices, chemical sensors, high density data storage devices, light emitters, etc... They also got an enormous attraction in biological and biomedical applications e.g. for hyperthermia usage to treat cancer cells.

When it comes to the application of NW or NT arrays for data storage, there is a basic need of understanding and controlling the magnetization behavior and reversal process. In the present work, magnetic force microscopy (MFM) has been used to characterize low and medium packing density arrays of magnetic NWs and NTs manufactured by electrodeposition in nanoporous polycarbonate membranes. This was realized using a modified MFM setup allowing *in-situ* and *in-field* measurements.

The influence of the material and geometrical parameters (composition, diameter, shape) on the magnetization reversal process was studied. It is demonstrated that in low density arrays, the dipolar interaction is negligible and that the switching field distribution broadening is mainly due to intrinsic parameters such as the size (diameter) distribution of the NWs. MFM also allows observing the magnetic reversal of individual NWs. This provides detailed information on the local dependence of the dipolar interaction on the inter-wire distance at the nanoscale, which cannot be done by standard magnetometry techniques.

Table of contents

List of symbols and abbreviations

1D	Uni-dimensional
2D	Bi-dimensional or two-dimensional
A	Exchange stiffness constant
A_1	Vibration amplitude of a cantilever
A_0	Free vibration amplitude of a cantilever
AAO	Anodized alumina
AFM	AFM Atomic Force Microscopy
AM-AFM	Amplitude-Modulated Atomic Force microscopy
AGFM	Alternating gradient force magnetometer
ALD	Atomic layer deposition
B_z	Local magnetic induction of the sample
D	Diameter
D_{cr}	Critical diameter
DCD	Direct current demagnetization
ΔE	Energy barrier
E_{ex}	Exchange energy
E_H	Zeeman energy
E_{MC}	Magnetocrystalline energy
E_{ME}	Magentoelastic energy
E_{MS}	Magnetostatic energy
f	Thermal attempt frequency
F_{mag}	Magnetic force on tip apex
FM	Ferromagnetic
FEMM	Finite element micromagnetic
FORC	First order reversal curves
H	External applied field

H_0	Zero external applied field
H_c	Coercive field
H_d^0	Field value at 0 for normalized DCD curve
H_{dip}	Dipolar field
$H_r^{0.5}$	Field value at 0.5 for normalized IRM curve
H_u	Interaction field
HDD	Hard disk drive
l_D	Interwire distance
IF	Interaction field
IRM	Isothermal remanent magnetization
J_{IJ}	Exchange integral
K_1	Magnetocrystalline anisotropy constant
K_u	Uniaxial anisotropy constant
L	Length of NT/NW
l_{ex}	Exchange length
MFM	Magnetic force microscopy
M_r	Remanent magnetization
M_s	Saturation magnetization
m_t	Magnetization of the tip
N	Number of nearest neighbours
N_a	Demagnetizing factor along a-axis
N_c	Demagnetizing factor along c-axis
n_{down}	Number of wires magnetized along $-O_z$
NIST	National institute of standard and technology
NMAG	Micromagnetic simulation package
NWs	Nanowires
NTs	Nanotubes
n_{up}	Number of wires magnetized along $+O_z$

$+O_z$	Upwards field/magnetization direction along Z axis
$-O_z$	Downwards field/magnetization direction along Z axis
P	Porosity/Packing density
PC	Polycarbonate
Q	Quality factor of a harmonic oscillator or resonance peak
SEM	Scanning electron microscope
SFD	Switching field distribution
SQUID	Superconducting quantum interference device
STM	Scanning Tunnelling Microscopy
U_{mag}	Magnetic potential
VSM	Vibrating sample magnetometer
YIG	Yttrium iron garnet
α	Theoretical interaction field
β	Ratio of internal and external tube raddi
σ_D	Standard diameter deviation
K_i	Spring constant
k_B	Boltzman constant
Φ	Phase shift
δ_{SFD}	SFD width
δ_{wall}	Domain wall width

Scientific output and awards

Book chapter

Muhammad Ramzan Tabasum, Fatih Zighem, Luc Piraux and Bernard Nysten, *Magnetic Force Microscopy Characterization of Magnetic Nanowires and Nanotubes,* Springer Book series on magnetic characterization of nanomaterials, 6th Volume, accepted, expected publication- fall 2015.

Publications

1. **M.R. Tabasum**., F. Zighem, JDLT Medina, L. Piraux, B. Nysten, Intrinsic Switching Field Distribution of Arrays of $Ni_{80}Fe_{20}$ Nanowires Probed by In Situ Magnetic Force Microscopy. J. Superconduct. Novel Magn., 26, 1375 (2013).
2. **M. R. Tabasum**., F. Zighem, JDLT Medina, A Encinas, L Piraux and B Nysten, Magnetic force microscopy study of the switching field distribution of low density arrays of single domain magnetic nanowires, J. Appl. Phys 113, 183908 (2013).
3. **M. R. Tabasum**., F. Zighem, JDLT Medina, A. Encinas, L. Piraux and B. Nysten, Magnetic force microscopy investigation of arrays of nickel nanowires and nanotubes, Nanotechnology 25, 245707 (2014).
4. **M. R. Tabasum**., L. Piraux and B. Nysten, A review: Recent advances in magnetic force microscopy characterization of nanodots, nanowires and nanotubes, To be submitted, Nanoscale (2015).
5. **M. R. Tabasum**., A. Encinas, F. Zighem, J. M. Martinez-Huerta, L. Piraux and B. Nysten, Quantitative measurement of interaction field at nanoscale by single nanowire switching using Magnetic Force Microscopy, To be submitted, Small (2015).
6. Y.G. Velazquez-Galvan, A. L. Guerrero-Serrano, J. M. Martınez-Huerta, E. Araujo, **M. R. Tabasum**, B. Nysten, L. Piraux, and A. Encinas, Relation between the coercive and interaction field distributions in the first order reversal curve diagrams of magnetic nanowire arrays, To be submitted, J. Appl. Phys (2015).
7. J. M. Martinez-Huerta, A. Encinas, **M. R. Tabasum**, and L. Piraux, Mean field interaction parameters in first order reversal curves, In preparation.
8. Coulon, A., **M. R. Tabasum**., L. Piraux and B. Nysten, Resolution of commercially available tips for high density nanowire arrays in PC templates, In preparation.

International conference communications

1. M.R. Tabasum, F. Zighem, J. De La Torre Medina, L. Piraux and B. Nysten, *Measuring Switching Field Distribution of Arrays of Mono Domain Magnetic Nanowires Using Magnetic Force Microscopy*, International conference on superconductivity and magnetism (ICSM 2012), April 29-May 4, 2012, **Istanbul, Turkey.**
2. M. R. Tabasum, F. Zighem, J. De La Torre Medina, L. Piraux and B. Nysten, *Intrinsic switching field distribution of arrays of $Ni_{80}Fe_{20}$ nanowires using in situ magnetic force microscopy,* IEEE International Magnetics Conference, INTERMAG 2012, May 7-11, 2012, **Vancouver, Canada.**
3. M. R. Tabasum, F. Zighem, J. De La Torre Medina, L. Piraux and B. Nysten, *Magnetization reversal of ferromagnetic nanowires: a magnetic force microscopy and micromagnetic simulations study*, International Workshop on Magnetic Materials and Nanomaterials MMN'2012, September 04-06, 2012, **Boumerdes, Algeria.**
4. M. R. Tabasum, F. Zighem, J. De La Torre Medina, L. Piraux and B. Nysten, *Magnetic Force Microscopy Study of the Magnetization Reversal in Isolated Nanowires*, Forum des microscopies à sondes locales 2013, 12-16 March 2013, **l'Abbaye de St Jacut de la Mer, France.**
5. M. R. Tabasum, F. Zighem, L. Piraux and B. Nysten, *Renversement de l'aimantation dans des réseaux de nanotubes et nanofils ferromagnétiques de Nickel*, Forum des microscopies à sondes locales 2013, 25-29 march 2013, **Spa, Belgium.**
6. M. R. Tabasum, F. Zighem, L. Piraux and B. Nysten, *A comparative MFM study of the switching behavior of Ni nanotubes and nanowires,* E-MRS 2013 SPRING MEETING, May 27-31, 2013, **Strasbourg, France.**
7. M. R. Tabasum, F. Zighem, J. De La Torre Medina, A. Encinas, L. Piraux and B. Nysten *Measuring Switching Field Distribution of Arrays of Mono Domain Magnetic Nanowires Using Magnetic Force Microscopy*, Euro-Asian Symposium "Trends in MAGnetism": Nanomagnetism, 15^{th}-21^{st} September 2013 Russky Island, **Vladivostok, Russia**.
8. M. R. Tabasum, F. Zighem, L. Piraux and B. Nysten, *MFM investigation arrays of Ni nanotubes and nanowires,* International conference on nanoscience and nanotechnology, ICN+T 2014, July 20-25, 2014, **Vail, Colorado, USA.**
9. M. R. Tabasum, F. Zighem, L. Piraux and B. Nysten, *MFM investigation arrays of Ni nanotubes and nanowires,* International microscopy congress, IMC 2014, September 7-12, 2014, **Prague, Czech Republic.**
10. M.R Tabasum, A. Encinas, J. M. Martinez-Huerta L. Piraux and B. Nysten, *Quantitative measurement of interaction field at nanoscale by single nanowire switching using Magnetic Force Microscopy,* International workshop on magnetic nanowires and nanotubes, IWMNN 2015, May 17-20, 2015, **Meersburg, Germany.**

Awards

1. Young scientist award E-MRS 2013, spring meeting, May 27-31, 2013, Strasbourg, France.
2. Invited young researcher at IV World materials summit, organized by European Materials Research Society, E-MRS, 2013.
3. Featured article and selected image for the front cover of the high impact journal, Nanotechnology, Volume 25, 2014.
4. Best presentation on PhD student day, institute of condensed matter and nanoscience (IMCN), Université catholique de Louvain, 2014.
5. Selected “Talent in the spotlight” for NRG magazine on presenting innovative idea at European NRG Battle, Groningen, Netherlands, 2014.
6. Winner of travel grants from Belgian Microscopy Society (BSM) and European Microscopy society (EMS), 2013 and 2014.
7. Key scientific article in “Advances in Engineering” edition 2015.

Chapter 1
Introduction context and objectives

The present era of *Nanotechnology*, has started engulfing and replacing the old machines and apparatus with novel miniaturized devices based on nano-facts and nano-objects. The objects of study under nanotechnology are of dimensions usually in the range from 1 to 100 nm (1 nm = 10^{-9}m). One of the young branches of this emerging technological tree is nanomagnetism. This branch has already started participating actively to make humanity flourish and prosper in domains such as information technology, medical diagnosis, industrial applications or even leisure. The 2007 Nobel Prize for Albert Fert recognized the extraordinary achievement and contribution of the research in nanomagnetism.

Materials that contain magnetic particles, films, and other structures in the nanometric scale are often described as nanostructured magnetic materials and are of great interest because they exhibit valuable and unique properties. New types of materials with different structures and improved physical properties are subject of constant interest. Scope of nanomagnetism wraps the scrutiny of properties and applications of the magnetism of isolated nanoparticles, nanodots, nanowires and nanotubes to name a few. For instance, advances in the magnetic materials and nanomagnetism has helped tremendously increasing the magnetic data storage capacity from 5 MB [1] in early 1960s to 4 TB [2] in 2014 [Aune 2006,

[1] Byte is the unit of data storage and is represented by B
[2] (1Terabyte-TB ~ 1000 Gigabytes-GB and 1GB ~ 1000 Megabytes-MB)

Blackblaze 2014]. In conventional recording media, each bit is stored in a collection of hundreds of particles. In recent years, as shown in Figure 1.1, the transition from longitudinal to perpendicular magnetic recording (easy axis of the individual recording elements (bits) must be aligned in the out-of-plane direction) is underway leading to storage densities of few TB per square inch.

So far the continuous increase in the areal density is the result of direct scaling down of magnetic entities which have encountered a physical limit called superparamagnetism. This situation is faced due to miniaturization of the magnetic grains to an extent that even the ambient temperature will flip the magnetization of the grains holding magnetic information (from "0" to "1" and vice versa). The energy barrier of a grain in the absence of external magnetic field in its simple form is, $E_B = K_u V$, where V is the volume and K_u the magnetic anisotropy constant. This barrier can be increased by increasing either V or K_u. The higher value of anisotropy (thus higher coercive field H_c of the medium) brings technical problems linked with the read/write capacity of hard disk drive (HDD) head.

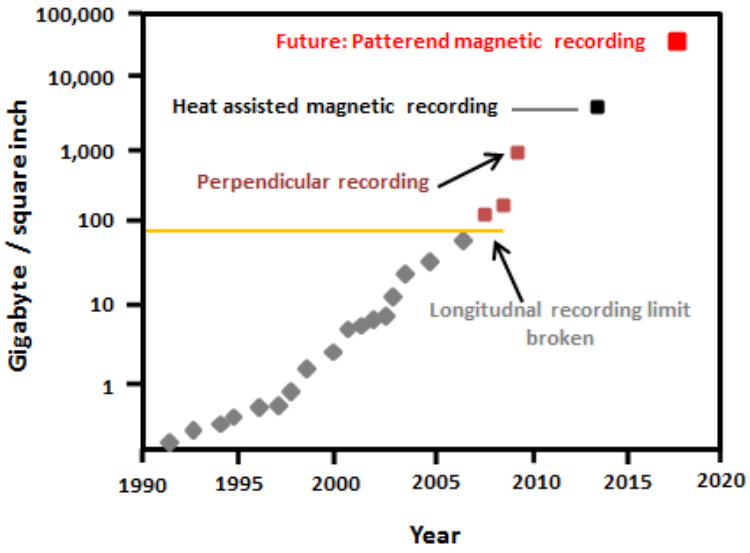

Figure 1.1: HDD recording-density trend, adapted from [Aune 2006]

Recently, researchers came up with an idea of using one single elongated particle of larger V to store one bit instead of using plenty of grains per bit-as depicted in

Figure 1.2. Due to the shape anisotropy effect linked with the increased volume, it is much easier to magnetize a 1D ferromagnet to its saturation using a longitudinal field. In this context, high aspect ratio[3], small diameter and single domain magnetic nanowires fabricated into the pores of porous anodic alumina has been suggested to be suitable as patterned magnetic recording media [Albrecht 2000, Nielsch 2001]. Their high aspect ratio (diameter in tens of nm and lengths in μm) helps suppressing the onset of the 'superparamagnetic limit' thus preventing the loss of magnetically recorded information among the nanowires.

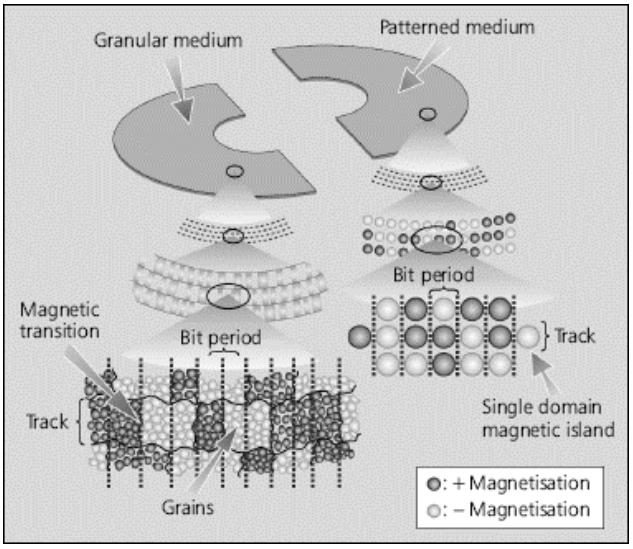

Figure 1.2: One single island stores one bit in patterned media compared with the many random grains of conventional granular media. Adapted from [Ryan 2010]

Furthermore, there has been an increasing demand for new types of nano materials with different structures and improved physical properties to be used in miniaturized devices. This development in nanomaterials domain became possible thanks to the invention of scanning tunnelling microscopy (STM) in 1980s. Although STM represents an excellent way to characterize the surface, it has certain limitations such as conducting samples and a strict operation requirement. This led to the invention of the atomic force microscopy (AFM) that enables the imaging of surfaces of various types of samples under ambient conditions and its capability to

[3] Aspect ratio = length /diameter

incorporate local electrical and magnetic measurements [Asenjo 2001]. Electron holography and nanoSQUIDs are employed to extract the properties of individual nano magnetic entities but they do have a limitation of tedious sample preparation and measurement methods [Thomas 2008, Hao 2010]. Therefore, to study the individual magnetic nanostructures magnetic force microscopy (MFM), an operational mode of AFM, is being used extensively nowadays [Asenjo 2006, Yuan 2008, Jaffar 2009, Tabasum 2013b, Rozmann 2014]. The special probe, magnetic probe, is brought close to a sample and interacts with the magnetic stray fields emanating from the surface.

Along with other conceivable candidates for novel devices, magnetic nanowires (NWs) and nanotubes (NTs) have been produced because of their unique magnetic properties and potential technological applications in, for instance, microwave devices [Encinas 2007, Darques 2009, Hamoir 2013], chemical sensors [Favier 2001, Murray 2004], high density data storage [Nielsch 2001, Wang 2008, Proenca 2013], and light emitters [Li 1999, Sun 2000, Martin 2005]. Magnetic NWs and NTs are attractive in physics but they also got an enormous attraction in biological and biomedical applications [Martin 2003, Lee 2002, Escrig 2007b, Lee 2007]. They have been proven to be promising tool for cell manipulation and positioning and have also been suggested for hyperthermia usage to treat cancer cells [Choi 2008].

However, as for any magnetic system, the overall peculiarity of NWs and hence their suitability for a particular application would be determined by magnetic anisotropy which is determined by many factors such as geometry, orientation and the interwire distances. There is a basic need of understanding the magnetization reversal process and of control of their magnetization behavior to use these magnetic nanostructures in magnetic data storage applications and in novel devices such as sensors, microwaves etc. Generally, very high density arrays of NWs are supposed to be used for the above mentioned applications. Efforts have been made to understand magnetization switching and to extract the intrinsic switching fields of individual entities by using certain corrective formulas [Sorop 2003, Yuan 2008, Wang 2008]. There were no studies done on non-interacting

arrays of NWs/NTs to have an insight into their intrinsic properties. Therefore, the objective of the present work was to understand the magnetic properties (reversal) of individual magnetic NW/NTs. To reach this objective, several sub-objectives were focused:

1. Developing an adapted characterization method based on MFM. Actually this is the first detailed experimental work on this topic at our lab so there was a need to modify the existing facility i.e. AFM to perform *in situ* and *in field* MFM measurements. Therefore to apply the magnetic field, electromagnets of proper dimensions, were fabricated and placed under the sample in AFM.
2. Study the magnetization reversal in dilute arrays as a function of material, NWs packing density, NWs diameter, geometry (NWs or NTs). Magnetic NWs arrays of various diameters were first characterized to comprehend the influence of changing diameter and then keeping the diameter same, effect packing density was observed. Further, comparison of modifying the geometry, filled nanocylinders (NWs) versus hollow (NTs) was made.
3. Determining the interaction field between an individual NW and its neighbors. NWs arrays of very dilute and medium packing density were used to explore the influence of changing the interwire distance of surrounding NWs.

The basics of magnetism are presented in the **chapter 2** to facilitate the understanding of the thesis contents. State of the art concerning magnetic NWs and NTs, arrays of these entities and the MFM characterisation of them are summarized in this chapter. It is shown that the MFM studies done on magnetic NWs were usually on high density arrays whereas NTs were not yet exploited using this technique. Out of various techniques, electrodeposition has been used to fabricate the magnetic nanostructures. To study the individual magnetic entities a home-made electromagnet was built to apply *in field* and in situ external magnetic fields during MFM measurements **(chapter 3).** In magnetism, magnetometry (alternating gradient force magnetometer-AGFM) instruments are generally used

to access the global properties but they are practically unable to extract the magnetic characteristics of single units. MFM, a special mode of operation of the AFM, employs a magnetic probe (incorporating the tip) to characterize the nano magnetic entities quite easily. MFM has the capacity to map the local stray fields emanating from the individual nanostructures of the sample, hence provides the insight into their magnetic behavior. The fabrications methods, materials, characterization techniques and experimental methodologies used during this work are regrouped in this chapter.

Chapter 4 is devoted to the determination of the magnetization reversal progress of dilute arrays of single domain ferromagnetic NWs to extract the intrinsic switching field distribution map and to evaluate the influence of geometrical parameters e.g. diameter. As expected, the attitude of arrays of isolated NWs is quite different when compared with the compact NWs arrays (of the same diameter). For smaller diameters, it seemed essential to have a strict control on their diameter size distribution if one wants to employ them into applications which require narrow switching fields. Interestingly, this fact is valid for all the materials under study i.e. Ni, NiFe and CoFe.

The curiosity to question the influence of morphology of magnetic entities, on the global properties of the arrays, motivated us to investigate magnetic NTs. To the best of our knowledge MFM characterization of magnetic NTs arrays have not been performed up to present study. The fundamental properties of magnetic nanotubes arrays have been well described theoretically but in reality they are subject to certain flaws and imperfections which along with their geometrical parameters strongly affect the mechanism and dynamics of the magnetization reversal. **Chapter 5** presents the results on effect of different morphologies i.e. solid cylinders (NWs) and hollow cylinders (NTs). Due to their specific geometry-hollow core, the way NTs react to the external applied field is different than NWs. Linking intrinsic and external effects on the behavior of magnetic NWs and NTs it is shown that, for the same packing density, NWs array demonstrated stronger

magnetic interactions than the NTs arrays. The influence of the packing density for the same diameters has been elaborated as well.

Finally, MFM analyses have been used to extract quantitatively and precisely the interaction field by observing the switching of single NWs. It will be shown that the methodology of employing MFM to assess the magnetic properties at nanoscale is a unique way to have information on interaction fields of single magnetic particles which is very useful for magnetic logic devices and patterned magnetic media **(Chapter 6)**. Furthermore, as it was essential at this step, a simple and straight forward approach has been used to evaluate the influence of the tip's stray field on the MFM measurements. Finally, the outcomes of this work are summarized in the last chapter "Conclusions and Perspectives".

Chapter 2
State of the art and theoretical background

This chapter, firs presents the basic and fundamental concepts of magnetism to understand the observations and discussions presented in this thesis. It starts with a brief history and an introduction to magnetism followed by detailed description of magnetic anisotropy. Later, the domain structure and single domain behavior of nanostructures are discussed. Then the fundamental concepts such as magnetic interaction and magnetization reversal mechanisms have been described. The fundamental properties of the magnetic NWs and NTs have been well described theoretically but the real systems are subject to certain flaws and imperfections which strongly affect the mechanism and dynamics of the magnetization reversal. The end of this chapter provides an insight into the magnetic force microscopy (MFM) characterization studies to understand the reversal behavior of densely packed arrays of magnetic NWs and NTs.

2.1 Introduction

The area of the materials science and physics which deals with the magnetic properties of the objects having at least one dimension in nanoscopic range, from 1 nm (10^{-9}m) to 100 nm, is the *nanomagnetism*. Its scope includes the study of properties and applications of the magnetism of isolated nanoparticles, nanodots, nanowires, thin films and multilayers, and also macroscopic samples that contain nanoscopic particles [Alberto 2009]. Nanomaterials are of great interest because

they exhibit valuable and unique physical and chemical properties. Furthermore, there is an increasing demand for new types of materials with different structures and improved physical properties to be used in miniaturized devices. This has led, along with other conceivable candidates to the production of magnetic NWs and NTs due to their magnetic properties and potential technological applications such as nanoelectronic devices, optical components, chemical sensors, high density data storage, and light emitters [Nicoleta 2010].

Magnetic NWs are attractive not only in physics but they got an enormous attraction in biological and biomedical applications. They have been proven to be compliant tool for cell manipulation, positioning and have also been suggested for hyperthermia usage in cells to treat the cancer cells [Choi 2008]. Heating in this application is caused from the magnetic hysteresis to destroy the harmful cells. There are numerous ways to grow the NWs and NTs of various kinds and materials but electrodeposition is considered the most versatile and low cost technique [Nicoleta 2010].

Magnetization hysteresis curve is used to characterize the behavior of nanostructured magnetic materials. The characteristics features of the this curve (detailed description follows later in this chapter) are linked to the type of material, size and shape of the entity, orientation of the sample with respect to the field and sample's magnetization history. Switching field distribution SFD, saturation magnetization (M_s), remanent magnetization (M_r), coercive field (H_c) and saturation field are key parameters to describe the magnetic behavior of magnetic entities. The huge progress in nanotechnology would have not been possible without the modern trend towards the miniaturization of devices and the development of specific instrumentation e.g atomic force microscope (AFM) that could visualize the nanomaterials [Eftekhari 2008].

Understanding the properties of the magnetic nanostructures is essential to employ them into modern advanced devices. Magnetic force microscopy (MFM), a special mode of operation of the AFM, employs a magnetic probe (incorporating

the tip) to characterize the magnetic entities. MFM has the capacity to map the local stray fields emanating from the individual nanostructures of the sample, hence provides the insight into their magnetic behavior. MFM presents excellent resolution for individual magnetic nano structures and provides simultaneous information about topography and the magnetization. The principle and the modes of operations of MFM are explained in chapter 3 (section characterization techniques).

2.2 Brief history and origin of magnetism

The history of magnetism evolves with the science's history. Although its earliest history is obscure, its power of attracting iron has captivated the countless curious spirits for millennia. The first magnetic materials known to man was the lodestone-magnetite (Fe_3O_4), found in a district of ancient times, Magnesia (modern Turkey), which was supposed to be magnetized with a huge flux of lightening currents. The earliest magnetic device was the lodestone carved in the shape of a Chinese spoon that turned on the base to align its handle with the Earth's magnetic field shown in Figure 2.1.

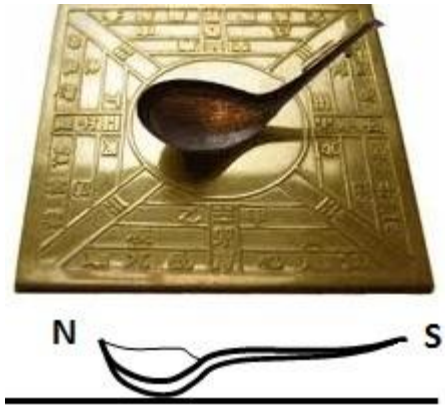

Figure 2.1: The earliest magnetic device from China "South pointer"

In 1064, steel needles from red hot quenched iron were made that, aligned themselves with the Earth's field when floated or suitably suspended, led to the invention of the navigational compass. The discovery of America by Christopher Columbus in 1492 and the earlier Chinese discovery of Africa by the admiral Cheng Ho in 1433 would have not been possible without the use of compasses. The first

scientific text “On the Magnet”, arguably, was from William Gilbert in 1600 that overthrew many superstitions about the origin of magnetism. Until beginning of nineteenth century, before Hans Christian Oersted discovered in 1820 that an electric current produces a magnetic field, the only way of making magnet was rubbing the iron and steel with a lodestone. This invention was the breakthrough for the research on magnetic materials. Later Michael Faraday discovered electromagnetic induction in 1821 and magneto-optic effect in 1845. All this experimental work inspired James Clerk Maxwell’s formulation of a unified theory of electricity, magnetism and light in 1864. Altogether that brought the industrial developments such as electric motors, street lights and telegrams which improved the public life [Kethly 1999, Coey 2010, Cullity 2009].

Recent decades have witnessed an immense expansion in magnetic applications. There have been advances in earth science, medical imaging and the theory of phase transitions that can be laid at the door of magnetism. More recently efforts to understand on small length scales are being made, which has large implications on the developments in nanotechnology. As a consequence, magnetism is currently present in everyday life, not only on large scales, like in the electric motor of a washing machine and fan of an air conditioner, but also on very small scales, like in the hard disk of a computer where this chapter is being stored. Despite the widespread applications of magnetism, a lot of fundamental questions persist and magnetism remains an extremely rich scientific research domain.

2.3 Types of magnetic materials

Electric charges can be isolated in the form of positive or negative charges, whereas the same cannot be done with magnetic poles. In any single magnet, if one end is its north pole, the other end is its south pole. By breaking a magnet, there are two smaller magnets generated, each with both a north pole and a south pole. Hence, we often use the term “dipole” for a magnet. At atomic level these dipoles can be created by the electron. Electrons have orbital and spin angular momenta and their net would be responsible for making an atom, containing many electrons, magnetic or non-magnetic. If the net angular momentum is nonzero

then the atom would behave as a tiny magnet and the quantity to measure its strength is the magnetic moment expressed in emu (electromagnetic unit). The Bohr magnetron, μ_B, is the *magnetic moment m* associated with the orbital angular momentum of an electron around the nucleus of a hydrogen atom and is used as a unit for magnetic moments. When talking at macroscopic level, for condensed matter, the magnetic moments from the constituting atoms sum up and represented by *magnetization M*, which describes the degree to which magnets are magnetized and is written as magnetic moment/volume and its units are *emu/cm*^{3}.

M varies when an external *magnetic field H,* also called magnetizing force, is applied to the materials and its units are *Oersted* (Oe). So *H* is the "fundamental" magnetic field, which produces magnetization *M* in magnetic materials. The magnetic properties of a material are characterized by the way *M* varies with *H*. The ratio of these two is susceptibility $x = \frac{M}{H}$ and defines the types of materials as diamagnetic, paramagnetic, antiferromagnetic and ferromagnetic mainly. Out of these, paramagnetic and in particular ferromagnetic (Figure 2.2) are of interest in the present work.

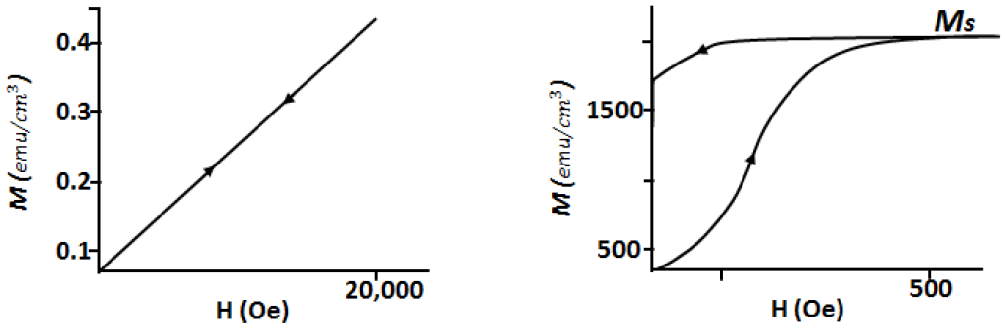

Figure 2.2: Typical magnetization curves of a paramagnetic material (left) and a ferromagnetic material (right). Adapted from [Cullity 2009]

Paramagnetic materials have net magnetic moment when under applied field, however the sample remains magnetic until the field is present. Once the field is removed the thermal effects brings the material back to zero net magnetization state. Al, Mg and Ru behave as paramagnetic. The subsequent sections of this chapter are devoted to **ferromagnetic (FM)** material, in which the permanent

magnetic moments interact strongly with each other to align even in the absence of an external magnetic field. The behavior of a FM simply can be revealed by its M-H curve also called hysteresis curve explained below.

2.3.1 Magnetization processes and hysteresis

The spontaneous magnetization of FM materials such as Ni, Co, Fe and their alloys is a remarkable manifestation of magnetism. The essential characteristic of a FM material is the irreversible nonlinear response of magnetization *M* to an applied field *H*. This response is symbolized by the hysteresis curve (Figure 2.3) which shows the history dependent nature of the magnetization of the magnetic material. This curve is magnetization hysteresis curve. To get this curve, the sample is saturated in one direction, a reverse field, *H*, is applied, and the value of *M* is noted. The dotted line, inside the curve, in the Figure 2.3 shows the initial saturation process of the multi domain magnetic material. The external magnetic field forces the orientation of various randomly oriented domains in the field direction.

When an external field is applied on the multi domain structure the magnetic domain walls align themselves and further applications of the field will bring no change in the *M* of the sample, this is the saturation magnetization M_s. M_s value for various materials used in this study are shown in the table 2-1 [Sun 2005]. Now, if the field is removed some of the magnetic domains will switch opposite to the saturation magnetization bringing the sample back to a state called remanent magnetization M_r and if a negative field is applied on the sample a state named as coercive field H_c is reached where there are half the moments up and half down. Further application of the field will saturate the sample where all the moments will be aligned opposite to the initial state i.e. saturation has again reached. A FM can also be completely demagnetized by applying cyclic magnetic field of lower amplitude or by thermal demagnetization process.

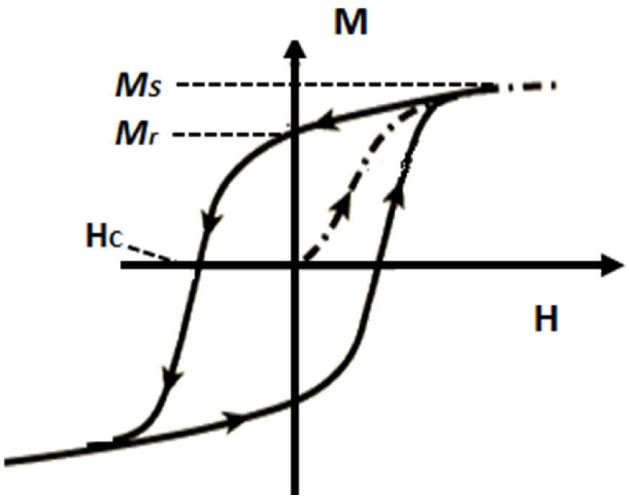

Figure 2.3: Hysteresis curve of a ferromagnetic material

Table 2-1: Values of saturation magnetization for various magnetic materials

Material	M_s (emu/cm^3)
Ni	485
$Co_{55}Fe_{45}$	1950
$Ni_{80}Fe_{20}$	800

2.4 Magnetization energy of a ferromagnetic material

The magnetostatic and the domain wall energies are critical in determining whether a particle is single or multidomain as well as for calculating the characteristics parameters of their hysteresis curve. The total energy of magnetization in a magnetic entity is

$$E = E_{ex} + E_H + E_{ME} + E_{MC} + E_{MS} \quad (2.1)$$

Where E_{ex} is the exchange energy, E_H is the Zeeman energy, E_{ME} is the magnetoelastic energy E_{MC} the magnetocrystalline energy and E_{MS} is the magnetostatic energy.

E_{ex} in a FM material is related to the interaction between the spins and tries to keep the directions of the atomic moments parallel to each other. E_{ex} between two

adjacent atoms *i* and *j* can be written as $E_{ex} = -2 \sum_{ij} J_{ij} S^2 \cos\theta_{ij}$, where J_{ij} is the exchange integral, S is the spin associated with each atom, and θ_{ij} is the angle between adjacent spin orientation. For FM materials J is positive and minimum energy state occurs when the spins are parallel to each other. Exchange interactions are short range and are depicted by exchange stiffness constant *A* whose value for most FM materials is typically between $1x10^{-6}$ to $2x10^{-6}$(erg/cm). If the magnetic moments of neighboring atoms are made to change their directions with respect to each other, it has to be at the cost of the exchange energy.

Zeeman energy is the magnetic potential energy which is simply the energy of the magnetization in an external applied field, expressed as $E_H = -M.H$. Here, $M \text{ and } H$ are external field vector and magnetization vector respectively. This energy is always minimized when the magnetization is aligned with the applied field. The magnetoelastic energy originates from the influence of stress/strain on the materials. If the crystal anisotropy is weak the direction of the *Ms* in the absence of the field will be largely governed by externally applied stress. The application of a small tensile stress to the demagnetized specimen may cause domain walls to move in such a way as to decrease the volume of domains magnetized at right angles to the stress axis, because such domains have high magnetoelastic energy. These domains can be completely eliminated by some higher value of the stress to minimize E_{ME} . The last two terms of equation (2.1) are collectively named as magnetic anisotropy. It is worth mentioning that ability of a material to magnetize more easily in one direction than another is called magnetic anisotropy. Along the easy axis the magnetic saturation can be achieved with the smallest applied magnetic field in comparison to any other axis or direction. The magnetic anisotropy can be modified by adopting proper materials and geometries. As during this thesis we have changed the material parameters like type of the material and their geometries so these energy contributions, for magnetic anisotropy, were crucial to understand and are presented in more details.

2.4.1 Magnetocrystalline anisotropy

In anisotropic crystals the distance between atoms in different directions varies. Therefore the magnetocrystalline anisotropy is an intrinsic characteristic of the materials and its origin lies in spinorbit coupling i.e. interactions of spin and orbital motion of each electron. As a result of this coupling, when an attempt to reorient the spins of an electron by applying an external field is made its orbital motion, which is linked with the crystal lattice, tends to reorient as well, counteracts this attempt to rotate the spins. The energy required to overcome the spin-orbit interactions and to rotate the spins of a domain away from the easy axis is E_{MC}. For example in hexagonal lattice, the E_{MC} is expressed as [Piramanayagam 2012]

$$E_{MC} = K_1 \sin^2 \theta + K_2 \sin^4 \theta + \cdots \qquad (2.2)$$

where K_1 and K_2 represent the magnetocrystalline anisotropy constant. As there is only one easy axis of magnetization, terms involving K_2 are very small, hence negligible [Sun 2005, Cullity 2009].

Depending upon the values of K_1 in certain directions anisotropy results in a so-called hard and easy axis. This means that, along an easy axis, the magnetization is easily saturated (Figure 2.4).

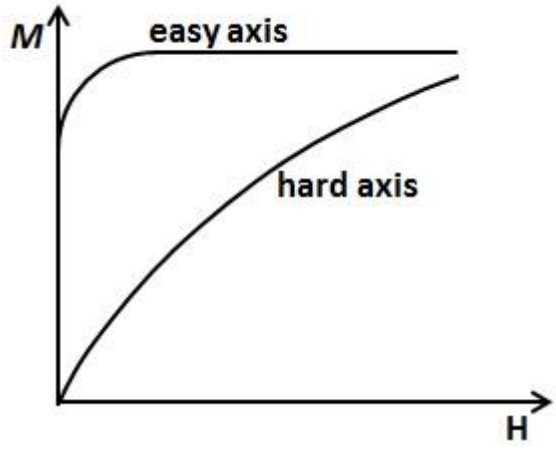

Figure 2.4: The response of the magnetization *M*, to an external magnetic field *H* applied along easy and hard axis. These curves are arbitrary and don't present the crystalline directions.

The strength of the anisotropy in any particular crystal is measured by the magnitude of the anisotropy constants K_1, K_2, etc. Although there seems to no

doubt that crystal anisotropy is due primarily to spin-orbit coupling, the details are not clear, and it is generally not easy to calculate the values of the anisotropy constants in a particular material from first principles. Further, there isn't any simple relationship between the easy, or hard, direction of magnetization and the way atoms are arranged in the crystal structure. Thus in iron, which is body-centered cubic, the direction of greatest atomic density, i.e., the direction in which the atoms are most closely packed, is <111>, and this is the hard axis. But in nickel (face-centered cubic) the direction of greatest atomic density is <110>, which is an axis of medium hard magnetization. Non textured polycrystalline materials are a collection of randomly oriented crystals and no overall crystalline directions are present in the material hence they demonstrate negligible magnetocrystalline anisotropy. In hexagonal Co lattice which represents the strong magnetocrystalline anisotropy, the hexagonal axis [001] is the unique easy direction of magnetization [Coey 2010].

2.4.2 Shape anisotropy (Magnetostatic energy)

As the name indicates the magnetostatic energy or demagnetization energy is related to the shape of the sample and effect of nearest magnetic neighbors. It is solely an extrinsic characteristic of the material. The sphere will be magnetized equally in all directions on the application of the field which is not the case for ellipsoid or prolate spheroid. They can be easily magnetized in their long axis than the short ones. Shape anisotropy is an important effect at nanoscale especially when anisotropic samples such as NWs and NTs are under considerations. When a rod shaped material is magnetized it has poles at the two ends. The magnetization emanates from north pole towards its south pole both inside and outside the rod. This means that field lines entering the south pole got opposite field lines from inside the rod and try to demagnetize the rod with a field called demagnetizing field H_d. The demagnetizing field for an arbitrarily shaped sample can be quite complex and most of the time is non-uniform. It is only for ellipsoidal-shaped samples that the demagnetizing field turns out to be uniform. Let's consider a prolate spheroid, the nearest approximation for a NW, as shown in the Figure 2.5.

When it is magnetized to a magnitude *M*, at an angle θ, the magnetostatic energy E_{MS} can be expressed as [Cullity 2009]

$$E_{MS} = \frac{1}{2} M^2 \sin^2 \theta \, (N_a - N_C) \tag{2.3}$$

where N_c and N_a are the demagnetizing factors along *c* and *a-axis* respectively. Here the shape anisotropy constant is $K_s = \frac{1}{2} M^2 \, (N_a - N_C)$ which indicates that the aspect ratio *c/a* of the sample is very crucial to determine the shape anisotropy. For high aspect ratio NW and NT, in our case the aspect ratio is always more than 100, $N_a = 2\pi$ and $N_c = 0$. Thus the shape anisotropy energy $E_{MS} = \pi M^2$ [Cullity 2009, Sun 2005]. In our studied systems the shape anisotropy is always dominant over crystalline anisotropy, as materials with significant magnetocrytalline anisotropy such as Co will not be considered, so the easy axis of magnetization is along the wire length [Fert 1999].

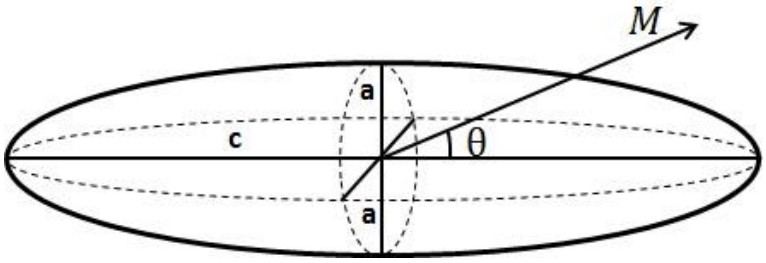

Figure 2.5: Schematic of a prolate spheroid

2.5 Single domain formation

Despite the strong interaction between spins in a FM, a complete alignment of all the spins does not always occur. The magnetic moments of neighboring atoms would normally be aligned parallel to each other if exchange energy were the only energy playing a role. However, if this happens for the entire sample, free poles will be formed at the surface, which would mean larger magnetostatic energy. As the system tends to be at lowest energy the FM can break up into magnetic domains, regions in which the spins are mutually aligned, but with a different orientation from adjacent domains as shown in Figure 2.6.

Although the formation of domains in a system reduces the magnetostatic energy, domain formation also results in the creation of an angle between the magnetic moments of the neighboring atoms as we move from one domain to another. This will cause an increase in energy as this change of magnetization works against the exchange forces. In order to spend the least energy for the transition, the magnetic moments would change their directions only gradually from one domain to another by a domain wall.

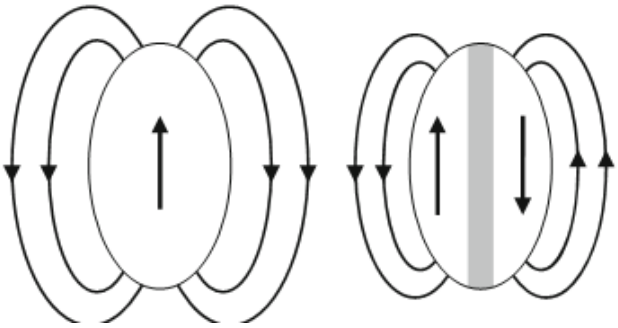

Figure 2.6: Single-domain and two-domain configurations of a magnetically ordered ellipsoid, showing the magnetic moments of the domains, the lines of field, and in the second case, the domain wall.

The particle will be completely magnetized in one direction i.e. single-domain particle when the cost of stray field (magnetostatic energy) is below than maintaining a domain wall, at a certain diameter [Frei 1957]. Brown has claimed and proved this theoretically by using the thermodynamic principle [Brown 1968]. So there are good reasons to believe that a sufficiently small magnetic particle will not contain domain walls and so will consist of a single domain. One simple argument is that, if the particle is smaller than the thickness of a domain wall, it cannot consist of two domains separated by a domain wall. The critical radius for a magnetic particle below which it stays single domain is r_{sd} and is given by the following expression [Sun 2005]

$$r_{sd} = \sqrt{\frac{6A\left[l_n\left(\frac{2r_{sd}}{a_1} - 1\right)\right]}{{M_s}^2 N_C}} \qquad (2.4)$$

where A is the stiffness constant , M_s is the saturation magnetization, a_1 the near neighbor spacing and N_c the demagnetizing factor. The stiffness constant of FM is a

force acting to keep the magnetic moments aligned. For the NWs and NTs of this work its value is ~1 x 10^{-6} erg/cm. The demagnetizing factor N_c is strongly dependent upon the aspect ratio $m = c/a$. It decreases with increasing aspect ratio.

The critical radius is dependent upon the geometry and the type of FM and increases with increase in aspect ratio ($m=c/a$) because of the decrease in demagnetizing factor N_c. By using the equation 2.4, the values of the r_{sd} for various materials of interest of this work has been calculated[4]. For instance, for aspect ratio m=10, Ni, NiFe and CoFe are expected to have the single domain below the r_{sd} ~ 450 nm, ~370 nm and ~220 nm respectively. This can be seen in Figure 2.7.

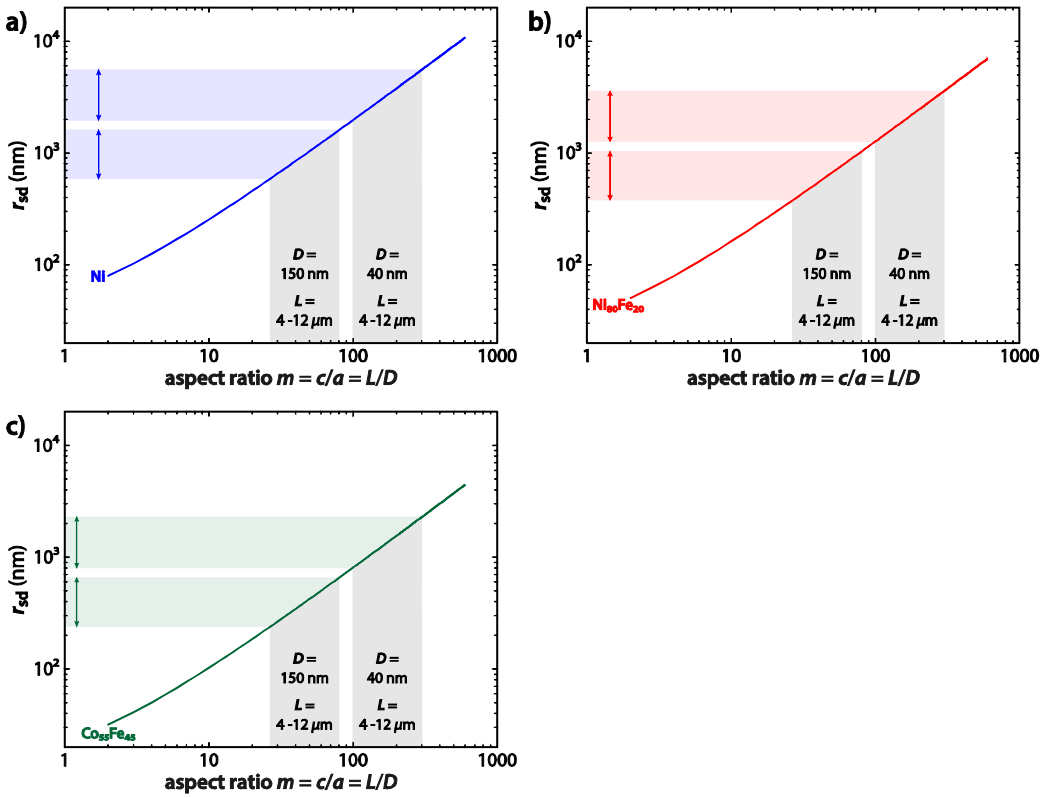

Figure 2.7: Calculated critical radius for a single domain prolate spheroid of, a) Ni, b) NiFe and c) CoFe as a function of aspect ratio.

2.6 Super paramagnetism

The magnetic behavior of nanoparticles is strongly dependent on their dimensions. The smaller magnetically ordered particles will tend to be single-domain, and the

[4] Matlab calculations are done by Dr. Flavio. Please see annex for details.

larger ones, above a certain critical diameter as multidomain or exhibit a vortex configuration. At a certain size and in the absence of the external applied field the thermal energy overcomes the exchange energy of the magnetic moments and a ferromagnetic material behaves like a paramagnetic one, this is called *super-paramagnetism* [Neel 1949]. The energy barrier ΔE for the magnetization reversal is expressed as [Yin 2002, Sun 2005]

$$\Delta E = \mathrm{U}\left(1-\frac{H}{H_0}\right)^{1/n} \tag{2.5}$$

Where *U* is the energy barrier at zero applied field, *H* is the applied field, H_0 is the field needed to overcome the barrier at zero temperature and parameter *n* indicates the switching mechanisms.

For single domain particles having uniaxial shape anisotropy (NWs and NTs) and where curling is the dominant switching mechanism, the following equation have been adopted [Sun 2005]

$$\Delta E = K_u \mathrm{V}\left(1-\frac{H}{H_0}\right)^{3/2} \tag{2.6}$$

where *V* and K_u represent volume and uniaxial magnetic anisotropy constant of the ferromagnetic material respectively.

Since energy barrier for the reversal according to equation (2.6) is proportional to volume, a particle below a critical value would not have energy barrier high enough to prevent switching at ambient temperature. For magnetic NWs and NTs, prolate spheroids is a close approximation (Figure 2.5), the energy barrier in remanent state (*H*=0) can be calculated. For a prolate spheroid, $K_u = \frac{1}{2} M_s^2(N_a - N_C)$, provided the aspect ratio *m* >10 it turns out that $\mathrm{K}_u = \pi \mathrm{M}_\mathrm{S}^2$. On the basis of this assumption, the energy barriers have been calculated [Sun 2005]. The probability, *P*, for not reversing the magnetization, against the thermally induced reversals at temperature, T, is given by Néel–Arrhenius formulation as

$$P = f\ exp\left(-\frac{\Delta E}{Tk_B}\right) \quad (2.7)$$

where f is the thermal attempt frequency and the k_B the Boltzman constant. This indicates that for single domain structures with uniaxial shape anisotropy the thermal energy, Tk_B, when of the order of shape anisotropy energy KV may switch their magnetization in the absence of the external field (means at very small diameters or at elevated temperatures). So, for the magnetic wires to have stable magnetization over a long period of time, years, the requirement is $\frac{\Delta E}{Tk_B} > 50$ which can be achieved at aspect ratio more than 10. Time dependent magnetization reversal phenomena are very crucial in data storage but are not in the scope of this thesis.

2.7 Fabrication of ferromagnetic NWs and NTs

2.7.1 Different fabrication routes of magnetic NWs

Many techniques have been developed for the synthesis and formation of *1D* nanostructured materials (NWs and nanorods), though some techniques have been explored extensively, while others have attracted far less attention.

These techniques can be generally grouped into following categories:

1) Spontaneous growth: evaporation (or dissolution)-condensation
2) Template-based synthesis: Electroplating and electroless deposition
3) Lithography

Spontaneous growth and template-based synthesis are considered as a bottom-up approach, whereas lithography is a top-down technique. Spontaneous growth is a process driven by the reduction of Gibbs free energy or chemical potential. The reduction of Gibbs free energy is commonly realized by phase transformation or chemical reaction or the release of stress. For the formation of nanowires or nanorods, anisotropic growth is required, i.e. the crystal grows along a certain orientation faster than other directions. Uniformly sized nanowires, i.e. the same diameter along the longitudinal direction of a given nanowire, can be obtained

when crystal growth proceeds along one direction, whereas there is no growth along other directions. In spontaneous growth, for given material and growth conditions, defects and impurities on the growth surfaces can play a significant role in determining the morphology of the final products.

Generally used to fabricate magnetic nanodots, lithography represents another route to the synthesis of NWs. Various lithographic techniques have been explored in the fabrication of nanodots and NWs, such as electron beam lithography, ion beam lithography, X-ray lithography and near-field photolithography. NWs with diameters less than 10 nm and an aspect ratio of 100 can be readily prepared [Cao 2004]. This technique has been used to produce not only NWs but also nanomagnetic strips [Adeyeye 2008, Endo 2008, Iglesias 2014].

Template-based synthesis of nanostructured materials is a very general method and can be used in fabrication of nanorods, nanowires and nano-tubules of polymers, metals, semiconductors and oxides. Various templates with nanosized channels have been explored for the template growth of NWs. For instanceself-assembled diblock copolymers have been used to fabricate ferromagnetic NW arrays of high density [Albrecht 2000, Rosa 2009]. This approach has not been used extensively due to strict preparation conditions to create nano pores in templates. Therefore, the most commonly used and commercially available templates are anodized alumina membrane and track-etched polycarbonate (PC) membranes.

The templates can be filled using soft chemistry techniques where the wires are grown by using the appropriate chemical solutions. Magnetic NWs have been successfully prepared by controlling the reduction rate by varying a concentration of deposition solution and nucleating agents [Kawamori 2011].However, from the various strategies for embedding the matter of interest within the pores of templates, electrodeposition is the prevalent technique for the deposition of the magnetic NWs. The proof of the fact is that none of the cited work in magnetic force microscopy (MFM) characterization of magnetic NWs in this thesis (section 2.9) used another technique than electrodeposition. Electrodeposition can be

understood as a special electrolysis resulting in the deposition of solid material on an electrode. The electrodeposition is initiated by the application of a potential difference between the cathode and the anode. When an electric field is applied, cations diffuse toward and reduce at the cathode, resulting in the growth of nanowires inside the pores of template (see section 3.1.1 for details). This technique has been widely employed to fabricate not only the magnetic NWs of pure metals such as Ni, Co and Fe, but also to fabricate the alloys of magnetic materials such as NiFe, CoFe and CoPt etc.

Electrodeposition of metals into the pores of nanoscale templates has been particularly attractive because: (a) it is a simple, low-cost, high-throughput technique for fabricating large arrays of nanowires with monodispersive diameter and length; (b) it provides the ability to tailor size, length, shape and morphology of the material deposited by controlling the template morphology and the synthesis parameters; and (c) it provides the ability to introduce composition modulation along the wire length, which in turn enables precise control on architecture and magnetic properties [Nicoleta 2010, Aravamudhan 2009].

2.7.2 Different fabrication routes of magnetic NTs

In magnetic NTs not only the diameter and length but also the wall thickness can be tuned during synthesis steps, which may result in more control of magnetization reversal. The hollow core in NTs brings not only advantages but also some drawbacks i.e. their fabrication is not as straight forward as simple electrodeposition used for NWs. However, they have been produced by applying some modifications to the basic electrodeposition technique. The prominent NTs fabrication procedures have been briefly described in the succeeding paragraphs.

Bao et al. [Bao 2001] were the first to illustrate the electrodeposition of a perfect ordered array of Ni NTs in alumina membranes of tens of µm long and of 160 nm in diameter.

Sui et al. used an approach of chemical deposition and hydrogen reduction in porous alumina templates to produce FePt and Fe_3O_4 NTs of length 50 µm and of

diameters 150 to 220 nm [Sui 2004]. The templates were loaded with the proper chemical solutions which were decomposed thermally followed by hydrogen reduction to yield the desired composition.

A synthetic approach, to fabricate Ni/Cu core-shell NWs by co-electrodeposition of Ni and Cu in anodic alumina pores and selectively etching the Cu core, was opted by Q. Wang et al. [Wang 2005]. The formation of the Ni ions adsorbed on the pore walls was achieved by their chemical attachment. Various parameters can be changed to get the required lengths, surface morphology and wall thickness. Being simple and robust technique, this technique has been used in our group for the last couple of years and is shown in Figure 2.8.

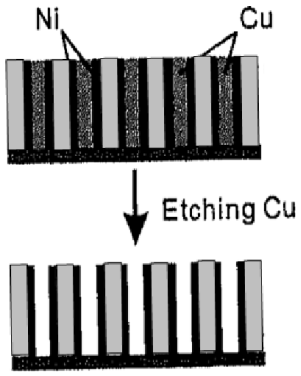

Figure 2.8: A schematic showing electrodeposited Ni-Cu nanocables which after etching Cu leaves only Ni nanotubes. Adapted from [Wang 2005]

Fabricating metal NTs without using surface modifiers for the template was done using a tri-block copolymer (commercial name P123) by Tao et al. [Tao 2006]. This distinctive approach used polymer surfactant which formed the micelles, on which Ni^{2+} gathered driven by the affinity between the oxygen of P123 and Ni^{2+}, in the electrodeposition solution. The excellent adsorption ability of alumina made the micelles concentrated on its walls and hence the deposition at the pore walls. Tube formation steps are shown in Figure 2.9. Daub et al. used atomic layer deposition (ALD) technique to synthesize magnetic NTs of Ni and Co of length 35 µm and external tube diameters ranging from 35-160 nm in alumina membranes [Daub 2007]. ALD is generally employed to coat three dimensional structures precisely

from two different vapour phase reactants. It was mentioned that this method has an excellent control to get the desired layer thickness.

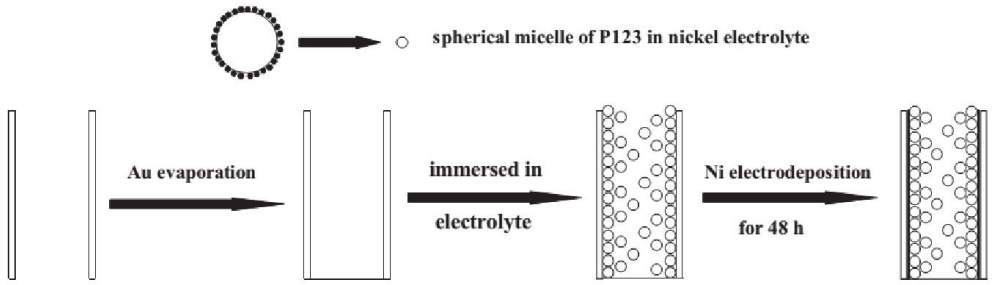

Figure 2.9: Schematic representation of Ni NTs fabrication and the proposed mechanism of the tubes growth. [Tao 2006]

X.F Han et al. suggested the low cost electrodeposition method to fabricate elemental, such as Fe, Ni, Co as well as alloy, such as NiFe, CoFeB, CoCrPt tubes in which use of the surface modifiers or of the polymer surfactants was not needed [Han 2009]. The use of sputtered conducting layer (Figure 2.10b) leaving the open holes resulted in NTs growth during electrodeposition (Figure 2.10). They indicated that the method was suitable to vary and tune the length, thickness and diameter of the studied tubes.

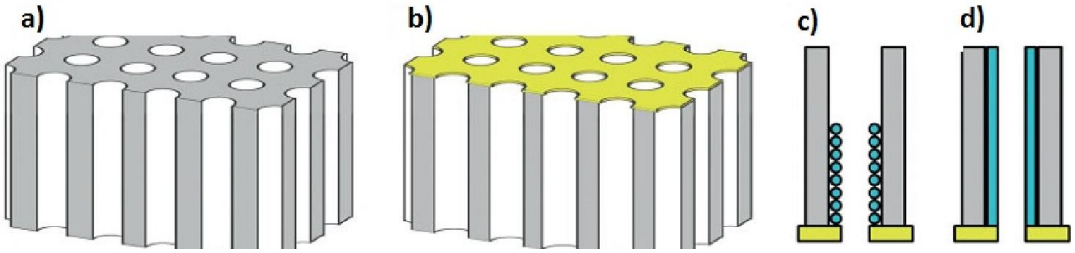

Figure 2.10: Schematic representation of NTs electrodeposition representing the bottom side of the template (a), thin Au layer sputtered on the bottom side (b), accumulation of positive charges along the pore wall (e) and growth of NTs (d).[Han 2009]

In electrodeposition of NTs, various parameters can be changed to get the required composition, lengths, surface morphology and wall thickness. For instance in Ni-P binary alloy NTs the amount of P was adjusted by controlling the cathode current densities [Liu 2010] whereas electrodeposition potential influenced the morphology of FeNi by fabricating NWs around -1 V to -1.2 V while NTs for voltages from -1.5 V to -2.5V [Zhang 2013a].

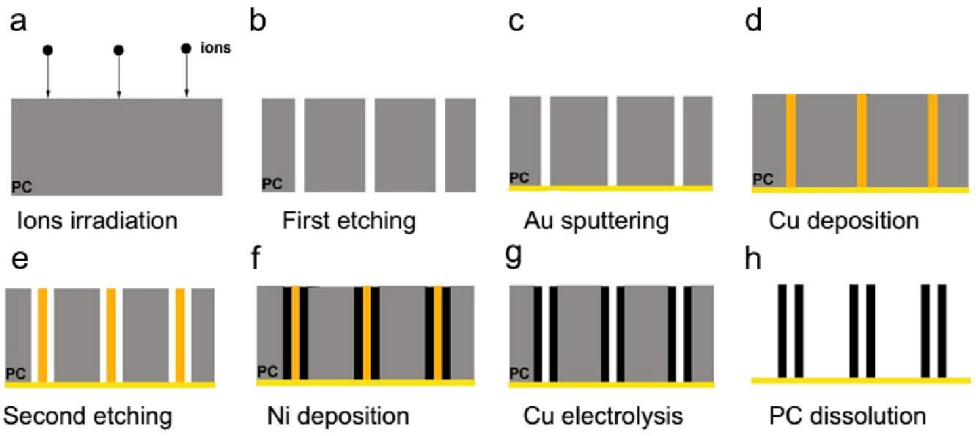

Figure 2.11: Schematic representation of proposed mechanism of the Ni NTs growth. [Chen 2014]

Recently a novel approach to deposit magnetic NTs of same inner diameter (100 nm) and different thicknesses (20 nm to 110 nm) in PC templates has been introduced [Chen 2014]. This consists of two-step track etching, two-step electrodeposition (Cu and Ni) and one-step electrolysis of Cu as illustrated in Figure 2.11.

2.8 Magnetization interaction and reversal in NWs and NTs

A thorough knowledge of the magnetic response of a material with externally applied field or without applied field is indispensable for the development of magnetic devices, where a good control over the magnetic switching is needed. Therefore understanding magnetization switching/reversal is vital and is the core of this work. Let's consider a single domain prolate spheroid (symmetry similar to NWs and NTs) under an applied field *H* at an angle θ with respect to its easy axis, the magnetization of the particle rotates along *H* and its energy density is given by [Wang 1999]

$$\frac{E}{V} = Ksin\,\varphi^2 - HM_S\,\cos(\theta - \varphi) \qquad (2.8)$$

The parameters *K*, *V* and M_s have been defined in the beginning of this section in equation (2.4 and 2.6). If we assume that the applied field is in the easy axis but $\theta = \pi$, then the above equation will become

$$\frac{E}{V} = Ksin\,\varphi^2 + HM_S\,\cos(\varphi) \qquad (2.9)$$

The two local minima of energy appear for ϕ=0 and ϕ=π. To make the magnetic particle switch we have to apply an external field of sufficient strength to overcome the energy barrier represented in Figure 2.12. The situation depicted explains the switching of the isolated magnetic single domain structure under the influence of the applied field.

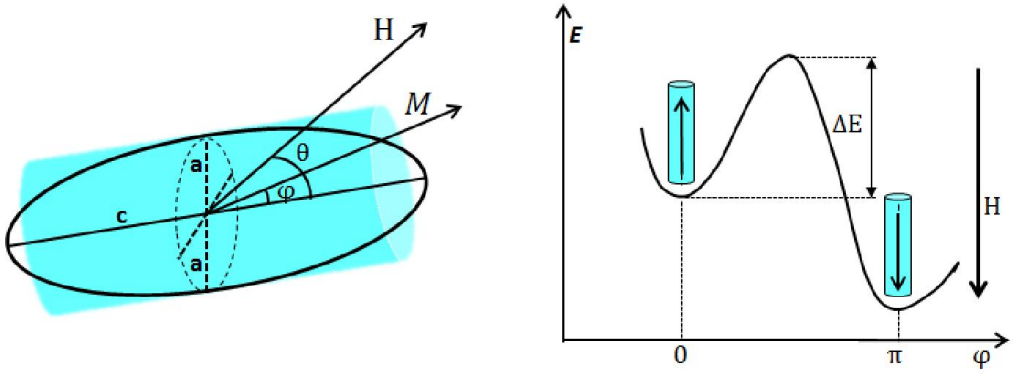

Figure 2.12: Prolate spheroid (left), an illustration showing the difference in the energy barrier between the two possible magnetization states of a magnetic wire (right).

In case there is an array of magnetic NWs and NTs (Figure 2.13), there will be a field exerted by the neighbors up to a certain distance even in the absence of the external field. This is due to stray field of the neighbors and as we consider all the neighbors as nano-magnets with theirs dipoles, this internal field is called dipolar field or this interaction is known as dipolar interaction. As a result of this interaction the energy barrier for various wires will be either enhanced or reduced resulting in non-uniform switching field for different elements of the array, hence the shearing of the hysteresis curve is enhanced [Ghadar 2011]. The range of magnetic field required to switch the first wire till the last wire in an array of magnetic objects is the switching field distribution (SFD). As it can be seen from the

Figure 2.13 the interacting array of NWs exhibit broader SFD compared with the non-interacting array which is considered as intrinsic SFD.

.

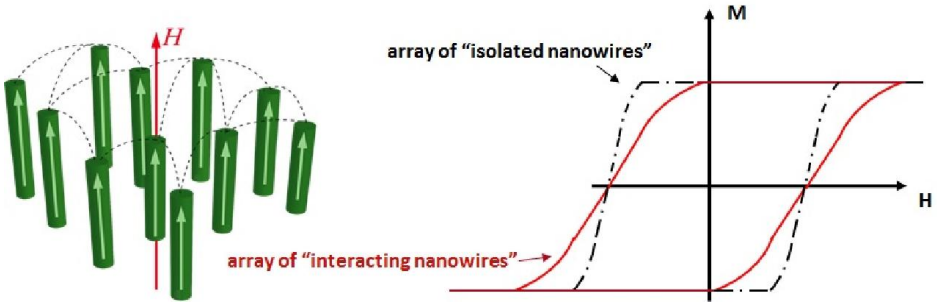

Figure 2.13: Array of interacting magnetic NWs (left) and the influence of interaction on the magnetization hysteresis curve.

When the shape anisotropy is dominant, as in elongated magnetic wires, the dipolar interactions depend upon their geometry, orientation in the template and the average inter-wire distance [Vazquez 2004]. In our experiments we will be using both systems, interacting and isolated wires, to study their magnetic reversal behavior.

The mehanisms of reversal are strictly size dependent as well. The multidomain structures change their magnetization by re-arranging the magnetic domain structure, n other words, the magnetization varies through the motion of magnetic domain walls, or changes in the shape of the domains. But there is a transition size between single domain and multidomain. Depending on the balance of magnetic anisotropy and exchange energy, the configuration of lowest energy for a nanoparticle of diameter just above the critical single-domain diameter is not a multidomain, but a swirl, or vortex, a circular arrangement of magnetic moments. But the studied systems of this work had a diameter which was always below single domain limit so the below sub-sections will elaborate the two categories of reversal which are dominant in single domain NWs and NTs.

2.8.1 Coherent reversal

During this reversal mode of the single domain particles, all magnetic moments remain parallel to one another to minimize the exchange energy and rotate around the easy axis (Figure 2.14). But when the magnetization component is along the hard axis the demagnetization energy increases. The switching field can be calculated using the Stoner-Wohlfarth model using the following formula for an infinite long wire [Stoner 1948]

$$H_{coh} = \frac{2K_u}{\mu_0 M_S} + \frac{M_S}{2} \tag{2.10}$$

where K_u is the uniaxial anisotropy constant and the *Ms* is saturation magnetization. The key feature of this model is that the switching field is independent of the size. The values measured experimentally rarely approach this theoretical value explaining the fact that reversal is nucleated at structural imperfections and flaws.

2.8.2 Curling

This represents the inhomogeneous nucleation and the dominant mechanism of reversal for the structures above a certain critical size but still in the single domain regime [Aharoni 1958]. It becomes then energetically favorable to break the exchange coupling and the moments rotate in a chiral fashion around the easy axis instead of all being parallel (Figure 2.14) , to save the stray field energy i.e. demagnetization energy. The reversal in this case is an abrupt process in which switching field and nucleation field are dependent on the size and aspect ratio of the particle. The switching field for a wire with uniaxial anisotropy when field is applied along its easy axis is given by [Zhu 2008]

$$H_{cur} = \frac{2K_u}{\mu_0 M_S} + \frac{6.78\ A}{\mu_0 M_S R^2} \tag{2.11}$$

The exchange energy and the demagnetization energy compete to decide the reversal mode.

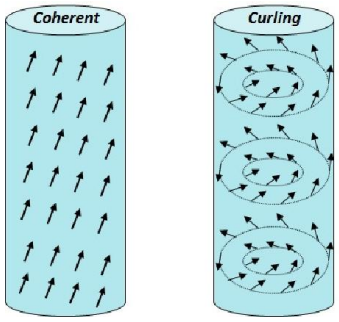

Figure 2.14: Magnetization reversal modes for rod like shapes.

During the curling, the exchange energy density increases with decreasing size as the relative angle between neighboring moments increases hence coherent rotation is favored. On the other hand, increase in the demagnetization energy for smaller sizes favors curling. Further in the curling regime, the switching or the coercive field increase significantly with decrease in diameter. Curling mode requires a minimum diameter to work which is D_{cur} = 13.208 l_{ex} (nm) where the exchange length is, l_{ex}=$\sqrt{\frac{2A}{\mu_0 {M_S}^2}}$. So, critical diameter for inhomogeneous reversal depends only on the exchange stiffness constant *A* and the saturation magnetization. It has been calculated that critical diameters for inhomogeneous nucleation for long cylinders of α-Fe, Co and Ni, are ∼15, ∼25 and ∼40 nm, respectively. Some other non-common reversal modes such as buckling and fanning become active under certain conditions as well [Alberto 2009].

2.8.3 Coercivity and reversal

If we have only one single domain magnetic particle the field needed to switch its magnetization from one direction to the other is the coercive field. The coercive field, H_c, has been discussed in the section 2.3.1 of this chapter. This characteristic like the others is strongly size dependent, as illustrated in Figure 2.15. The size dependence of the coercivity in single domain is due to the different mechanisms by which the magnetization reverses and have been detailed in the preceding sections. There is a progressive decrease in coercivity by reducing the particle size in single domain region which is linked with the thermal effects and ultimately to *superparamagnetism* where coercivity is zero. There may be a region between

single domain and multi-domain where coercivity falls due to vortex magnetic order, and finally, for multi-domain particles the reversal is by domain wall motion.

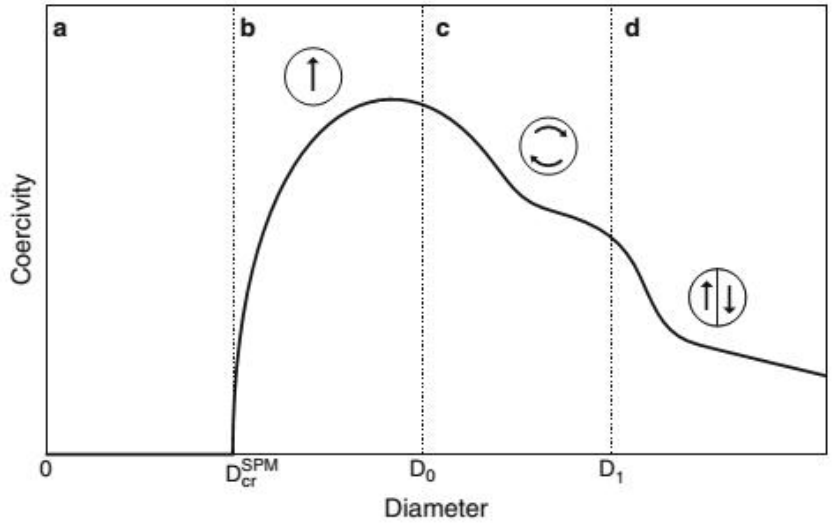

Figure 2.15: Curve of coercivity vs. size of magnetic particle, showing four regimes: (a) superparamagnetic $0 < D < D_{cr(spm)}$, (b) ferromagnetic single-domain, Dcrspm $< D < D_0$, (c) vortex state, for $D_0 < D < D_1$ and (d) multidomain, for $D > D_1 = D_{cr}$ [Alberto 2009]

2.9 Overview of MFM studies on magnetic NWs

Years before the invention of scanning tunneling microscope (STM) by Binning and Roher from IBM in 1981, Russell Young demonstrated in 1972 the surface imaging technique by measuring the current between the sample and the scanning probe [Young 1972,Binning 1981]. The quest to obtain the atomic resolution for surface characterization and its achievement in 1983 by the inventors of the STM won them a Noble Prize “for their design of the scanning tunneling microscope” [Binning 1983, Noble prize 1986].

Although STM represents an excellent way to characterize surfaces, it has certain limitations such as use of conducting samples and a strict operation requirement. This led to the invention of the atomic force microscopy (AFM) that enables the imaging of surfaces of various types of samples under ambient conditions [Asenjo 2001]. Magnetic force microscopy (MFM) is one of the operational modes of the AFM. The special magnetic probe, is brought close to a sample and interacts with

the magnetic stray fields emanating from the surface. The strength of the local magnetostatic interaction determines the vertical motion of the tip as it scans across the sample. MFM was introduced shortly after the invention of the AFM [Martin 1987]. Since the early 1990s, it has been widely used in the fundamental research of magnetic materials, as well as the development of magnetic recording components.There were several reports on studies of magnetization reversal mechanisms in NWs by various techniques at the tail end of twentieth century. However the succeeding sections on NWs cover only the prominent reports of using MFM as a characterization tool to extract the valuable information about their properties.

The operating principles of MFM are the same as in atomic force microscope (AFM). Figure 2.16 describes the basic mechanism of image acquisition. The cantilever, incorporating the tip, is excited close to its resonance frequency with certain amplitude. The deviation of a laser beam reflected off from the cantilever end onto a deflection sensor allows measuring the vibration amplitude of the cantilever. The cantilever roughly behaves as a forced damped harmonic oscillator and its resonance frequency is modified by the force field acting on the tip. In MFM, a tapping cantilever equipped with a special tip (magnetic) is first scanned over the surface of the sample to obtain topographic information. Using Lift-Mode, the tip is then raised just above the sample surface. The surface topography is scanned while being monitored for the influence of magnetic forces using the principle of force gradient detection. The cantilever is excited close to its resonance frequency with certain amplitude. Magnetic forces shift the resonance frequency of the cantilever; amount shift is proportional to vertical gradients in the magnetic forces. The attractive or the repulsive forces between the sample and magnetic tip are noted by measuring the phase-lag which is inversely proportional to the force gradient as shown in the equation below.

$$\Delta\Phi \propto \frac{-Q}{k}\frac{\partial F}{\partial z} \tag{2.12}$$

Q is the cantilever quality factor and *k* its stiffness. Therefore, attractive forces with a positive gradient lead to a negative phase-lag (dark contrast) and repulsive forces with a negative gradient lead to a positive phase-lag (bright contrast). Section 3.2.3 describes the basic mechanism of image acquisition in details.

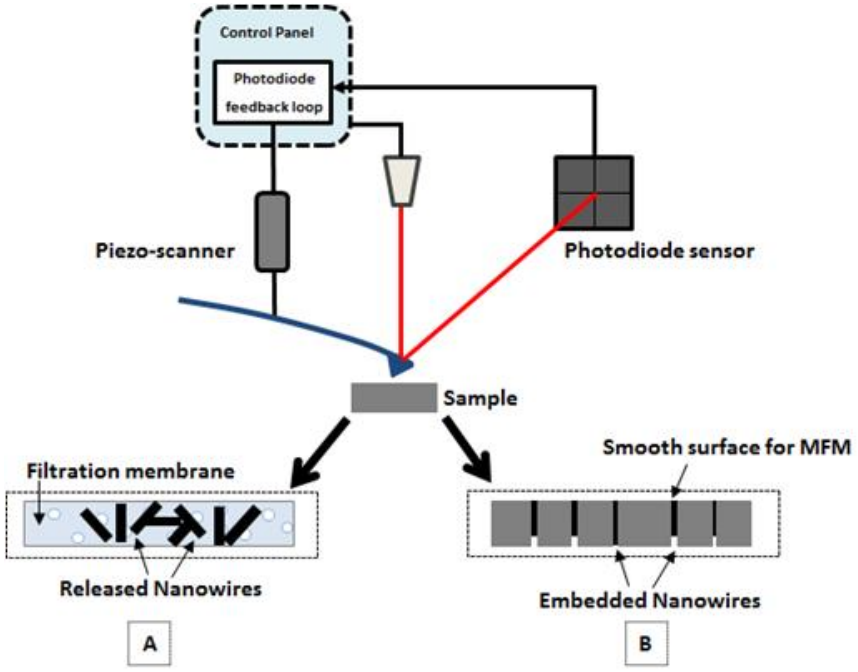

Figure 2.16: Schematic description of an atomic force microscope showing the samples for MFM, released NWs from the template and the embedded NWs in template.

2.9.1 *Ex-situ* MFM studies on NWs

The intrinsic differences between the magnetization reversal mechanisms of Ni and Co NWs of different diameters using magnetometry and numerical studies were reported by Ferré et al. [Ferré 1997]. Square hysteresis curves were observed for Ni for various diameters (35nm -500 nm) whereas only for small diameters (less than 50 nm) in Co wires. It was demonstrated that there was strong and negligible crystal anisotropy in Co and Ni NWs respectively. This fact led to the orientation of the magnetization along the long axis in Ni wires whereas in Co, multidomain magnetization configuration was considered in wires of diameter equal or larger than 100 nm due to orientation of *c* axis of the hexagonal close packed structure perpendicular to the wire axis.

Further, micromagnetic calculations in that study provided the accurate description of the above fact. This finding triggered the use of MFM to study the magnetization of individual and isolated Co NWs released from the templates [Belliard 1998, Fert 1999, Henry 2001]. The MFM results proved the already made assumptions by Ferré that magnetocrystalline anisotropy affected the domain formation in NWs as shown in Figure 2.17.

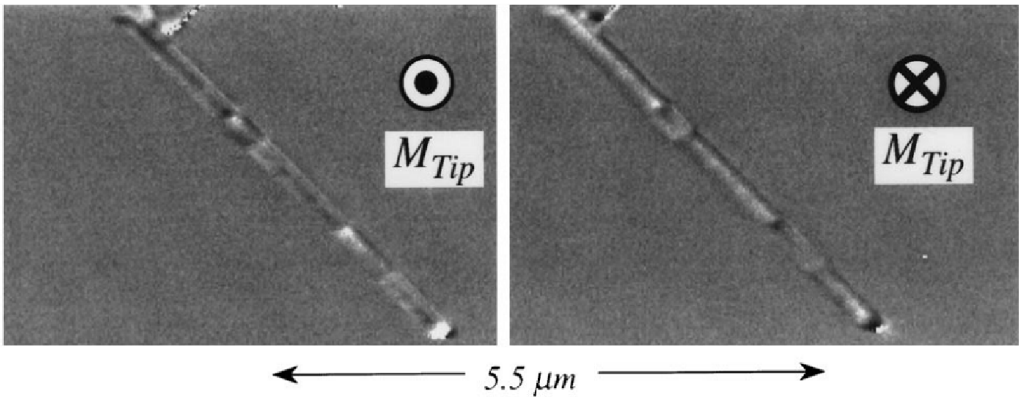

Figure 2.17: MFM images of bamboo type structure in a pure Co nanowire of diameter ~ 80 nm. Note the contrast switching with tip magnetization reversal. [Belliard 1998]

From one segment to the next, it is assumed, in agreement with the measured texture, that the c-axis rotates in such a way that it basically remains in a plane perpendicular to the wire's axis. Recently Sun et al. showed by MFM characterization that Ni NWs of 250 nm stay single domain whereas they show core-shell cylindrical magnetic domains at a diameter of 2 µm [Sun 2009]. Formation of single domains and its dependence on the critical radius has already been discussed in section 2.5.

Fert et al. presented a comprehensive review, compiling the finding of 1990's, not only on single component but also on multilayer magnetic NWs deposited in pores of polymer templates [Fert 1999]. The authors described the magnetic properties of the arrays as well as of the isolated electrodeposited NWs. The decrease in squareness and coercivity was observed with increasing diameter. For the Co wires with diameter larger than 75nm reversal is shown to be triggered by several nucleation sites. The MFM results presented in this review supported the findings of other researchers that Ni is a single domain wire from diameter 20-500 nm

whereas Co exhibited the complex domain structure with the co-existence of axial and transverse domains for diameters larger than 50 nm. Further in depth investigation was done by Garcia and co-workers and it has been depicted in Figure 2.18 that Co NWs show single domain behavior only below 50nm [Garcia 2002].

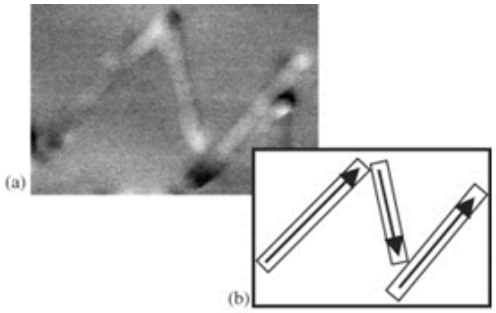

Figure 2.18: MFM images of single domain Co nanowires of diameter ~35 nm and their schematic interpretation (a, b) respectively. [Garcia 2002]

2.9.2 *In-situ* MFM studies on arrays of high density NWs

Asenjo et al. presented MFM as a widely employed technique to observe the magnetic domains and walls in modern magnetic materials [Asenjo 2001]. This overview covered the basics of domain formation, instrumentation and operation modes, interpretation of MFM results and representative images from thin films, magnetic data storage, amorphous and nanocrystalline alloys and nanowires. It was mentioned that despite it was a newly developed technique, it got a valuable position in magnetic characterization at nanoscale. While studying the longitudinal magnetic bits (data storage technique of that time) the authors claimed that the MFM may also be a useful technique to test the thermal stability of the recorded information.

Nielsch et al. used alumina membrane to grow, high density ~ 10^{12} per cm^2, ordered porous arrays of Ni NWs using electrodeposition [Nielsch 2001]. A complete pore filling for the sharply defined 30 nm diameter and 100 nm pitch was achieved which was a challenge for track etched polymer templates due to randomness of pore distribution (Figure 2.19a).

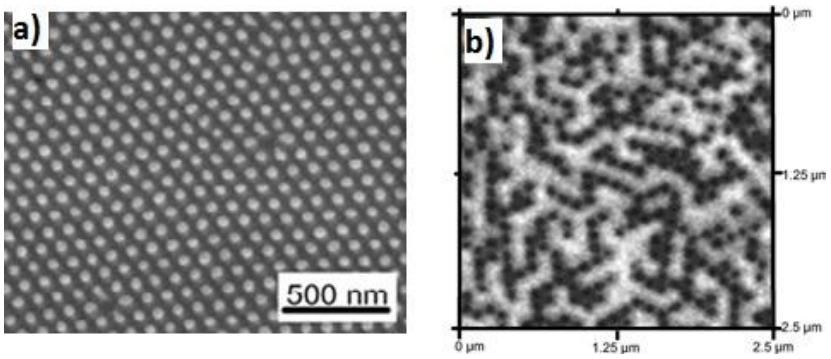

Figure 2.19: Top view SEM micrograph of Ni filled alumina matrix (a) and MFM image of a demagnetized sample (b) showing the magnetization of the pillars "up" (white) and "down" (black) [Nielsch 2001].

In some studies on effects of intrinsic parameters on magnetic properties of the NWs, not only the coercivity and remanence but also the switching field was found to be dependent upon the homogeneity of the template filling, alloy composition and aspect ratios [Vazquez 2004, Navas 2005]. Vazquez et al. declared that the tilt in the hysteresis curve of disordered systems was the consequence of strong interactions, hence reinforced the conclusion drawn by previous studies.

Further investigation of the weight of geometrical parameters using magnetic field sweeping MFM demonstrated that the transition from coherent to curling reversal was observed for NiFe NWs of width 10 nm to 150 nm respectively whereas the magnetization process changes from domain wall motion and pinning (below 500 nm) to domain wall motion at 800 nm as shown in Figure 2.20 [Adeyeye 2008, Endo 2008]. These results supported the already made assumptions that the magnetization reversal process alters by changing the size/width of nanostructures.

Nielsch et al. showed that MFM magnetic characterization agreed well with the bulk measurements. It was shown that switching of the individual single domain NWs was affected by the stray field generated by the nearest neighbors called demagnetizing field. The labyrinth pattern of the domain structure of the hexagonal packed NWs arrays in the demagnetized state (Figure 2.18b) was the result of the dipolar interactions. It was concluded that the stray field from the wires was extended over several inter-wire distances due to their high aspect ratio. It was illustrated schematically that the parallel alignment of the two single domain

neighbors is unfavourable as the dipolar field forces the nearest neighbors, dipole-dipole interaction decrease with a power of 3 of the distance, for an antiferromagnetic alignment.

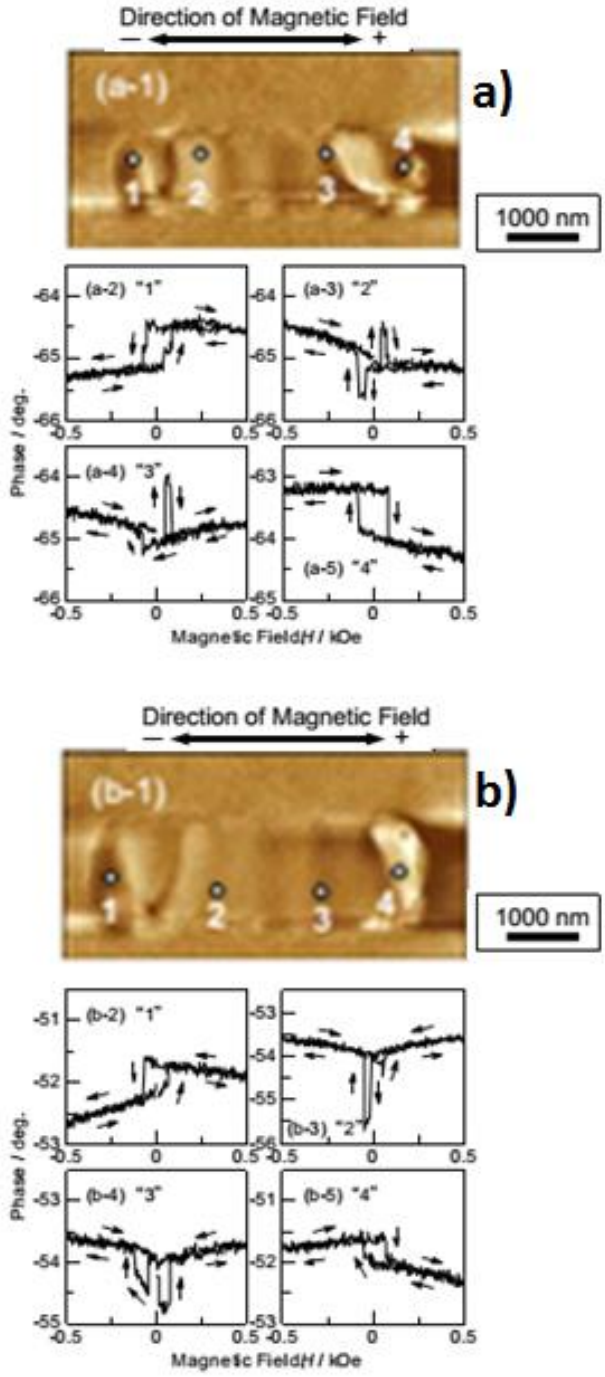

Figure 2.20: MFM images in a zero field of 30-nm-thick Ni-Fe nanowires with the widths of (a-1) 300 and (b-1) 500 nm. Points 1-4 indicate measured points within the nanowire. Curves of phase vs. magnetic field (H) for various points in the Ni-Fe nanowires with the widths of (a-2)-(a-5) 300 and (b-2)-(b-5) 500 nm measured by MFS-MFM. The magnetic field is applied in the longitudinal direction of the nanowire.

The impact of the dipolar interactions is to affect the liberty of switching events of neighboring NWs. Broadening of the SFD is one of the outcomes of dipolar field. To look at the influence of external parameters, namely of dipolar fields, on magnetic switching of wires became the motivation for the researchers. Sorop et al. performed the MFM measurements on single domain densely packed Fe NWs [Sorop 2003].

They decomposed the macroscopic hysteresis curve into microscopic curves in terms of irreversible magnetic response of individual NWs using MFM. The single wires had always the square hysteresis (Figure 2.21) whereas in the assembly of wires there was an asymmetry of the hysteresis curve which found its natural explanation in the dipolar field generated by the neighboring wires. The average of interaction field coefficient measured from different single NWs is of the same order as the broadening/asymmetry of the macroscopic curves. It was concluded that the switching field of a wire will be different depending upon its magnetization orientation and the distance with the neighbors.

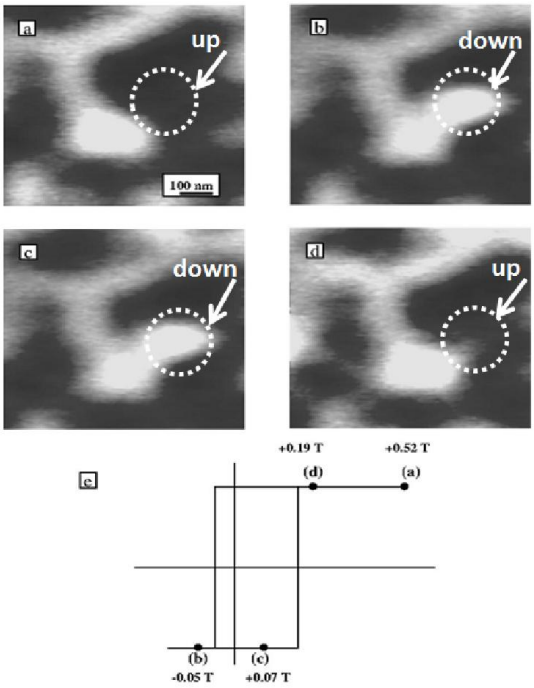

Figure 2.21: MFM images after applying magnetic fields of various amplitudes showing one NW switching the magnetization (a-d). The corresponding single NW magnetic hysteresis curve (e) [Sorop 2003]

The phenomenon of SFD broadening was quite similar in magnetic nanodots as well. The SFD of single bit in dense arrays of Co/Pd in bit patterned media (BPM) was analyzed using high resolution MFM by Chen et al. [Chen 2012b]. The intrinsic SFD contributed only 20-50% of the total indicating SFD broadening. MFM images showed that 50% or even more of the SFD contribution resulted from non-intrinsic parameters i.e. dipolar interactions. It was pointed that the single bits could switch in a very narrow range of applied field as small as 5 Oe as shown in Figure 2.22. The results indicated that even the same magnetic island may have different SFD broadening depending upon the magnetization of its surrounding islands, thus evidenced the dipolar interaction contribution.

Pei et al. performed magnetization reversal study of Co-Pt nanodots and showed experimentally that the contrast intensity of the nanodots in MFM images had a strong relation with their switching fields [Pei 2011]. The model proposed to explain the broader SFD was based on the finding that nanodots have two phases i.e. inner core and outer layer which forms a vortex like structure and is the source of SFD.

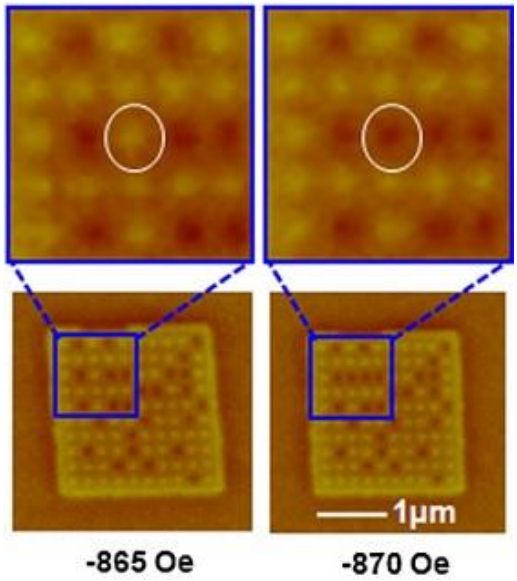

Figure 2.22: MFM images illustrating the reversal of single bit from its original "up" magnetization state to "down" state by applying only 5 Oe external field. [Chen 2012b]

In the above mentioned examples, it was shown that the broadening of the SFD was not only due to geometrical parameters and fabrication flaws but also strongly

dependent upon the dipolar interactions. The MFM study done by T.Wang et al. to analyze the switching field of Co NWs one by one and removing the dipolar interaction field effects, using high coercivity tip for in field MFM, established a base to extract intrinsic SFD of individual wires in interacting NWs [Wang 2008]. They investigated the magnetization reversal progress of ordered Co NWs array by successive *in field* MFM measurements (Figure 2.23). It was suggested that the dipolar field H_{dip}, acting on a given nanorod at a random magnetization state might be expressed as

$$H_{dip} = x \frac{M}{M_s} \tag{2.13}$$

where x represents the dipolar interaction field coefficient, M_s the saturation magnetization and M the average perpendicular magnetization which can be obtained by counting the number of reversed and non-reversed nanorods at each incremental step of applied field (Wang 2008). By removing the dipolar field effect, calculated from equation 2.13, the intrinsic SFD can be obtained for the system under study (see graphs in Figure 2.23). It can be noticed that even after removing the dipolar field, the intrinsic SFD is quite broad ~3 kOe which indicates that there is a significant contribution of the intrinsic effects in SFD broadening.

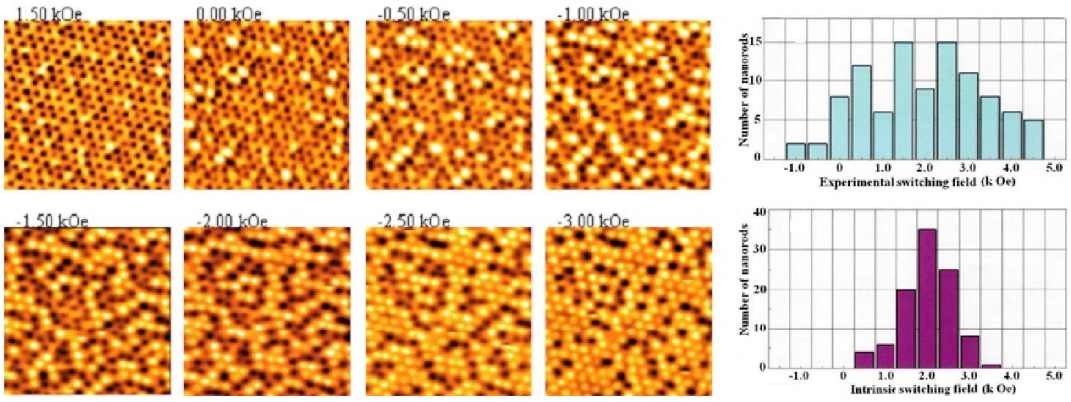

Figure 2.23: MFM images displaying the magnetization reversal progress of Co NWs with magnetization up and down. The graphs showing the switching field distribution with (above) and without (below) the effect of dipolar fields [Wang 2008].

J. Yuan et al. in a similar work on Co NWs emphasized that quite a broad distribution of SFD (~ 4 kOe) even after removing the dipolar field was due to

diameter size distribution, inhomogeneity of wire structures and dispersion of wire inter-wire separations [Yuan 2008]. The asymmetry of the hysteresis curves can be corrected, to some extent, if the dipolar field calculated using equation 1 is removed. Numerical calculations were performed to exhibit the dependence of dipolar field on diameter and pitch of hexagonal NW array. With increasing pitch and decreasing diameter the interaction field can be reduced. For instance, in an array of NWs of 10 nm the dipolar interaction field is 6 kOe, 1 kOe and 0 Oe for a pitch length of 20 nm, 40 nm and 80 nm respectively. Whereas for an arrays of NWs of diameter 20 nm, the values are 6 kOe, 1 kOe and 0.5 kOe for a pitch length of 40 nm, 80 nm and 100 nm respectively.

Piraux et al. [Piraux 2012] proposed a novel approach to get the periodic array of magnetic nanostructure by depositing Co/Pt layers on the barrier layer of ordered anodic alumina with weak exchange coupling. The oxide barrier layer, generally removed before electrodeposition in other studies, was given importance in their work as they emphasized that this layer possesses an ordered array of bumps that can be used as a pre patterned substrate (Figure 2.24). It was shown that the magnetic caps on the bumps are exchange decoupled and can be addressed one by one.

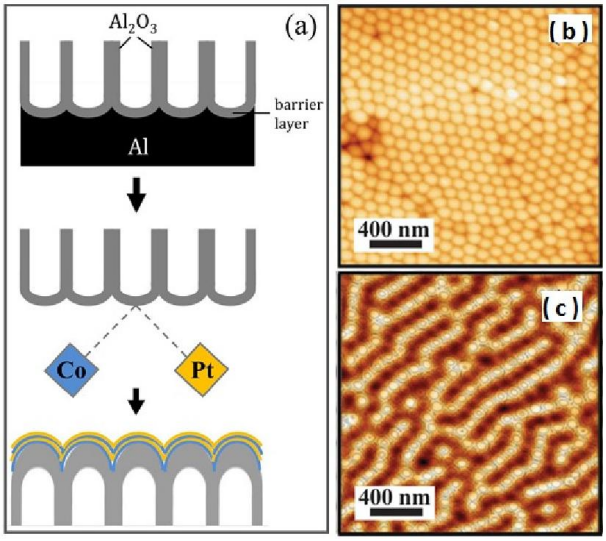

Figure 2.24: Schematic representation of the formation of 2D-ordered bumps array from the barrier-layer surface of the AAO template after a two-step anodization process, followed by sputtering deposition (a). On the right, AFM image of the bumpy surface (b) and MFM.

In the very dense Ni NWs array, MFM contrast was difficult to distinguish by counting the up and down wires (Figure 2.25a). Therefore, a qualitative method to extract the remanent magnetization by fitting the MFM data to Gaussian or Lorentzian distribution functions was proposed by Asenjo et al. [Asenjo 2006] and is shown in Figure 2.24b. Escrig et al. coupled the numerical calculations and MFM analysis to obtain the information of magnetic remanence dependence of Ni NWs on their size [Escrig 2007a]. Their model presented a way to calculate the remanence as a function of magnetic interactions in the NWs array. They also elaborated the importance of having a sufficient sample size for the reproducibility of MFM analysis.

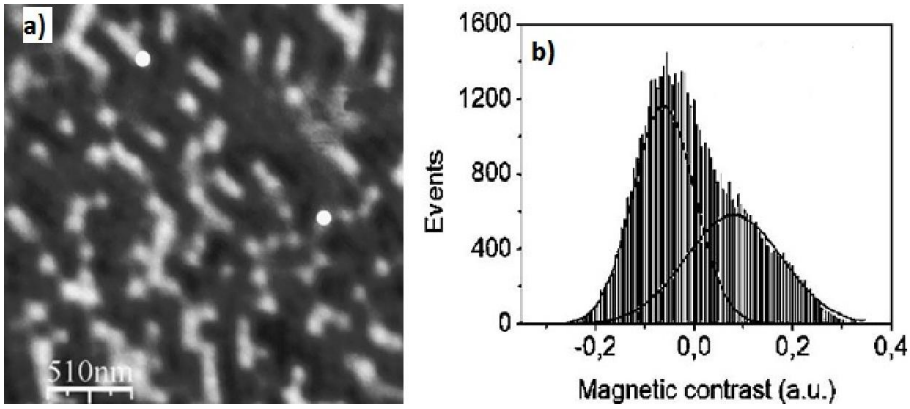

Figure 2.25: MFM image showing NWs with magnetization up and down (a) and corresponding magnetic contrast distribution (b). [Asenjo 2006]

Jaafar et al. introduced the variable external field MFM to apply the field both in-plane and out-of-plane directions of the sample (Figure 2.26 a). Considering the NWs arrays, the external magnetic field can be applied parallel as well as perpendicular. They claimed that this technique can be used not only as a characterization instrument but also for magnetic reading and writing of individual nanostructures. The wires initially saturated by an external field opposite to the tip magnetization resulted in white contrast (Figure 2.26b). By applying the magnetic field pulses of pre-selected width and intensity at any spot of the image region, switching of the NWs at particular selected spots was initiated as shown in Figure 2.26c [Jaafar 2009].

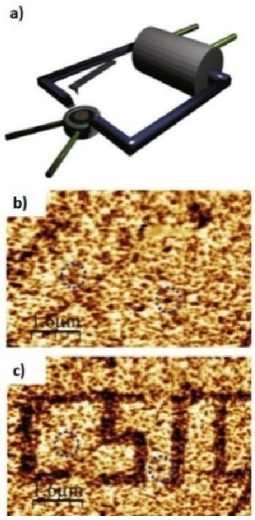

Figure 2.26: Scheme of both in-plane field and out-of-plane field coil system (a). MFM images of the Ni NW array before (a) and after the application of local magnetic fields (b). [Jaafar 2009]

2.10 MFM studies on magnetic NTs

NTs present more degree of freedom to tune their magnetic properties as they possess a hollow core but they are still quite new in the family of magnetic nanostructures and require special attention as for as their fabrication is concerned (section 2.7.2). This is the reason why they were not the subject of research from the MFM point of view. For instance, except our group and according to the best of our knowledge, MFM studies to understand the reversal behavior of individual magnetic NTs have not been done so far by other groups.

Nevertheless, the structural, magnetic and magnetization reversal properties of ferromagnetic NTs were investigated experimentally as a function of their geometrical parameters by other magnetometry techniques [Bao 2001, Sui 2004, Han 2009, Escrig 2007b, Sharif 2008, Rozman 2011, Proenca 2013, Aravena 2013]. NTs present lower magnetic interactions compared with the same diameter and same density NWs, thanks to their hollow structure [Bao 2001, Liu 2010, Proenca 2013]. It was further indicated that the physical reason of low exchange energy in NTs was the absence of curling related vortices which are present in other magnetic structures. The domain structure and the reversal mechanisms in NTs are strongly dependent upon their outer and inner diameters and the aspect ratios [Sui 2004, Landeros 2007, Usov 2007, Escrig 2007b, Daub 2007, Wang 2011, Lopez

2012, Chen 2012a, Zhang 2013b, Chen 2014]. This triggers the need of MFM characterization of the NTs as a function of their geometric parameters.

The most recent MFM characterization of individual magnetic NTs released from the templates is presented by Rozmann et al. as shown in Figure 2.27 [Rozmann 2014]. The MFM phase image (Figure 2.27a) displays a relatively uniform phase shift across the width of the nanotubes (marked with A–A*) with only a weak signal detected at the nanotubes ´ edges (Figure 2.27b). A much more significant signal is observed at the nanotubes´ bottom part (marked with B -B* in Figure 2.27c), where a clear defect due to the breaking off of the nanotube can be observed.

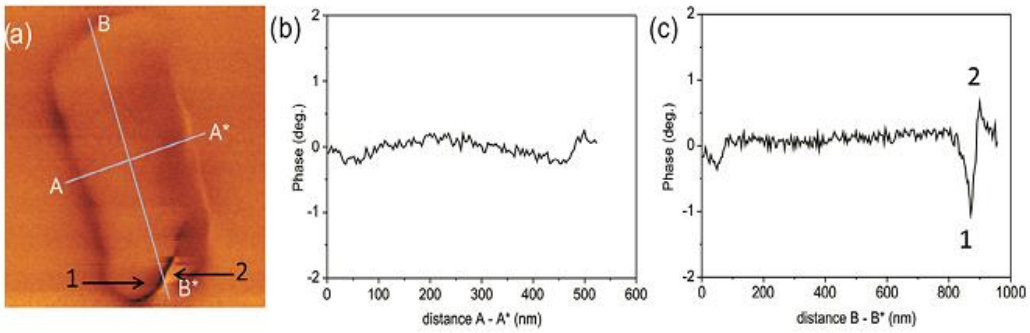

Figure 2.27: MFM Co–Pt nanotube image, arrows 1 (black contrast) and 2 (white contrast) point to the magnetic signal at the tube defect. (b) MFM phase profile across the tube width (A–A*). (c) MFM phase profile along the tubelength (B–B*), with signals coming from nanotube defects marked with 1 and 2 in (a).

The absence of a significant dipole contrast in most parts of the nanotubes suggests that the magnetization distribution is indeed in the expected circumferential direction, thus forming a flux-closure configuration without any axial contribution. Since MFM is not sensing the magnetization directly, but rather the second derivative of the sample's stray field, contrast can only be expected when magnetic charges are emanating at the surface of the sample, which creates stray fields in the exterior of the specimen.

2.11 Conclusion

The literature review presented herein made it clear that, in interacting arrays of magnetic NWs and NTs, the observed SFD is the sum of intrinsic parameter effect such as geometry, composition etc. and of extrinsic parameter effects such as

dipolar interactions. To use these magnetic nanostructures in novel devices, there is a basic need of understanding the magnetization reversal process and of controlling the SFD. As mentioned in the previous sections, efforts have been made to understand magnetization switching and to extract the intrinsic switching fields, from data on high density NW arrays, using certain corrective formulas. Experimental studies on isolated, non-interacting arrays of NWs/NTs to have an insight into their intrinsic properties have been rarely performed. Therefore, we came up with the idea of starting MFM measurements on dilute arrays of NWs and NTs where dipolar interactions were negligible and then moving towards the medium packing density arrays. The objectives of these studies, along with generating a model system for MFM in which we can apply *in situ* magnetic fields during the measurements, include:

1) Determining the magnetization reversal progress and SFD of non-interacting (i.e. absence of dipolar coupling) single domain ferromagnetic NWs/NTs arrays as synthesized using track-etch polymer template. Further, measuring the impact of a) different magnetic materials (Ni, $Ni_{1-x}Fe_x$ and $Co_{1-x}Fe_x$), b) the effect of different morphologies (i.e. solid cylinders and hollow cylinders) and geometrical parameters (like the diameter) on the magnetic properties.
2) Comparing MFM results with bulk magnetometry technique AGFM and with micromagnetic simulations to quantify the magnetic response from individual and from arrays of magnetic NWs/NTs.
3) Exploring the influence of varying the interwire distance on the magnetization reversal of the nearest neighbors.

The experimental strategies to reach the above said goals are presented in chapter 3. The results in the subsequent chapters will cover the outcomes of recent works and will give a glimpse of how these objectives have been achieved.

Chapter 3
Materials and methods

This chapter focuses on the fabrication of the samples and on the different characterization techniques used during the course of the study. The templates used were track etched polycarbonate (PC) membranes. The fabrication of the magnetic nanowires (NWs) and nanotubes (NTs) was done using the electrodeposition process. The magnetic characterization was carried out using alternating gradient force magnetometry (AGFM) and magnetic force microscopy (MFM) whereas finite element method magnetic (FEMM) package was used to execute numerical calculations. Structural characterization was performed with scanning electron microscopy (SEM). The chapter describes how the samples were prepared for MFM analyses, the adaptation made to the MFM set up to perform *in situ* and *in field* experiments, the procedures used to extract parameters such as the switching field distribution or the interaction field. It also addresses the optimization of the probe choice and of the imaging procedures.

3.1 Materials

A template, in general, is a pre-designed structure within which a network exists for further utilization. Nuclear track pores find diverse applications as templates for synthesis of micro and nanostructures. Though this technique produces randomly distributed pores, it allows controlling the size, shape and density of pores created over a wide range of values. Indeed, sizes of 10 nm to several micrometers, with a length to diameter ratio between 10 and 1000 are possible, and the pores density can range from 10^5 to 10^{11} cm^{-2}. During this study PC membrane, provided by

Etienne Ferain (it4ip) [Ferain 2003], containing pores of diameter ranging from 40 to 150 nm have been used as templates. The thickness of the used membranes was 21 µm and the diameter size distribution of ± 5 nm. Table 3.1 summarizes the characteristics of the PC templates.

3.1.1 Electrodeposition in PC templates

Electrodeposition was used to fabricate the arrays of NWs and NTs in PC templates. Before starting the process of deposition a thin Au layer, was sputtered on one side of the membrane. The thickness of this film was always three times larger than the pore diameter in the PC membrane. To improve the adhesion of Au with the PC membrane a 5 nm layer of Cr was first deposited. This conductive Cr/Au layer served as cathode during the subsequent electrochemical deposition of the metal in the nanopores.

Table 3-1: Characteristics of the PC templates used in this thesis: membrane thickness, average pore diameter and porosity.

Thickness (µm)	Diameter (nm)	Porosity (%)
21	40, 50, 70, 100	<1
21	40	~ 4
21	100	~ 12
21	150	~ 6
21	150	~ 10

The experimental set-up for electrodeposition is presented in Figure 3.1. The template was first attached to the cathode of the electrolytic cell and was then brought in contact with the deposition solution in which a Pt anode and a reference electrode were dipped later. The reference electrode was used to monitor the applied voltage. In our experiment an Ag/AgCl reference electrode was used and the electrodeposition of NW arrays was carried out into a Teflon cell using a EG&G Princeton Applied Research potentiostat model 263.

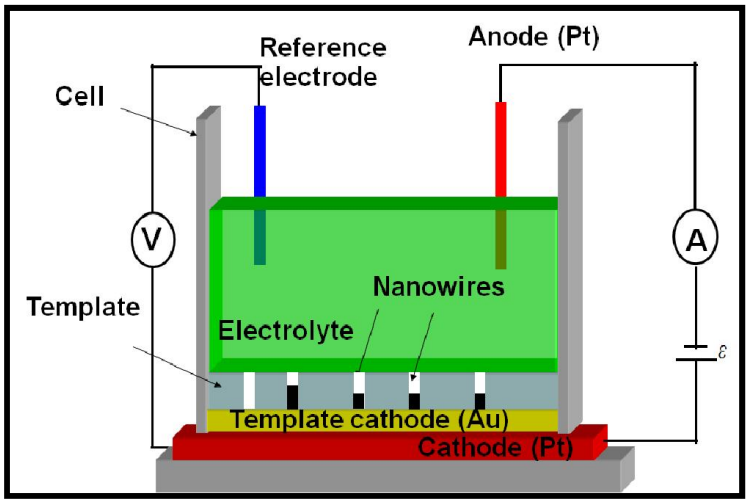

Figure 3.1: Schematic representation of the electrodeposition cell containing the porous template in contact with the cathode and filled with an electrolyte.

The electrodeposition was initiated by the application of a potential bias between the cathode and the anode. When an electric field is applied, cations diffuse toward and reduce at the cathode, resulting in the growth of nanowires inside the pores of the template. The nanowires grew inside the pores of the membrane from the cathode because the electrolyte was confined to the exposed side of the membrane. The electrons necessary for the metallic ions to deposit are provided by the cathode. The potentiostat measures the electrodeposition current and the voltage applied between the anode and the cathode. Figure 3.2a shows the current density at different deposition stages when a constant potential bias is applied.

During the electrodeposition, the voltage was kept at constant value depending upon the metal or alloy to be deposited, while the evolution of the current between the anode and the cathode was used to measure the progress of the nanowires growth. The current passing between the anode and the cathode depends on the effective area of each of those electrodes. As the area of the anode does not change, if the temperature and the electrolyte composition do not change significantly, the electrodeposition current depends only on the area of the electrodeposit. The three stages of this process can be identified in the evolution of the current with time (Figure 3.2).

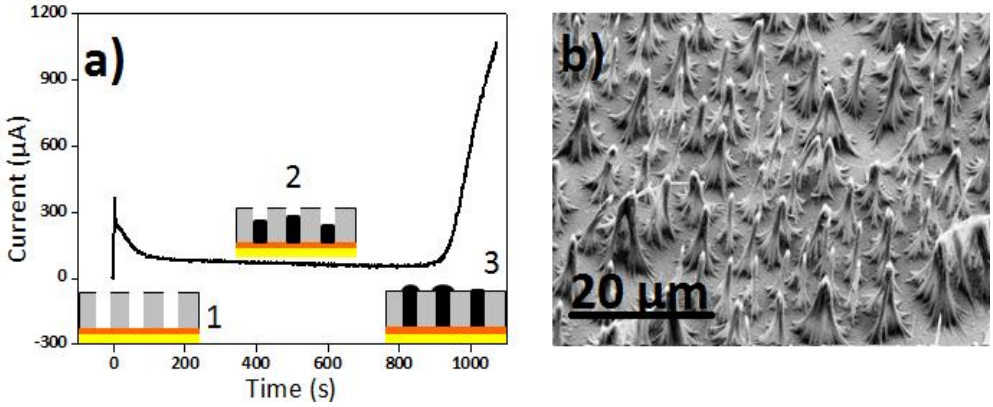

Figure 3.2: a) Current as a function of time corresponding to the electrodeposition of an array of NiFe NWs in potentiostatic mode at a potential of -1.05 V. Different stages are indicated with numbers. b) Deposited wires after PC dissolution.

The nucleation and the germination occurs in the virgin template at the start (Stage 1), showing the sudden increase in the current which is due to the difference between the equilibrium potential of the ions in solution and the applied potential. The wires then grow inside the pores (Stage 2) with the current remaining approximately constant due to the equilibration of the ions concentration and since the surface of the deposit is simply the sum of the areas of the pores. The constant current value in this stage depends upon the pore size and pore density. When the deposit reaches the surface of the membrane, the current increases rapidly (Stage 3) because the pores are filled and the metal begins to deposit as caps at the end of the wires. The electrodeposition was stopped before the stage 3 to avoid overgrowth out of the membrane. Figure 3.2b shows electrodeposited wires released from PC template.

For the fabrication of the NW arrays studied in this work, different electrolytes have been used based on Co, Ni, Cu and Fe sulfates in deionized water. Apart from these sulfates, each solution contains boric acid (H_3BO_3) which serves as pH buffering agent, improves the electric conduction and helps avoiding parasite reductions at the cathode like the hydrogen ions reduction ($2H^+ + 2e^- \rightarrow H_{2(g)}$). This chemical reaction modifies the solution pH, which has significant influence on the morphology of the deposited material. A considerable amount of boric acid ensures a stable solution pH which was maintained at 3.8 for all the solutions. The specific

solution pH can be controlled by adding sulfuric acid (H_2SO_4) or sodium hydroxide (NaOH) [Darque 2006].

Apart from deposition of pure materials, there is the possibility of depositing alloys of two or even more different ionic species e.g $Ni_{80}Fe_{20}$. The solutions of Ni, Ni-Cu, $Ni_{80}Fe_{20}$ and $Co_{55}Fe_{45}$ used in this work to deposit different metallic nanowires are shown in table 3.2.

Table 3-2: The composition of the electrolytic bath and specific deposition potential.

Deposited Material	$NiSO_4.6H_2O$ (g/l)	$FeSO_4.7H_2O$ (g/l)	$CuSO_4.5H_2O$ (g/l)	$CoSO_4.6H_2O$ (g/l)	Ni (H_2SO_3).$6H_2O$ (g/l)	H_3BO_3 (g/l)	Deposition Bias (V)
Ni	262.84	--	--	--	--	20.30	-1.1
Ni-Cu	--	--	12.48	--	90.7	4.6	-1
$Ni_{80}Fe_{20}$	131.42	5.56	--	--	--	24.73	-1
$Co_{55}Fe_{45}$	--	40	--	80	--	30	-0.9

Ni NTs were fabricated using a two-step procedure as depicted in Figure 3.3a. The process started by growing simultaneously Ni/Cu core/shell NWs at a constant potential of −1.0 V using a 0.4 M Ni (H_2NSO_3)•$4H_2O$, 0.05 M $CuSO_4$•$5H_2O$ and 0.1 M H_3BO_3 electrolyte. The Cu core was later electrochemically etched at a potential of + 0.2 V [Wang 2005, Tabasum 2014]. The corresponding SEM images of the NTs embedded in the template and released from the template have been shown Figure 3.3 b-d. The details of how to prepare the sample for SEM imaging can be found in section 3.2.1.

One should note that the wall thickness of the NTs can be controlled by varying deposition potential. It has been shown that by modifying at the deposition potential of -0.82, -0.86, -0.90 and -1.00 V, the wall thickness of the NTs is 10, 25, 45, and 65 nm respectively [Wang 2005]. This shows that the Ni deposition rate increases by decreasing the deposition potential. In further studies the same phenomenon has been demonstrated for NiFe [Wang 2011].

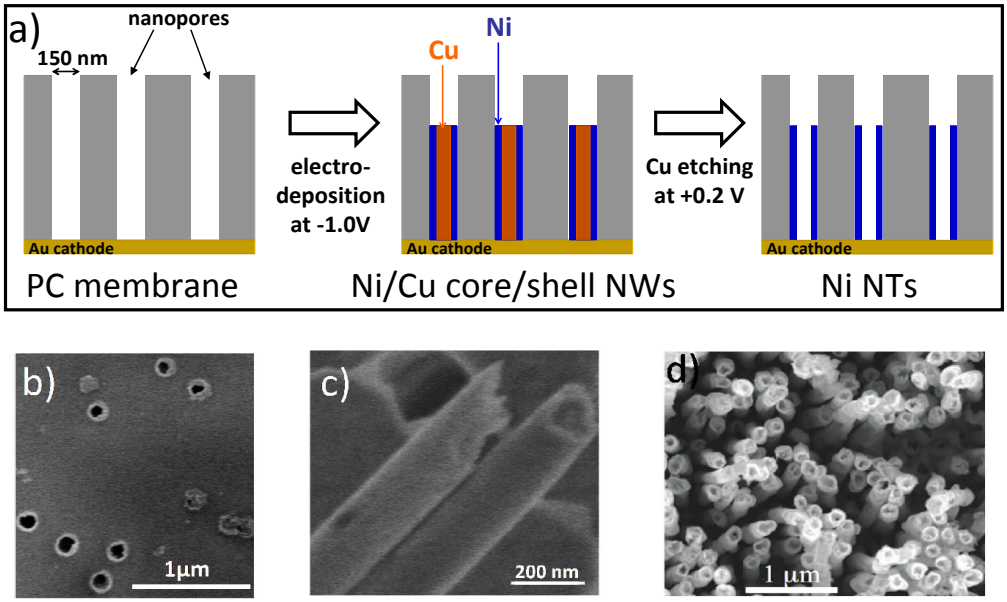

Figure 3.3: a) Sketch of the NTs fabrication process presenting the two different steps, b) SEM images of Ni NTs in the PC membrane after etching the metal cathode, c) of two Ni NTs after the dissolution of the PC membrane and d) of a large number of NTs obtaine

NWs of not only different materials but also of various diameters have been produced. The packing density "*P*" of the samples was also varied. For NTs we have produced structures with external diameter of 150 nm and of various "*P*". Table 3.2 presents various samples used during this study. The term packing density *P* in this table is explained in section 3.1.3.

3.1.2 Sample preparation for MFM measurements

As it has been stated in the preceding section the electrodeposition was stopped before the NW start growing out of the template and form inter connected wires as caps. Nevertheless, as all the wires do not breed at a uniform rate, the top surface of the PC-template was not used for MFM characterization. Hence, after electrodeposition, the sample was turned over to remove the gold and chromium layers by chemical etching in order to obtain a smooth surface where all the nanowires tips are close to the surface (Figure 3.4). The extremity of the nanowires may be imaged while keeping them in the template. The surface prepared by this procedure could also be used to characterize the sample using SEM to verify the growth of the nanowires inside the holes.

Table 3-3: Various samples used during this study.

Samples	Diameters (nm)	Packing density (%)
Ni NWs	40, 50, 70, 100	<1
	100	~12
	150	~ 6
	150	~10
$Ni_{80}Fe_{20}$ NWs	40,50,70,100	<1
	40	~4
$Co_{55}Fe_{45}$ NWs	40,50,70,100	<1
	40	~4
Ni NTs	150	~ 5
	150	~ 9

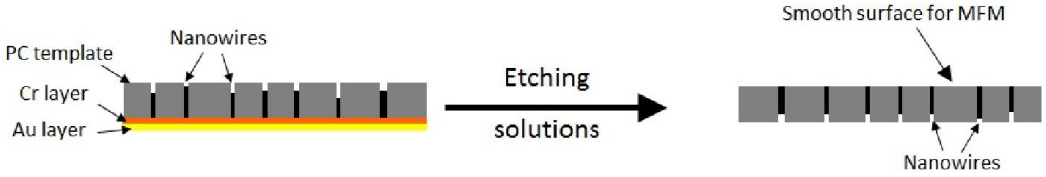

Figure 3.4: Sample preparation for MFM measurements.

To prepare samples for MFM investigations, the metallic cathode was first removed by dipping the sample into a 100 g/l KI + 25 g/l I_2 solution to etch the gold layer. The remaining Cr layer was either scraped off using a scalpel or etched using a Cr etching solution composed of 52g $KMNO_4$ in 600ml of 5M NaOH in H_2O. This step is very crucial as if the surface is exposed to the Cr etching solution, containing NaOH, for a long duration it will result in an attack on the PC membrane [Karim 2011]. This phenomenon has been observed and shown in Figure 3.5. Large etching time during Cr-etch resulted in rougher surface with the nanorods sticking out of the surface. Therefore, etching time has to be short, less than half a minute. The Au layer takes more time to be dissolved but this process has no side effects on the

sample surface since the solution used for this process does not damage the membrane.

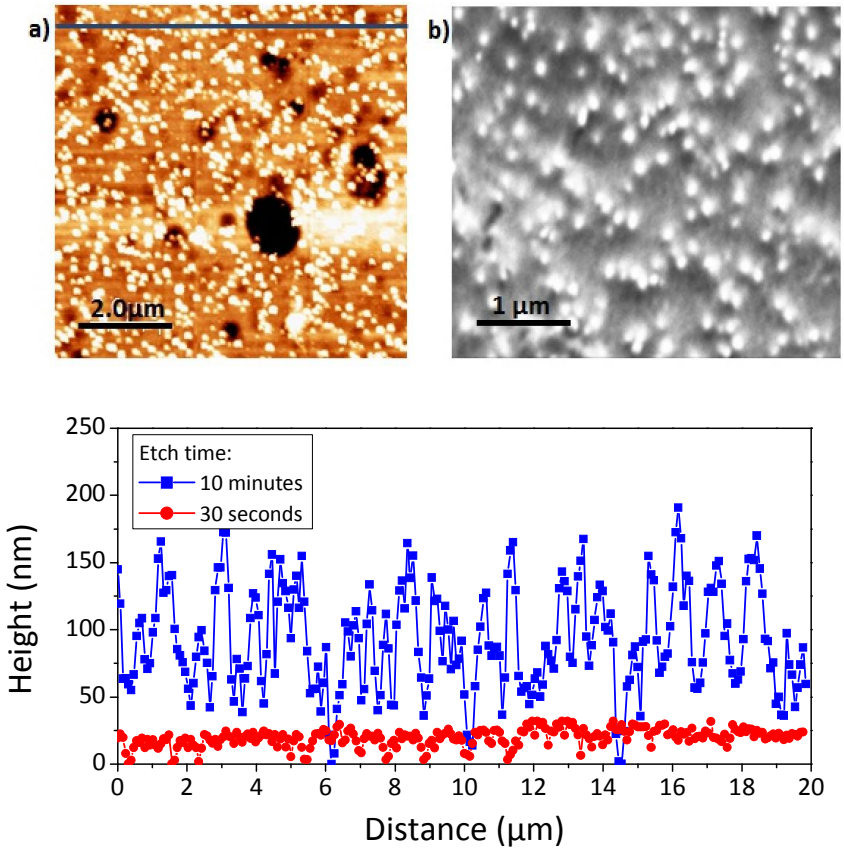

Figure 3.5: a, b) Topography as measured by MFM and SEM after etching the cathode layer, c) effect of appropriate etching time (30 seconds-red dotted line) and extended etching time (10 minutes-blue peaks) on the topography details which correspond to the dark gray horizontal line on top of (Figure 2.15a).

3.1.3 Packing density and inter-wire distance

The porosity or the pore-density (P_{pores}) of a template is simply the ratio of surface area of the pores (S_{pores}) in a given surface divided by the total surface area ($S_{template}$) under consideration and can be written as:

$$P_{pors} = \frac{N_{pores} S_{pores}}{S_{template}} \tag{3.1}$$

where N_{pores} is the number of pores. Generally, after the electrodeposition of NWs, almost all the pores of the template are filled therefore the pore-density is approximately the same as packing density (P) which is defined in the below equation as:

$$P = \frac{N_{NW} S_{NW}}{S_{template}} \quad (3.2)$$

where $N_{NW} (\approx N_{pores})$ is the number of NW, $S_{NW} (\approx S_{pores})$ is the surface area of the deposited NW. However sometimes depending upon the diameter of the nanopores, the packing density (*P*) may be quite different from the pore-density (P_{pores}). It has been shown that the packing density can be drastically low when the pore size is smaller than 20 nm [Ferrain 2003]. By counting the number of the wires of known diameter in given MFM image, the packing density can be very easily calculated using the above formula. For instance the packing density of sample in Figure 3.6a containing 300 NWs of 50 nm diameter in a surface of 20 x 20 μm^2 is ~0.15%. The samples studied in this work had always the diameter above 40 nm so there was no huge difference between the pore-density and the packing density as shown in the Figure 3.6. The packing density will be represented with the symbol *P*. The packing density in NTs array is calculated using following equation.

$$P_{NT} = P_{NW}(1 - \beta^2) \quad (3.3)$$

where $\beta = r_1/r_2$ is the ratio of internal and external radii of the NTs.

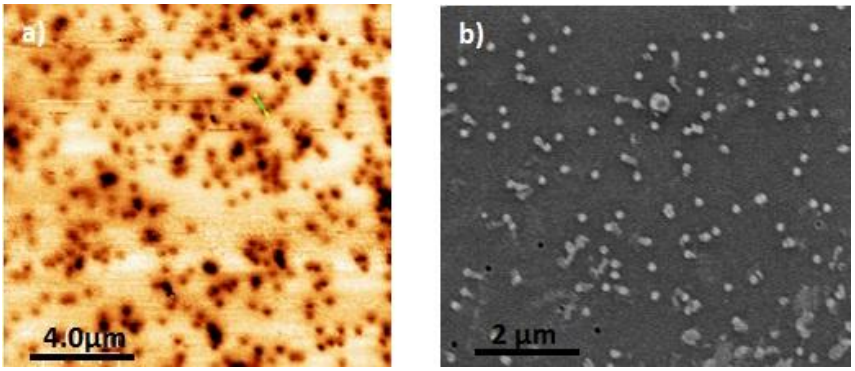

Figure 3.6: a) MFM image of NWs of 50 nm and 0.15% packing density b) SEM micrograph of 150 nm NWs array showing that the pore-density is almost the same as packing density

SEM and MFM images were used to calculate the packing density as well as the inter-wire distance (I_D). To calculate I_D, one wire was selected and the distance with its nearest neighbors was measured as depicted in Figure 3.7. This was repeated at least for four surrounding neighbors. The vertical axis of the graph in Figure 3.7 represents the signal strength whereas the horizontal axis represents the distance

between the two signal peaks i.e. between two wires. As PC membrane has random distribution of track etched pores, wires at different location on the same image were chosen to get an average inter-wire distance. For instance calculations done at various spots of the presented image in Figure 3.7 showed that the average l_D was 1 µm. This distance is not the statistical average as the wires are randomly distributed in PC membrane.

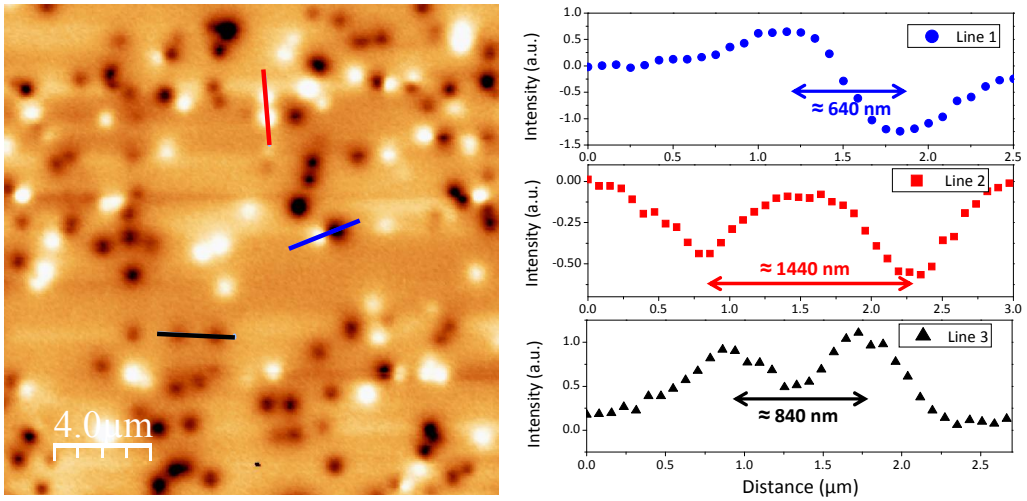

Figure 3.7: MFM image showing the chosen wires and lines to measure the inter-wire distances with one of the neighbors (left). The vertical axis of the graphs represents the signal strength whereas the horizontal axis represents the distance between the two signal.

3.2 Experimental Methods

3.2.1 Scanning Electron Microscopy (SEM)

SEM images were obtained using a FE-SEM, 982 Gemini from LEO operated at 1 kV. The samples preparation process to obtain SEM micrographs of the topography was similar as for MFM. To obtain more detailed information about the geometry of the deposited nanostructures in the membrane, it was dissolved (in our case PC). To do so, once the cathode was etched, 2 mm^2 piece of PC containing NWs was placed on a 1 cm^2 porous filtration membrane (Millipore VVLP) which was placed on a metallic sieve. This sieve was put into the mouth of a conical flask whose neck was connected to the suction pump. About 20 to 30 dichloromethane droplets were spread on the porous membrane in order to well dissolve the PC, yielding only the wires spread on it. Some minutes after, the droplets used for dissolution

were collected in the flask. This porous membrane which will act as a substrate containing NWs or NTs was then placed into the SEM chamber for structural characterization. A typical micrograph of is shown in Figure 3.8. From SEM images it can be verified that NWs diameter may have a standard deviation of ±5 nm. Figure 3.3c-d present the released NTs from the templates.

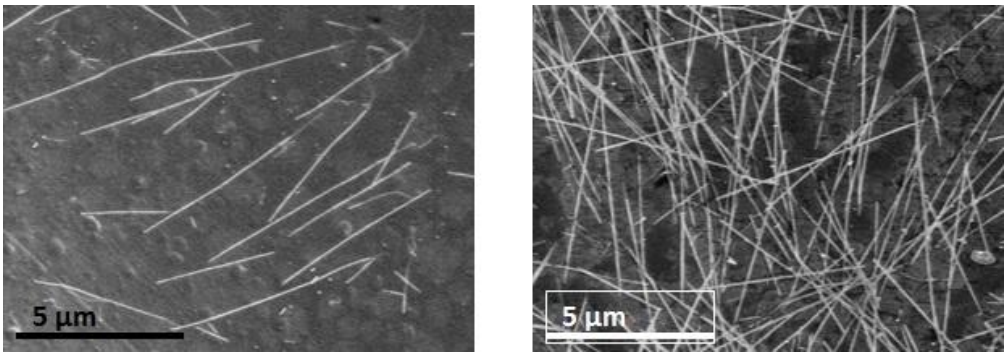

Figure 3.8: NWs released from PC templates of low packing density (left) and from high packing density (right).

3.2.2 Alternating Gradient Force Magnetometer (AGFM)

Alternating gradient force magnetometer (AGFM) allows the characterization of samples of very low magnetic moment. In this work AGFM from Princeton Measurements Corp. Model 2900 MicroMag^{TM} was used. The accuracy of the measurements was about 2 % vs. calibration with a standard reference material (SRM-2853) YIG sphere from NIST. The limiting sensitivity of this version was about 10^{-9} emu. Sensitivities higher than the other magnetic characterization instruments such as vibrating sample magnetometer (VSM) and SQUID can be achieved by mounting the sample at the end of a quartz piezoelectric probe, and subjecting it to a fixed dc field plus an alternating field gradient, produced by an appropriate coil pair, as indicated in Figure 3.9. These coils generate a non-uniform alternating field in the gap, so that a moment-bearing sample placed between them becomes subjected to an oscillating force.

The force acting on the magnetic dipole of moment $\vec{m}$ subjected to an inhomogeneous field $\vec{H}$ can be expressed as

$$\vec{F} = \vec{\nabla}\,(\vec{m}.\vec{H}) \tag{3.4}$$

The component of the force along the x-axis is thereby given as

$$F_x = \left[m_x \frac{\partial Hx}{\partial x} + m_y \frac{\partial Hy}{\partial x} + m_z \frac{\partial Hz}{\partial x}\right] \tag{3.5}$$

Totally analogous expressions are obtained for F_y and F_z components. If we consider that the field gradient is varied in *x-axis* and the dipole moment of the sample is placed in the center directed along the *x-axis* as well, then the force acting on it would be

$$F_x = m_x \frac{\partial Hx}{\partial x} \tag{3.6}$$

For symmetry reasons F_y and F_z components are zero on (*y, z*) mid plane.

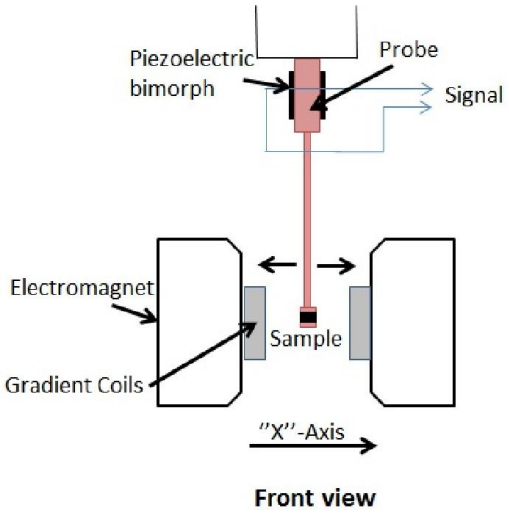

Figure 3.9: AGFM schematic.

The oscillation of the probe due to this force is detected by measuring the voltage output of the piezoelectric sensing element attached to the other end of the sample holding probe. The output signal from the piezoelectric element is synchronously detected at the operating frequency of the gradient field. As the magnetic moment of the samples depends on the magnetizing field, alternating gradient force magnetometers can be used to measure the hysteresis loop of magnetic samples. In this work, hysteresis loops have been recorded by sweeping the magnetic field in the range ±5 kOe along the wires axes.

AGFM is not only used to obtain hysteresis but also isothermal remanent magnetization (IRM) curve and direct current demagnetization (DCD) curves. IRM can be measured from the demagnetized sample by applying and removing incremental positive applied fields until the sample is saturated (open circles in Figure 3.10) and DCD curve can be measured from the remanent state obtained after saturating the sample. The successive demagnetizing negative fields are applied till the sample is saturated in opposite direction (represented by cross marks presented in Figure 3.10). These measurements can be used to extract the interaction field value on array of NWs.

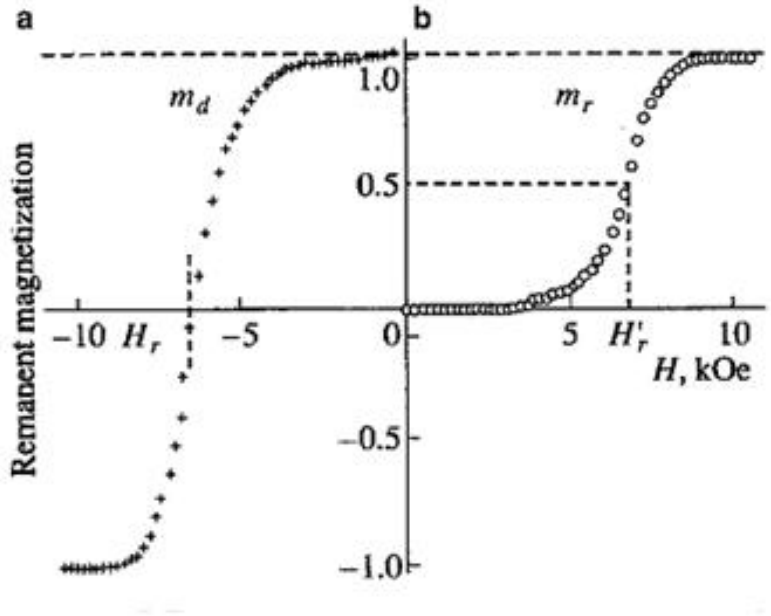

Figure 3.10: Schematic curves of, a) DCD remanent magnetization shown by cross marks and b) isothermal remanent magnetization shown by open circles.

In addition, first order reversal curves (FORC) measurements which are used to retrieve the coercivity H_c and interaction H_u parameters of arrays of interacting nanomagnets can be performed using AGFM. To achieve this, the system is first positively saturated, in order to put all the magnetization in the "up" position. The external applied field H (H_o in step 1) is then lowered until a point called reversal field (H_r), which switches "down" the magnetization of some magnetic entities, depending upon their $H_u = -(H_o + H_r)/2$ and $H_c = (H_o - H_r)/2$ parameters. Then, the field H is increased again and the magnetization M is measured. This method is shown schematically in Figure 3.11.

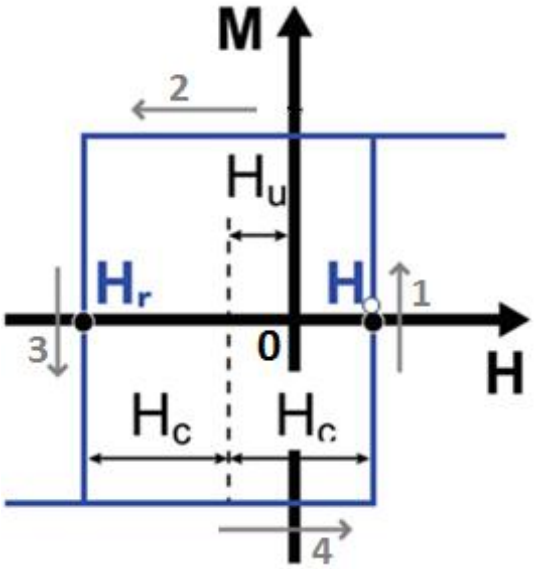

Figure 3.11: The magnetization switches down, abruptly, at H_r = -(H_c + H_u), and switches back up for a certain H_O = (H_c - H_u) value. It is completely described by the H_c and H_u parameters, which respectively represent the coercivity and the bias field, adapted from.

The FORC distribution are calculated using the below formula [Béron 2008, Pike 2005]

$$\rho(H_r, H_O) = \frac{1}{2} \frac{\partial^2 M(H_r, H_O)}{\partial(H_r, H_O)} \tag{3.7}$$

FORC diagram is a contour plot corresponding equation 3.7 and it is usually represented in (H_c, Hu) coordinates to directly obtain the coercivities and interaction fields. FORC distributions have been calculated using FORCinel software package with a smoothing factor of 1 in all cases [Harrison 2008].

3.2.3 Magnetic Force Microscope (MFM)

3.2.3.1 Introduction and basic principle

The operating principles of the MFM are the same as in atomic force microscope (AFM). Figure 3.12 describes the basic mechanism of image acquisition. The cantilever, incorporating the tip is brought in close proximity of the sample surface. The deviation of a laser beam reflected from the cantilever end onto a deflection sensor is recorded to measure the vertical displacement of the cantilever.

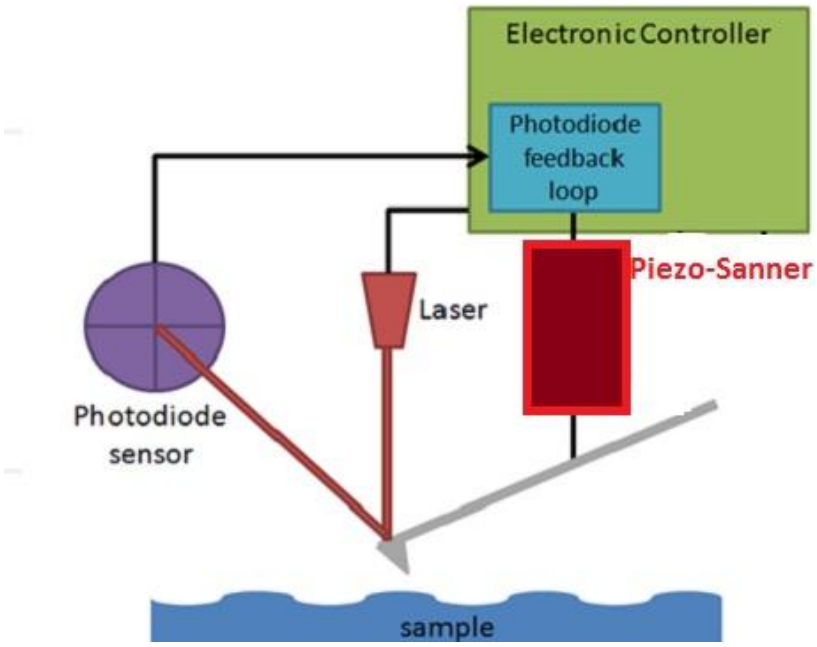

Figure 3.12: Schematic description of an AFM.

3.2.3.2 Modes of Operation

There are mainly three categories of the operation modes in AFM.

- the contact modes
- the intermittent contact or tapping modes
- the non-contact modes

In the contact mode, the tip stays in contact with the sample surface. This technique enables to map the variation of the chemical composition, the physico-chemical properties (hydrophobicity or hydrophilicity) or mechanical properties of surfaces. It was soon noticed that contact mode was not suitable to analyze the surface of soft materials and rough surfaces. To avoid this problem, non-contact modes and intermittent contact or tapping modes were developed.

In tapping modes, an oscillating electric potential is applied to the piezoelectric bimorph of the probe holder in the *z* direction, and the cantilever vibrates, thus bringing the tip to contact with the sample intermittently (Figure 3.13). This enables the scan of the topography of the soft samples. The tip is only briefly in contact with the surface and thus, friction is greatly reduced and the good lateral resolution can be obtained [Aigouy 2006].

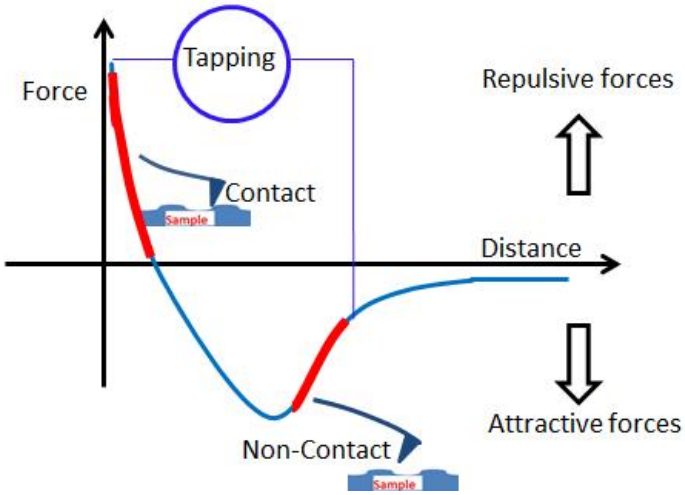

Figure 3.13: Schematic representation of tip-surface interaction force and force ranges used in different AFM modes.

The non-contact mode is generally used for the detection of long-range interaction forces. The non-contact mode can also be used to scan the topography of the sample, but the lateral resolution is not as good as with the other modes [Aiguoy 2006]. In this mode, the cantilever is excited at its resonant frequency at a sufficiently large distance from the surface to avoid any contact between the surface and the tip. This mode is also called the resonant mode. It detects the gradient of the interaction force. That is also the case with the non-contact mode.

In tapping and non contact modes, the cantilever behaves as if it has a modified spring constant under the influence of the tip-sample interaction $k' = k - \frac{\partial F}{\partial z}$, where k is the natural spring constant and $\frac{\partial F}{\partial z}$ is the derivative of the interaction force relative to the perpendicular coordinate z. It is assumed that the cantilever is oriented parallel to the sample surface. An attractive $\frac{\partial F}{\partial z} > 0$ or repulsive $\frac{\partial F}{\partial z} < 0$ interactions will shift the resonance frequency and thus the probe amplitude and phase. The most common detection method uses the amplitude signal and is referred to as amplitude modulation (AM). The cantilever is driven slightly away from resonance, where the slope of the amplitude-versus-frequency curve is high, in order to maximize the signal obtained from a given force derivative. The above mentioned force derivative could be the result from various

sources; including van der Waals , damping capillary and electrostatic interactions, MFM relies on forces that arise from long-range magnetostatic coupling between probe and sample. The topography of the sample surface is obtained by scanning the surface at constant force gradient i.e. constant vibration amplitude.

When a magnetic sample is brought in interaction with a magnetic tip, the stray field of the sample inserts a force on the tip that can be calculated using the following equation [Porthun 1998]

$$F = -\nabla E = \mu_0 \int \nabla\left(M_{tip}.H_{sample}\right)dV_{tip} \tag{3.8}$$

The origin of the magnetic interaction between a ferromagnetic tip and a magnetic surface is relatively complex to model [Wiesendanger 1994, Bonnel 2001, Meyer 2004]. The integration has to be carried out over the tip volume, or rather its magnetized part. Simplified models for the tip geometry and its magnetic structure are often used in order to make such calculations feasible. If the length of the magnetic domain at the tip apex is sufficiently small compared to the the extension of the sample stray field, one may consider that the tip has a single magnetic dipole at its apex with a magnetic moment oriented in the *z* direction, m_t [Wiesendanger 1994, Bonnel 2001]. Keeping this in view, when the tip interacts with the magnetic sample, the magnetic potential is $U_{mag} = - m_t B_z$. Here B_z is the vertical component of the local magnetic induction of the sample. The magnetic force, F_{mag} on the tip apex will be the first derivative of potential in this simplified model

$$F_{mag} = -\frac{\partial U_{mag}}{\partial z} = m_t \frac{\partial B_Z}{\partial z} \tag{3.9}$$

It can be demonstrated that the phase shift between the excitation signal and the vibration signal $\Delta\emptyset$ is proportional to the force gradient

$$\Delta\emptyset = \emptyset(\omega) - \emptyset_0 = -\frac{Q}{k_c}\frac{\partial \mathrm{F_{ts}}}{\partial \mathrm{z}} \tag{3.10}$$

Q represents the quality factor. An attractive force will thus cause a negative phase shift as its gradient is positive and vice versa. This force gradient can be written as

$$\frac{\partial F_{ts}}{\partial z} = \frac{\partial F_{mag}}{\partial z} = -m_t \frac{\partial^2 B_s}{\partial^2 z} \quad (3.11)$$

where m_t is the magnetization of the tip and B_s is the magnetic stray field from tip respectively.

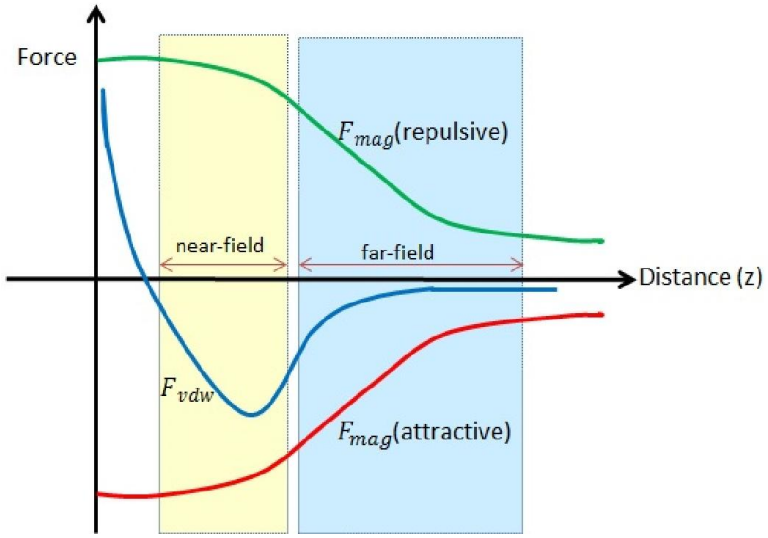

Figure 3.14: Illustration of the force in "near-field" and "far-field" acting on the magnetic tip.

The force acting on the tip while scanning the sample is sum of the attractive F_{vdw} and F_{mag}. In the far-field regime, when the tip scans the surface at a relatively large distance, typically a few tens of nanometres, both the magnetic force and its gradient are the dominant terms in the above expression (Figure 3.14). Phase shift signal has been plotted from different spots of the same image (Figure 3.15). In the absence of the magnetic field there is no phase shift as indicated by the black curve in Figure 3.15 (mark 1 in MFM image). An attractive tip sample force caused a negative phase shift as its gradient was positive, see red curve in Figure 3.15 (mark 2 in MFM image). A repulsive tip sample force caused a positive phase shift since its gradient was negative, as shown by green curve in Figure 3.15 (mark 3 in MFM image).

In the near-field regime, when the tip is scanned close to the surface, around ten nanometres, the magnetic force remains the dominant term in the tip-surface force; whereas, the force gradient is dominated by the Van der Waals force gradient as illustrated in Figure 3.13. The vibration amplitude and the phase-shift

are proportional to the force gradient and the average vertical deflection of the cantilever is proportional to the force acting on the tip [Delcorte 2013]. Based on this the lift mode is generally used to image both the topography and the magnetic properties.

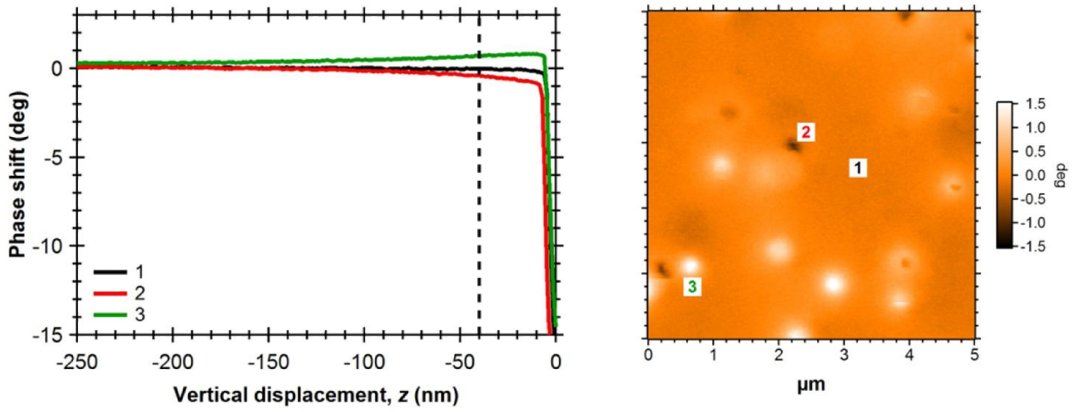

Figure 3.15: Phase shifts (left) from various spots on the same scan area (right). The positions where the curves were acquired are marked with the corresponding numbers on the images. For the curves, the abcissa (vertical displacement) were normalized to $z = 0$ for the tapping amplitude (set-point amplitude). The position for the second pass (lift height) is marked with the vertical dashed line ($z = 40$ nm).

In the lift mode (Figure 3.16), the topography is first scanned using the tapping mode. In this regime, the tip-surface interaction is dominated by the repulsive inter-atomic forces. Scanning while maintaining the vibration amplitude constant allows recording the actual surface topography with negligible effect of the other interactions (magnetic, electrostatic ...).Then the tip is lifted up at a predetermined height above the surface, typically a few tens of nanometres so that the Van der Waals interactions become negligible compared to the other interactions. During this second pass, the average tip-sample distance follows the topography that was recorded during the first pass. In this second pass, parameters such as phase shift are measured to record the magnetic properties. This double pass mode effectively decouples the topographic signal from the magnetic signal and was used in present study. We have used Agilent 5500 (Agilent technologies, USA) and ICON dimension (Bruker, USA) for our MFM experiments.

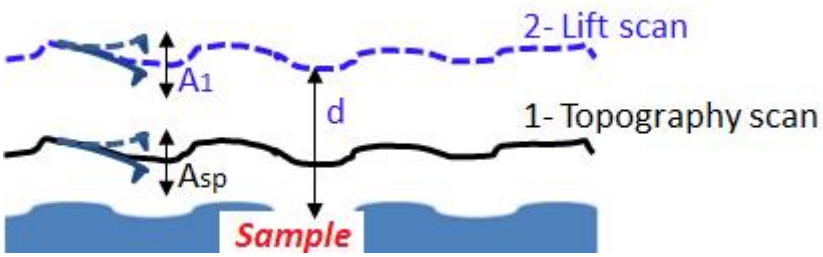

Figure 3.16: Lift mode indicating the two scan passes. The magnetic signal is obtained in the lift scan. A_1 and Asp represent the amplitude of vibration of the tip for scan 1 and 2 and d indicates the total tip sample distance.

3.2.3.3 Experimental set-up for in situ/in field measurements

To be able to perform *in situ* and *in field* measurements a small electromagnet was first used. It has the capacity to apply ~1250 Oe magnetic field at its maximum applied current and voltage (1A and 50V) (Figure 3.17a and Figure 3.17b). This limit was satisfactory for most of the samples studied in this work but there were some of the samples which needed a higher magnetic field to be saturated. For that purpose a new electromagnet was obtained from Bouhnik (Paris, France) [Bouhnik].

This was made of a steel breech containing 800 turns of copper wire of dimensions 2 x 1 mm (Figure 3.17c). The diameter of the breech was 13 cm and the assembly is 71 mm in height with a total weight of ~6 kg. The above mentioned dimensions were chosen to allow the integration of this magnet in our MFM system. With this set up, we could apply a vertical magnetic field of about 5 kOe safely at the center of the magnet (Figure 3.17d), parallel to the wire axis using short current pulses of few seconds.

The calibration of the field emanating from the electromagnets was done using Hall probe as shown in Figure 3.18. Hall probe is fixed at a distance of 2 mm from the center of the electromagnet. This distance represents the actual distance where sample will be placed during the measurements. Although the samples of dimensions 5 x 5 mm^2 can be mounted on top of the magnet but the sample, containing NWs/NTs, is usually 2 x 2 mm^2 so that it is always in the center of the magnet. The samples are pasted on a 600 µm thick Silicon substrate and placed on the center of the electromagnets to be precise about the value of the external

applied field. This should be noted that the field curves in Figure 2.18 (applied current vs generated magnetic field) have been traced using the Hall probe caliberation within 2 mm distance from the center of the electromagnet. The emanating field is not homogenous far from this range. If there are samples of exceeding dimension, care should be taken to calibearte the magnetic field accordingly.

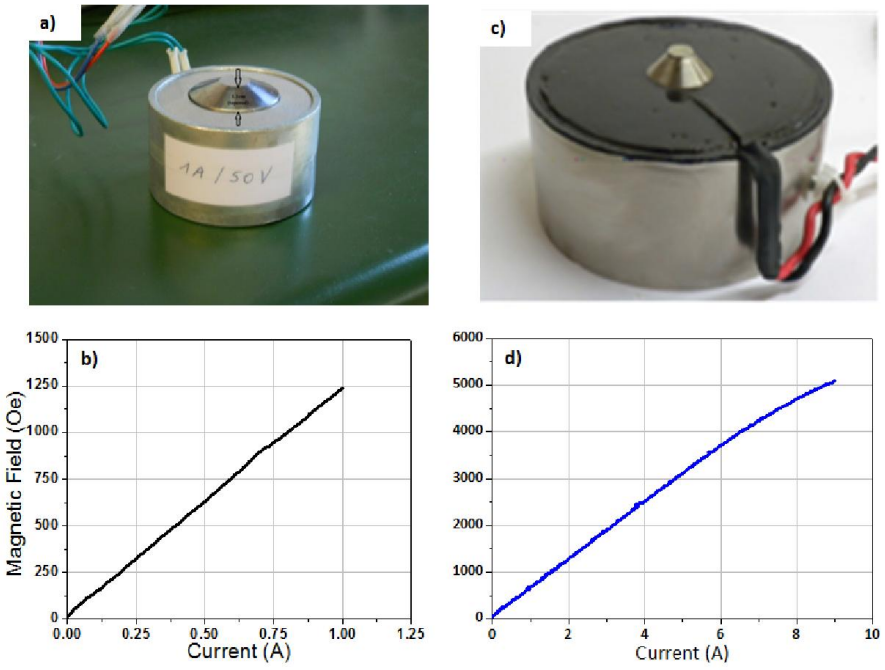

Figure 3.17: a) First electromagnet that can apply a magnetic field of 1250 Oe. b) Second electromagnet with the capability of applying 5 kOe and c) the corresponding graph of applied current and obtained magnetic field by using the second electromagnet.

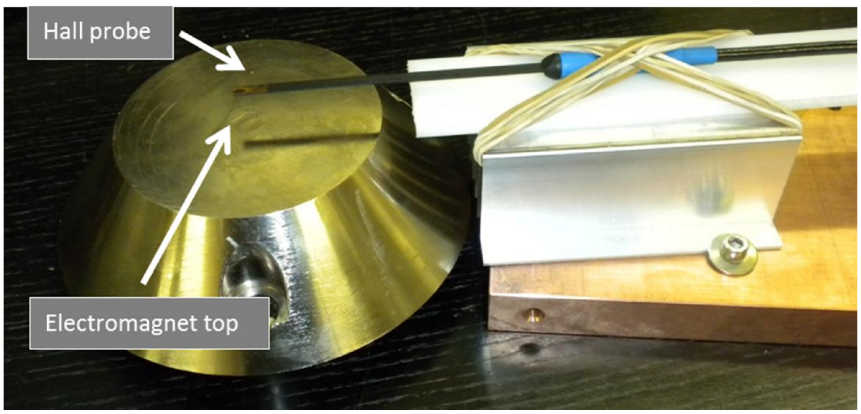

Figure 3.18: Calibrating the electromagnets using Hall probe. The probe is fixed at the centre of the electromagnet and at a height of 2 mm (same as the thickness of the sample support).

The procedure used for *in situ* or *in field* measurements was the following. Prior to the measurements the sample was saturated and the tip is magnetized as shown in the Figure 3.19. The tip was magnetized opposite to the magnetization of the sample but in the same direction as the applied field. Then, a series of magnetic fields along the magnetization of the tip but opposite to the sample's initial saturation field was applied.

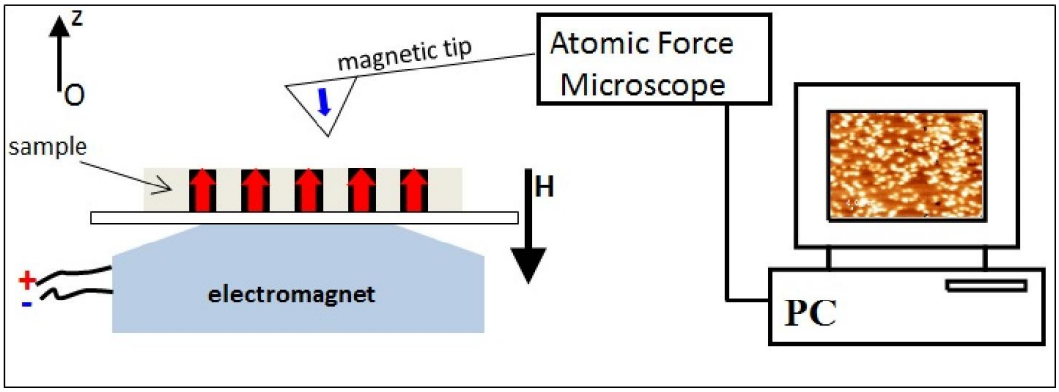

Figure 3.19: Schematic of the MFM setup.

The MFM images have been generally obtained at zero applied field (in different remanent states) after applying *in situ* external magnetic field parallel to the nanowires (Figure 3.20). This means that the applied field was switched off during the measurements. To get the *in field* images the applied field was not switched off during the image recording.

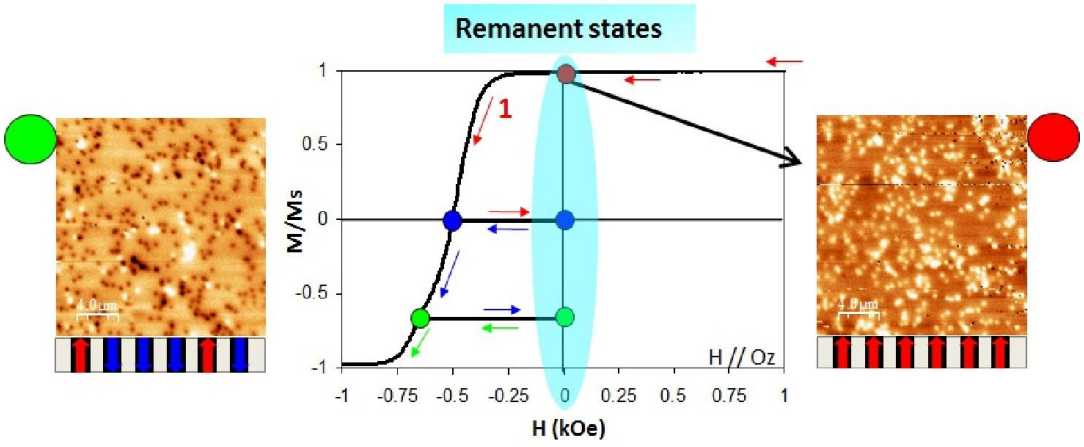

Figure 3.20: Showing the in situ MFM images recorded at remanent states when the sample is saturated (right) and when almost 75% of the wires have been switched (left)

In situ measurements in the remanent state were possible thanks to the weak dipolar interactions between nanowires in low porosity membranes. In that case, measurements done without switching off the applied field H_0 and at zero fields after applying H_0 were close to each other (this was verified for some arrays). That was the reason why low packing density samples were always characterized at remanent states. For *in field* measurements performed on medium density NWs and NTs (see chapter 5) the applied external field was not switched off.

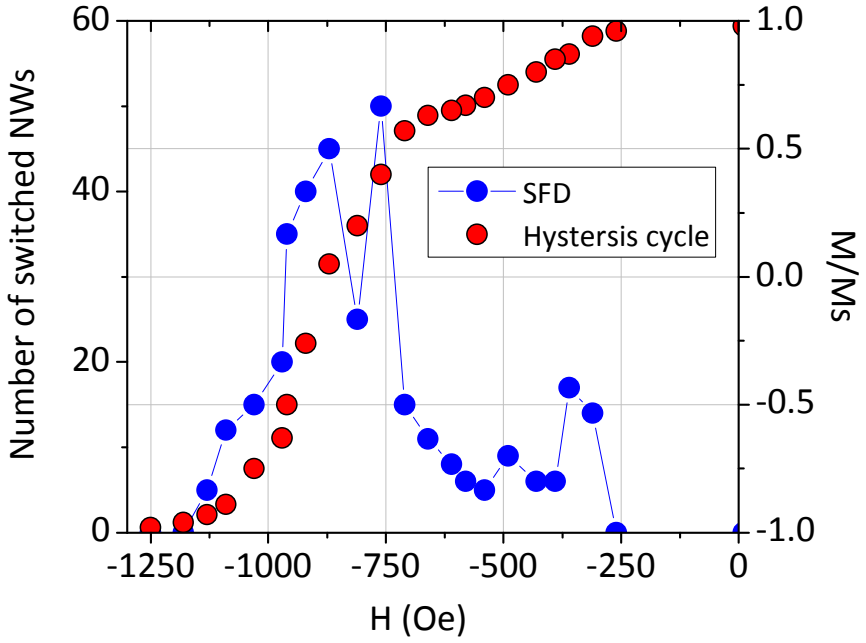

Figure 3.21: Switching field distribution (SFD) and MFM hysteresis curves.

As depicted in Figure 3.21, by counting the number of NWs which reversed their magnetization direction after each increment of applied field, MFM-magnetization curves (hysteresis curve) were obtained using

$$\frac{M^{MFM}(H)}{M_S^{MFM}} = \frac{n_{up} - n_{down}}{n_{up} + n_{down}} \qquad (3.12)$$

The MFM images were obtained, on the same scan area, by applying external magnetic field. SFD is defined as the number of switched NWs/NTs as a function of the external magnetic field as shown by red dots (Figure 3.21). SFD width (δ_{SFD}) is the field range needed to switch the first wire in a saturated array till the last wire is switched.

3.2.3.4 Selection of appropriate probes

It is an obvious fact that the cantilever-tip assembly (probe) has a critical influence on the final images obtained by MFM. The resolution and contrast of the images obtained depends largely on the tip-sample distance, tip geometry and size of its magnetic material that interact with the sample stray field. As there are long range magnetic forces involved, in order to improve the lateral resolution, it would be useful to accumulate the magnetically sensitive region to its apex so that it behaves like a small single-domain ferromagnetic particle. The magnetic moment and the coercive field of the tip should be high to detect the signal from a nano-magnetic structure such as nanowires and to keep its magnetic state stable during the scan respectively. A typical tip (MESP-HM) used for MFM measurements has been shown below (Figure 3.22).

Figure 3.22: The schematic (left) and SEM image (right) of a MESP-HM tip from Bruker®.

Before the widespread use of MFM, the practice was to fabricate the cantilevers using electrochemically etched magnetic wires of Co or Ni. Sharp tips are produced nowadays based on silicon probes coated with thin layers of magnetic materials. Figure 3.22 shows the schematic and SEM image of such a tip.

In the present work probes from different suppliers such as Bruker, Nanosensors and Assylum Research were used. The probes used (Table 3.4) had different properties, such as coercivity, magnetic moment and tip radius of curvature. They were adapted to do experiments on low-density and high density magnetic structures. In order to ensure a predominant orientation of the magnetic vector field along the tip axis, they were magnetized prior to taking measurements. During this study, samples with different packing densities and different diameters of the electrodeposited NWs and NTs have been analyzed. Therefore, as

mentioned above, several type of probes had to be used to get the desired results. For instance, to get a better contrast, a probe with high moment is appropriate but the same is not useful to resolve the high packing density wires. Similarly to do infield measurements on interacting NWs a probe with high coercivity was used so that it didn't switch its magnetization during different scans at positive and negative applied fields. The selection of the probes is not the only and final step in getting better images. There are some other criteria to be met e.g. reduced scan height (tip-sample distance, *d*) and increased driving amplitude during the lift scan pass.

Table 3-4: Characteristics of different commercial probes used during this work.

Probes	**MESP-HM** (Bruker ®)	**MESP-LM** (Bruker ®)	**LC-MFMR** (Nanosensors™)	**ASYMHC** (Assylum ®)
Moment (emu)	~ $3x10^{-13}$	~ $0.3x10^{-13}$	~ $0.75x10^{-13}$	~ $3x10^{-14}$
Coercivity (Oe)	400	<400	0.75	>5000
Nominal tip Radius (nm)	90	~30	~30	~50

3.2.3.4.1 Influence of the lift scan height

MESP-HM (Table 3.4) was the appropriate probe for imaging low packing density and low moment samples [MESP-HM]. The surface of the PC-template compared with the alumina is not very smooth imposing relatively large lift height. Nevertheless by decreasing lift scan height contrast can be drastically increased as indicated in Figure 3.23. Therefore a compromise had to be found to get the best contrast without striking the tip with the sample surface. The best lift height is strongly dependent upon the roughness of the sample surface and for this particular sample was 60 nm.

Although high moment probes were suitable for low *P* samples they wouldn't distinguish the stray field emanating from individual NWs in high packing density samples. This was due to fact that the tip's stray field was large because of its larger nominal diameter at the apex and due to high magnetic moment. This is

illustrated in Figure 3.24 that present images of high porosity samples acquired with high moment probes. To summarize reducing the scan height of high moment probes improves the resolution for low P samples but does not allow distinguishing NWs in high P samples.

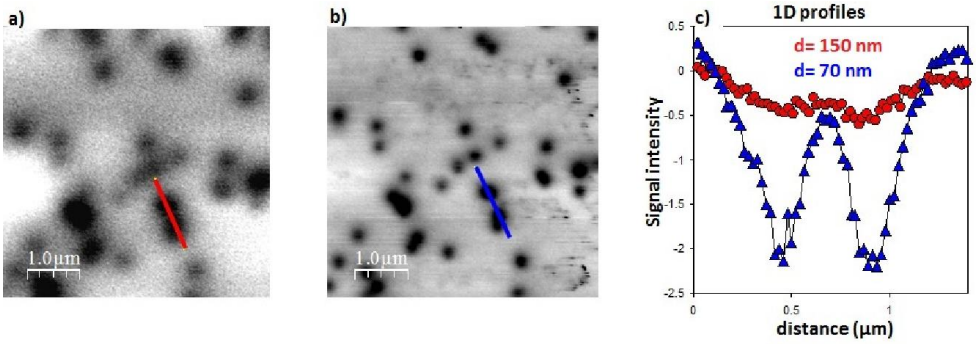

Figure 3.23: The magnetic contrast is strongly increased from a) 150 nm tip-sample distance to b) 70 nm and c) 1D profiles of the signals obtained from CoFe NWs array of 70 nm.

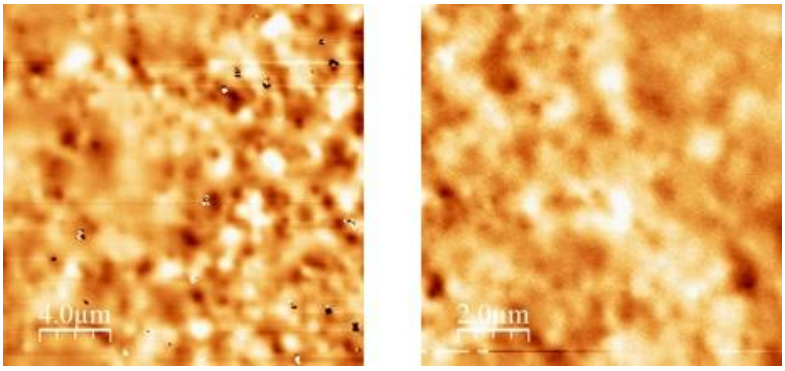

Figure 3.24: Resolution limit of the MESP-HM at its optimal parameters for Ni NWs of P~10% and diameter 100 nm (left) and for NiFe NWs of P~5% and diameter 40 nm (right)

For high *P* samples other probes (Table 3.4) have been used and the influence of changing the tip-sample distance was systematically studied (Figure 3.25). The first left images in all the rows present the topography. The second MFM image at tip sample distance $d \approx 150$ nm and third MFM image at $d \approx 100$ nm. The images have been taken with a fixed amplitude of the tip during second pass $A_1 = A_0$. Here, A_0 represents the free vibration amplitude. Quality and resolution of the images improves when the distance d is reduced from 150 nm to 100 nm. The top row represents the scans from ASYMHC, the second row from PPP-LC-MFMR and the last row from MESP-LM probes [ASYMFMHC, PPP-LC-MFMR, MESP-LM]. As all the

MFM images show the black contrast, it indicates that the NWs are magnetized in the same direction as tips.

The resolution strongly depends upon the choice of the probe. The difference of changing the *d* while using ASYMFM high coercivity probes is not very evident so these can be useful for the samples where the surface is rough. The lateral resolution is poor which limits their use for medium and high packing density NWs. The PPP-LC-MFMR probes have sharper tip radius. They can better distinguish the dense magnetic particles. MESP-LM low moment probes present the best resolution. At 150 nm the wires cannot be seen individually because of the low interaction. On the contrary, at 100 nm the image presents an excellent resolution.

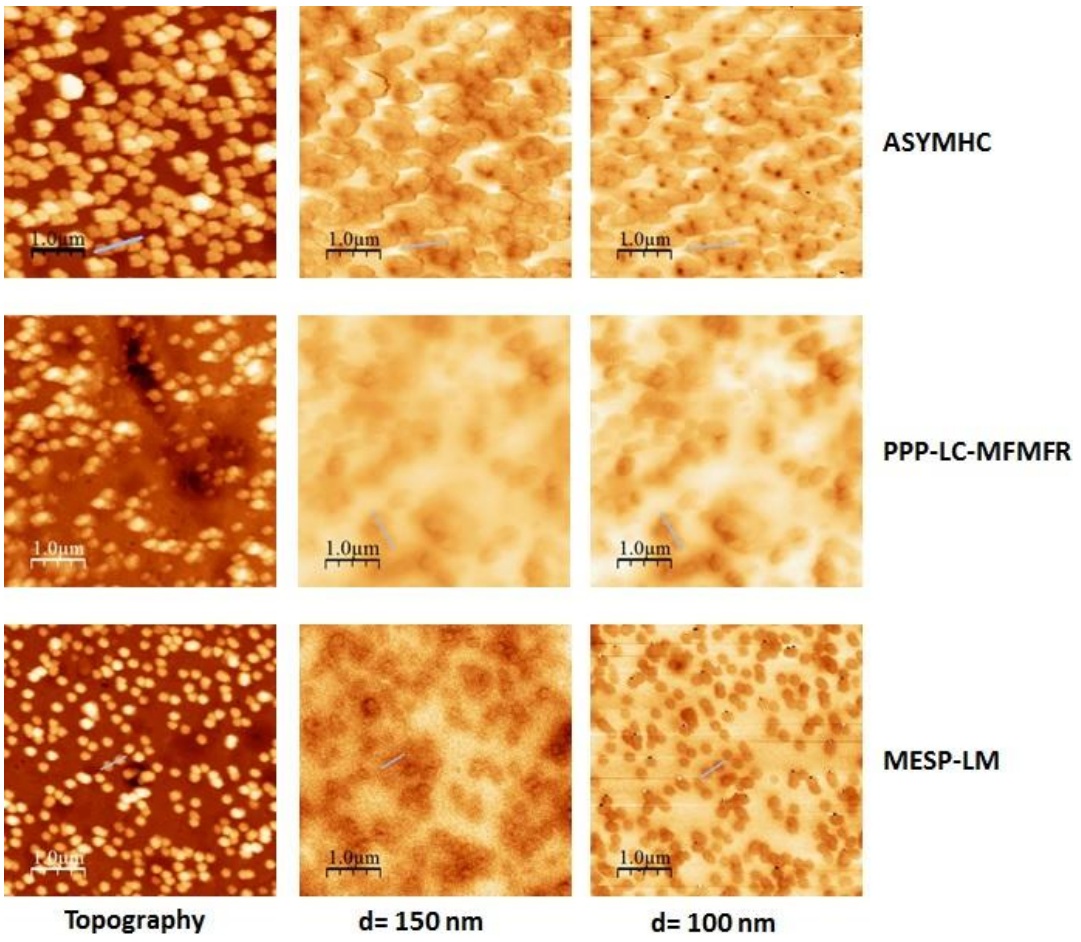

Figure 3.25: The Influence of the probe and the tip-sample distance on resolution of the MFM images from Ni NWs of diameter 100 nm and P~10%. The top row represents the scans from ASYMHC, the second row from PPP-LC-MFMR and the last row from MESP-LM probes. The height scale *z* for topography images ranges from - 33 to 145 nm.

The influence of the lift scan height has been measured systematically in a master thesis and results have been presented in Figure 3.26 [Coulon 2014]. It has been shown that by decreasing the tip sample distance the resensitivity can be drastically improved for all probes and especially for MESP-LM. The main reason is the lwo moment of these tips which cannot detect the signals from NWs at larger distances.

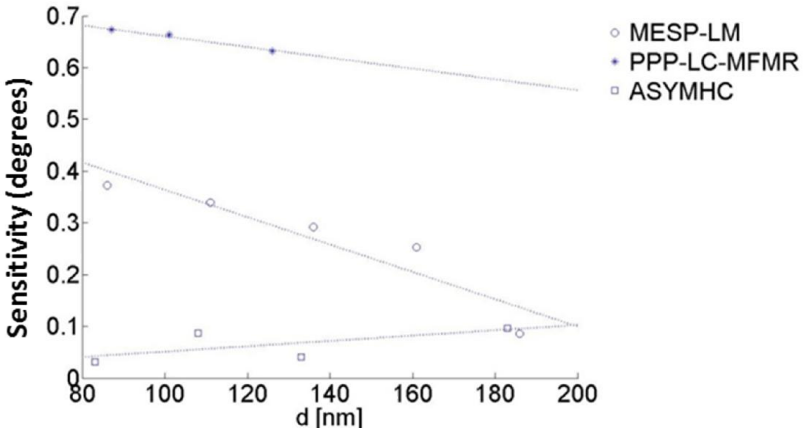

Figure 3.26: Comparison of improvement of resolution of MFM images with respect to the lift scan height for various magnetic tips.

3.2.3.4.2 Influence of the vibration amplitude

Larger vibration amplitudes during the second pass are expected to increase the signal-to-noise ratio (SNR) and hence to improve the quality to the magnetic images. However, the tip scan height is strongly limited by the vibration amplitude during the second pass, A_1. A_1 cannot be increased or the distance of the tip cannot be reduced if the tip starts tapping the sample surface, especially when using rough surfaces. An example of such parasitic signals is presented in Figure 3.27. Therefore, a compromise has to be found between both parameter in order to obtain both high resolution and acceptable SNR. Generally, when the distance is optimized, A_1 can be increased slowly until parasitic signals (streaks) are observed on the phase image due to the tip tapping the surface. Once this limit is reached, the vibration amplitude is slightly reduced until the parasitic signals disappear.

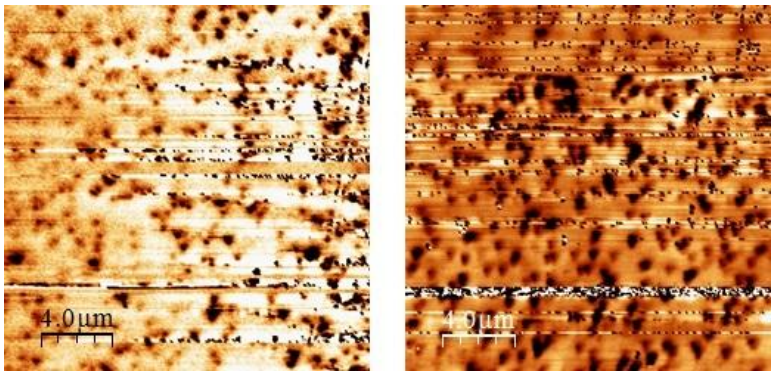

Figure 3.27: Effect of too large vibration amplitude or too small lift high with parasitic signals appearing on the phase image during the second pass (ASYMHC tip).

The influence of the vibration amplitude on the MFM resolution for various tips is in Figure 3.28. These images have been recorded on the same areas as of Figure 3.25.

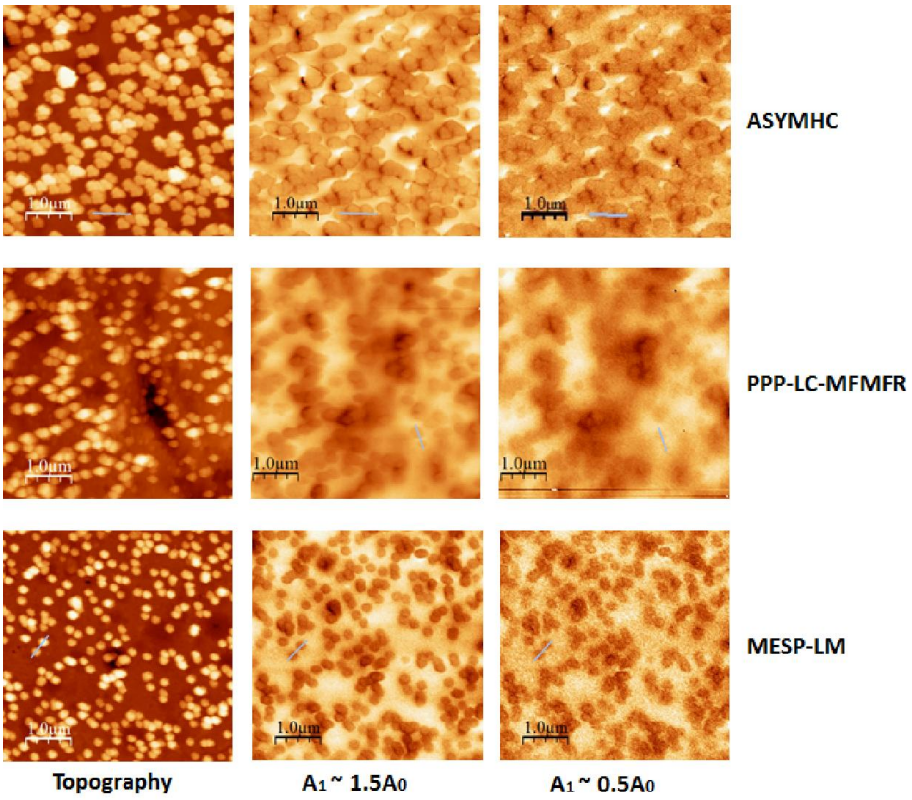

Figure 3.28: Influence of the vibration amplitude on the MFM image quality from Ni NWs of diameter 100 nm and P~10%. The top row represents the scans from ASYMHC, the second row from PPP-LC-MFMR and the last row from MESP-LM probes. The height scale *z* for topography images ranges from - 33 to 145 nm.

The tip-sample distance was kept constant while the value of A_1 was increased or decreased. This modification was done with respect to A_0. As expected, the SNR

decreases when the amplitude decreases for all the probes used. If the value of A_1 is too small the image details are not be distinguishable. The best images were obtained for larger vibration amplitude, due to the improvement of the signal-to-noise ratio. Apparently, the quality of the images obtained using the ASYMHC probes is less sensitive to the variation of the vibration amplitude.

Similar to life scan height, measuring the influence of the drive amplitude was objective of a master thesis [Coulon 2014]. It has been measured systematically and results have been presented in Figure 3.29. It has been shown that by increasing the A_1 by various small steps SNR can be drastically improved except for ASYMHC.

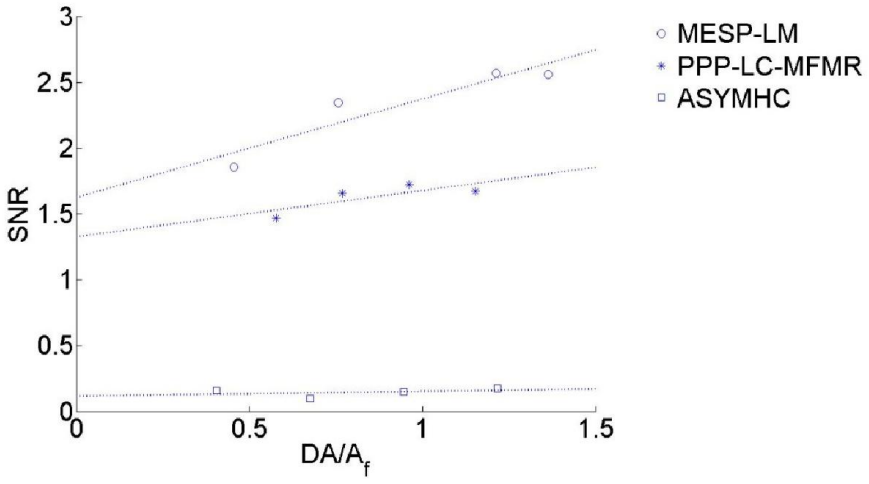

Figure 3.29: Comparison of improvement of resolution of MFM images with respect to the drive amplitude for various magnetic tips.

3.2.3.4.3 Tip aging and manufacturing faults

The quality of the images is also a matter of the tip aging, tip damage or manufacturing flaws. The images obtained using two different probes from the same box (same manufacturer and probe type), exhibit quite different features sometimes, which could be attributed to manufacturing defects. The magnetic coating of the used tips may be oxidized due to its exposure to atmosphere that result in blurred images as the one shown on left in Figure 3.30. The tip coating may be damaged during manufacturing. Tapping during the MFM scans on the

surface artifacts of PC membrane may damage the tip magnetic coating. This could result in very strange magnetic contrasts, see Figure 3.31. This particular artifact appeared only for MESP-HM tips. Replacing the tip by another tip from the same supplier gave the nice results as shown in chapter 4.

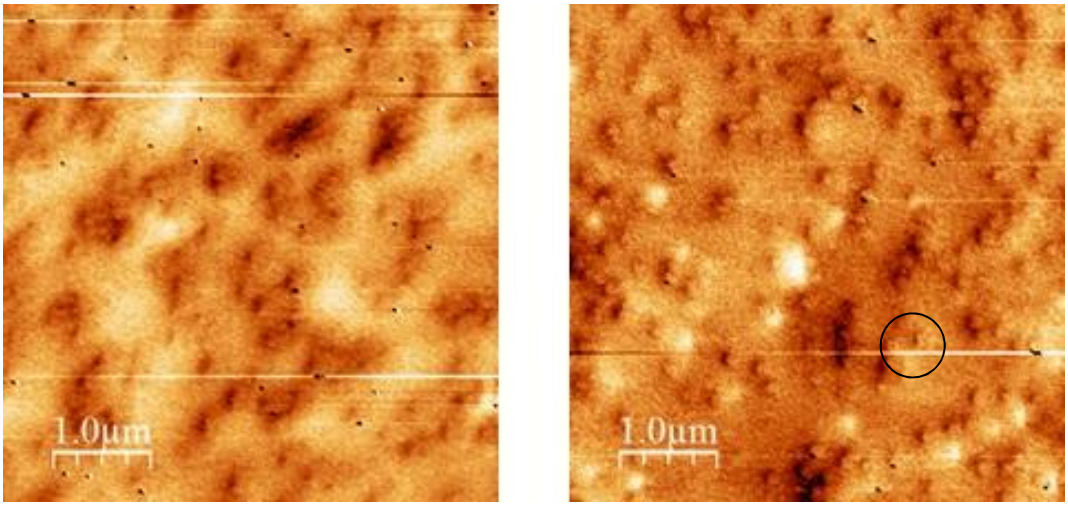

Figure 3.30: Effect of tip aging or damaged tip on the quality of the MFM images (left). The image from the tip, MESP-LM, newly exposed to atmosphere and to the sample (right).

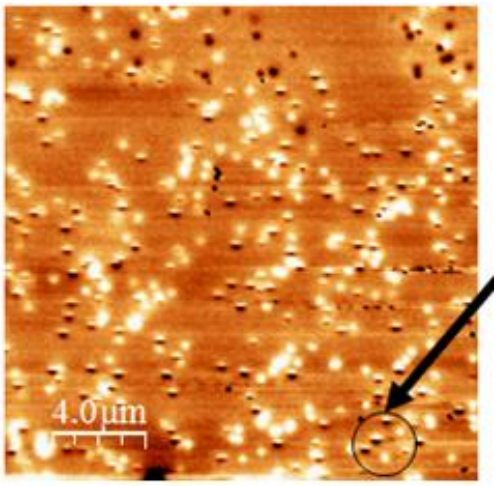

Figure 3.31: Effect of MESP-HM tip artifacts on the quality of the MFM images (array of CoFe NWs of 100nm diameter).

To sum up this section, we have an idea now about the suitability of the probes for various studies samples in this work. Table 3-5 indicates the probes used and the optimal working conditions for various studied samples.

Table 3-5: Optimized probes and conditions for various studied samples.

Packing density (%)	Probe used	Scan height	Amplitude
< 1	MESP-HM	~ 60 nm	~ 1.2 A_0
~ 4 , ~ 6, ~10	ASYMFM-HC	~ 60 nm	~ 1.2 A_0
~ 12	MESP-LM	~100 nm	~1.5 A_0

3.2.4 Numerical Calculations-FEMM:

The calculation method to solve electromagnetic problem on two dimensional planar and axisymmetric domains was finite element method magnetic FEMM [Meeker 2014]. Although the differential equations of interest appear relatively compact, it is typically very difficult to get closed-form solutions for all but the simplest geometries. This is where finite element analysis comes in. The idea of finite elements is to break the problem down into a large number of regions, each with a simple geometry e.g. triangles. The advantage of breaking the domain down into a number of small elements is that the problem becomes transformed from a small but difficult to solve problem into a big but relatively easy to solve problem.

The preprocessor was used for drawing the problems geometry, defining materials, and defining boundary conditions. A new instance of the preprocessor can be created by generating the “new file” off of the main menu of the software and then selecting “Magnetics Problem” from the list of problem types which then appears.

- Drawing a valid geometry (in our case NWs) usually consists of four tasks:
- Sketching the endpoints of the lines and arc segments that make up a drawing.
- Connecting the endpoints with either line segments or arc segments
- Defining material properties and mesh sizing
- Specifying boundary conditions on the outer edges of the geometry.

In this work, this simulation tool has been employed to get an insight on how the magnetic NWs and NTs behave independently and in the presence of neighboring wires. The magnetic stray field from a single NW was calculated as shown in Figure 3.32.

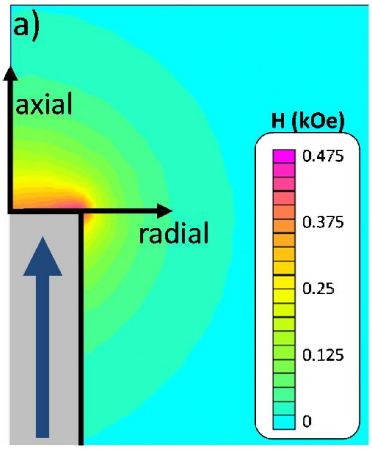

Figure 3.32: Dipolar field, calculated using FEMM, emerging from a NW of diameter *D* = 100 nm.

Chapter 4

Comparison of SFD in low and high packing density $Ni_{80}Fe_{20}$ and $Co_{55}Fe_{45}$ NWs arrays

4.1 Introduction

In recent years, there have been a considerable number of studies regarding the formation of high density arrays of single domain magnetic NWs embedded in nanoporous alumina templates by electro deposition [Nielsch 2001, Fodor 2003, Sorop 2004, Piraux 2005, Vazquez 2005, Carignan 2007, Medina 2010]. Although the switching field distribution (SFD) of the NWs arrays can be obtained from a DC demagnetization remanence curve averaged over a large nanowire array, magnetic force microscopy (MFM) has been found to be an interesting approach to probe locally the magnetization reversal process and to obtain local hysteresis loops.

The SFD has two components that should be addressed separately [Nieslch 2002, Hellwig 2007, Khan 2002]: an intrinsic part and an extrinsic part i.e. dipolar contribution. Intrinsic broadening of the SFD may arise from local variations of the nanowire magnetic properties and disparity in nanowire sizes and edge effects. The dipolar interaction arises from the magnetostatic interaction of a nanowire with its neighbors. In the latter case, the reversal field of a nanowire depends on the magnetic state of its neighbors. Both effects manifest themselves as a distribution of the switching fields associated to the magnetization reversal process of nanowires. From previous studies performed on dense arrays of single domain

nanowires embedded in alumina templates, it appears that the δ_{SFD} is quite large, up to 5-8 kOe [Fodor 2003, Nielsch 2002, Wang 2008, Dobrynin 2009]. It results mainly from the large dipolar magnetic interaction that dominates the behavior of hysteresis loops. Discrimination between intrinsic and dipolar contributions was not straightforward and required dipole-dipole interaction models to estimate the intrinsic SFD [Wang 2008, Yuan 2008].

In this work, we present a fundamental MFM study to evaluate the intrinsic SFD in arrays of bistable $Ni_{80}Fe_{20}$ and $Co_{55}Fe_{45}$ NW deposited in low porosity polycarbonate (PC) membranes with controlled diameters in the range 40-100 nm. All NW can be considered as infinite long cylinders. It is shown that the intrinsic SFD width, extracted directly from the MFM measurements without involving complicated calculations, is considerably narrow. This indicates that the broader SFDs in dense arrays of NWs was certainly the result of dipolar interactions. In addition, the non-uniformity in wire diameter causes an increase of the intrinsic δ_{SFD} as the diameter is reduced.

4.2 Results and discussion

Fabrication of $Ni_{80}Fe_{20}$ and $Co_{55}Fe_{45}$ NWs has been presented in section 3.1.1. The chemical solutions used for electrodeposition to produce NWs arrays of various diameters and packing density < 1% are shown in table 3.1. Section 3.1.2 presents the MFM sample preparation whereas section 3.1.3 describes the methods to calculate packing density of the samples, *P,* and the interwire distance, I_D, of the NWs arrays. The I_D between nanowires was found to be always larger than 600 nm.

MFM probes, Bruker MESP-HM, with a force constant around 2.8 $N.m^{-1}$ and a resonance frequency of about 75 kHz were used for this study. The analyses were realised in amplitude-modulation (AM-AFM) using a double pass procedure. The setup of the instrument was modified with a custom-built electromagnet for performing *in situ* MFM experiments allowing the analysis of the same spots of the

samples after applying various magnetic fields parallel to the NW direction. Details on the MFM-setup can be found in section 3.2.3.

The different MFM-images presented in this work were obtained at zero fields, in the remanent states, after applying increasing reverse magnetic fields along the NW's axis. In addition to the MFM experiments, magnetization curves were obtained using an alternating gradient field magnetometer (AGFM). The FEMM package (section 3.7) has been used in order to estimate the dipolar field created by an isolated and uniformly magnetized NW. Table 4.1 presents the packing density, *P,* and the mean interwire distances, I_D, of the studied NWs samples along with the NWs diameter *D*. These values were obtained from the local MFM scans on samples of $P < 1\%$.

Figure 4.1a presents the dipolar field created by a uniformly magnetized and isolated NW ($L = 4$ µm, $D = 100$ nm) using the $Ni_{80}Fe_{20}$ saturation magnetization value: $M_S = 850$ emu.cm^{-3}. It illustrates that for $I_D > 300$ nm the dipolar interaction between NW can be neglected. As a consequence, the magnetic state in the remanent state and under an applied magnetic field should be the same. This is demonstrated by the MFM images of a $Co_{55}Fe_{45}$ nanowire array ($D = 50$ nm) in a positive 600 Oe field (Figure 4.1(b)) and as the field was lowered to zero (Figure 4.1(c)).

Table 4-1: Local packing densities and the mean inter-wire distances for various samples measured from MFM scan.

D **(nm)**	**Measured *P*** **(%)**	**Inter-wire distance I_D** **(nm)**
40	0.04	~1200
50	0.15	~1000
70	0.19	~1000
100	0.25	~1200

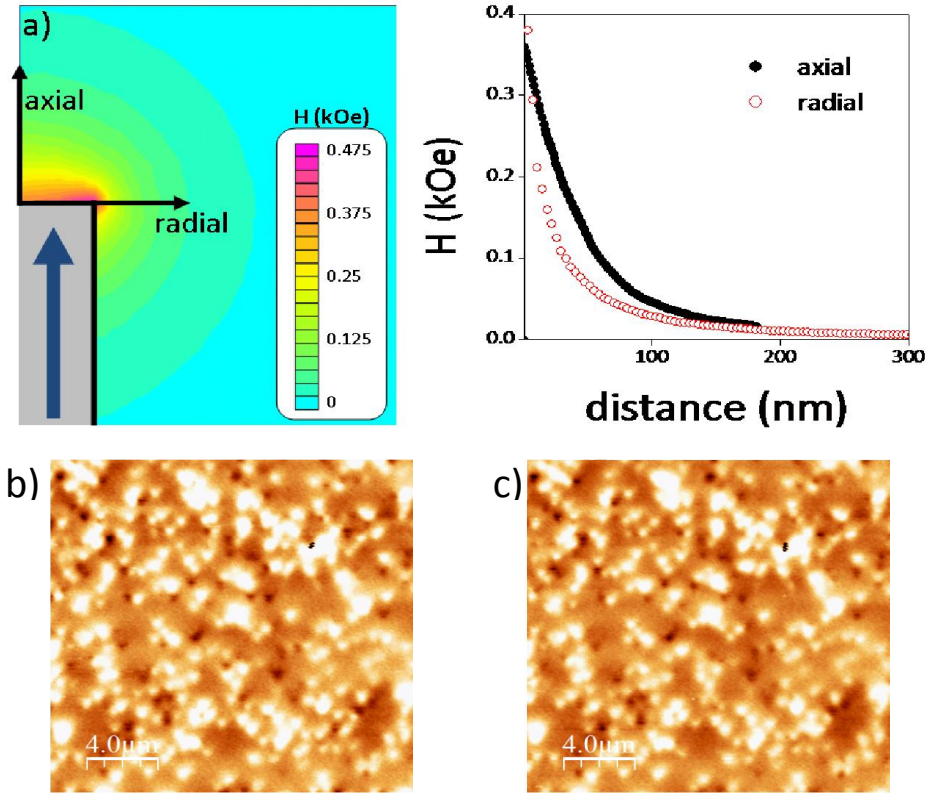

Figure 4.1: (a) Simulation of the radial and axial components of the stray field from an isolated nanowire ends using FEMM and considering a 4 µm-long NW of diameter *D* = 100 nm uniformly magnetized. The magnetic parameters used in the simulation correspond to the $Ni_{80}Fe_{20}$ composition (M_S = 850 emu.cm^{-3}). MFM images of the $Co_{55}Fe_{45}$ nanowire array (*D* = 50 nm) in (b) a positive 0.6 kOe field and (c) lowering the field to zero to verify the bistable behavior of the nanowire array.

4.2.1 MFM scans on $Ni_{80}Fe_{20}$ and $Co_{55}Fe_{45}$ arrays

Figure 4.2 and Figure 4.3 present a series of MFM images of the 50 nm and 100 nm diameter $Ni_{80}Fe_{20}$ NWs array scanned at different remanent states, respectively. Before inserting the array inside the microscope, it was saturated under a magnetic field of *H* = +2 kOe along the NW axis (+*Oz*) while the magnetic tip of the microscope was saturated in the opposite direction (-*Oz*). From the first images (top left), which corresponds to the one just after saturating the system, we observed that the NWs were still oriented in the same direction (as seen from the white spots). Then, a series of magnetic fields opposite to the sample initial saturation field were applied. The successive switching of the 50 nm NWs started around - 500 Oe till the application of - 950 Oe where all the NWs had been

switched black. The start and end of the switching in the 100 nm NWs array was -180 Oe and - 500 Oe respectively.

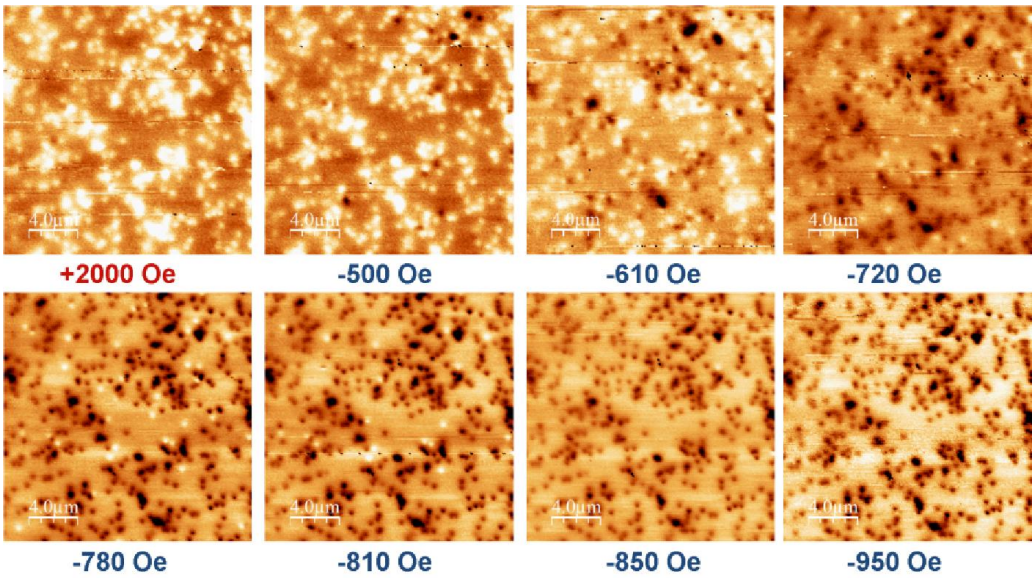

Figure 4.2: Array of $Ni_{80}Fe_{20}$ NWs with *D* = 50 nm: series of MFM images on scan areas of 20 x 20 μm^2 (taken at zero applied field: see text) indicating the progress of magnetization reversal after saturation in a positive field H = +2 kOe) and for different negative applied fields.

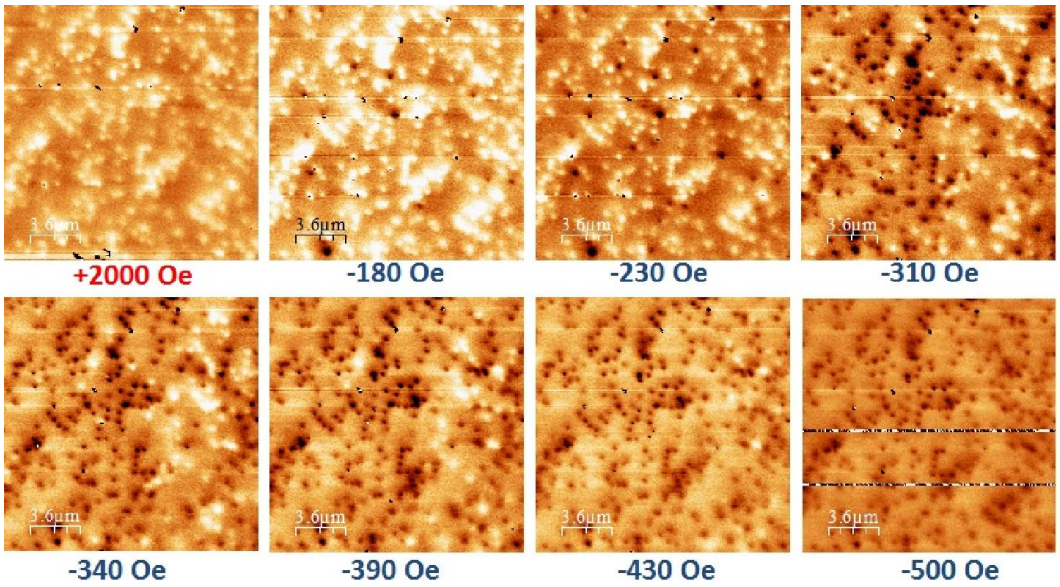

Figure 4.3: Array of $Ni_{80}Fe_{20}$ NWs with *D* = 100 nm: series of MFM images on san area of 15 x 15μm^2 (taken at zero applied field: see text) indicating the progress of magnetization reversal after saturation in a positive field H = +2 kOe and for different negative applied fields.

Figure 4.4a-b present typical MFM images obtained for the arrays of $Co_{55}Fe_{45}$ NWs (*D* = 70 nm) and $Ni_{80}Fe_{20}$ NWs (*D* = 70 nm). The successive switching of the NWs

started after the application of around - 360 Oe and - 310 Oe until the application of around - 1200 Oe and - 585 Oe for $Co_{55}Fe_{45}$ and $Ni_{80}Fe_{20}$ NWs, respectively. The spot sizes (black or white) are larger than the nominal diameters of the wires because MFM measures the dispersive stray field emanating from the wires and not the exact wire dimensions.

These images suggest the bistable behavior of the nanowires. The MFM investigations show the magnetization only at the top of the NW and the presence of only two magnetization states indicates that they are bistable. Indeed, the bright and the dark contrasts of the NW are the result of their magnetization antiparallel or parallel to the magnetization of the probe, respectively, as explained above. The coercivity of the probe is 400 Oe whereas its magnetic moment is ~ 3 x 10^{-13} emu. The measurements are done at remanent state so stray field of the tip is not influencing the magnetization reversal of the NWs. The method to calculate tip stray field will be presented in chapter 6.

From the MFM images, only two remanent states are observed for each NW suggesting single domain NWs with “up” (along *+Oz*) and “down” (along *-Oz*) magnetisation directions. Consequently, the local hysteresis curve was calculated by counting the number of NW with “up states” and “down states” and by using equation 3.12.

Figure 4.5 shows the MFM-magnetization curves obtained from the different $Ni_{80}Fe_{20}$ and $Co_{55}Fe_{45}$ NWs arrays (solid dots). In addition, bulk magnetization curves have been obtained using AGFM and compared to the MFM-magnetization curves (continuous lines). The results from MFM and AGFM are in good agreement. For $Co_{55}Fe_{45}$ NWs arrays of diameter 40 nm, we were not able to measure the complete MFM hysteresis curves due to limitation of the applied external field. Further, for this sample AGFM measurements did not provide us satisfactory curves, to be presented here for comparison. The small deviations that appear between these two measurements can be attributed to the fact that a limited number of NWs is

probed using MFM (local study) while the whole set of NWs is probed using magnetometry measurements.

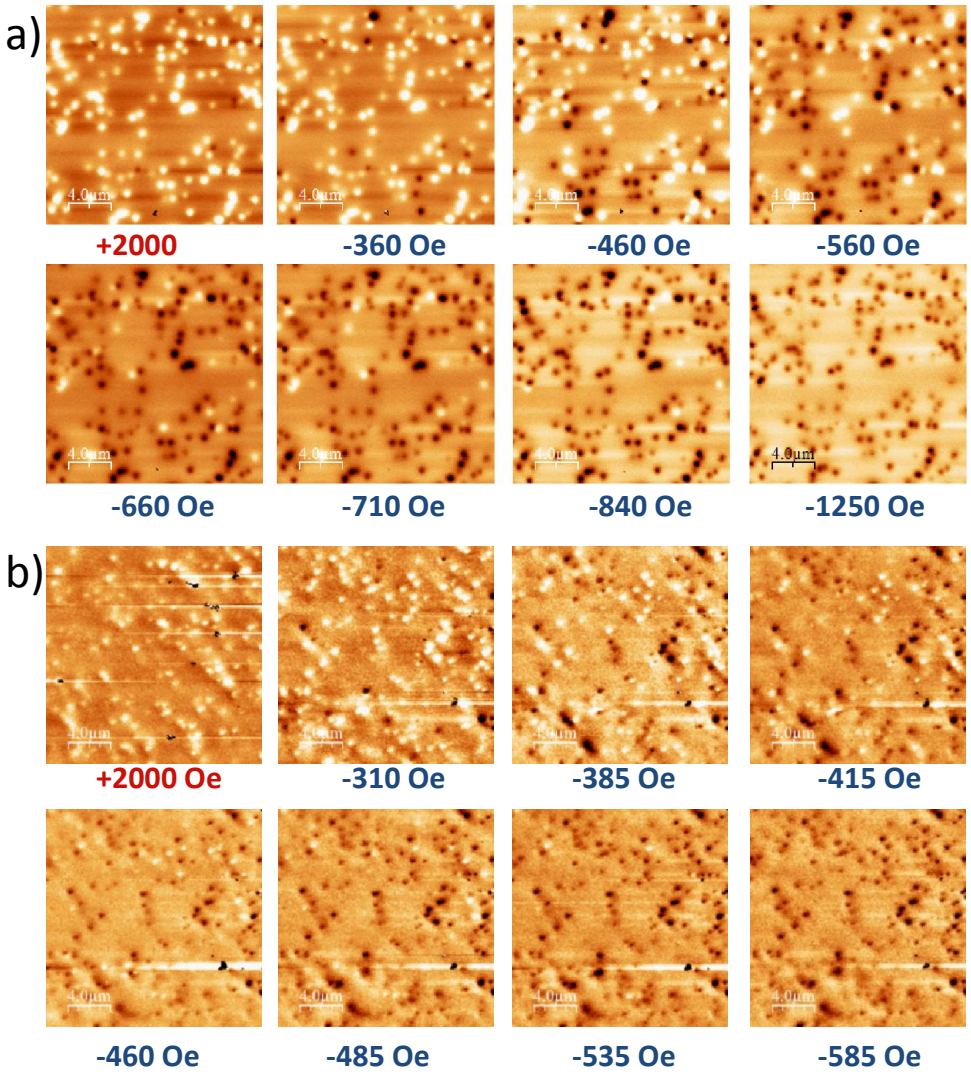

Figure 4.4: MFM images of the $Co_{55}Fe_{45}$ nanowire array of D = 70 nm at zero field after saturation in a positive 2 kOe field and then in a variety of non-saturated remnant states obtained by changing each time the magnetic state of the nanowire array from saturation to a given negative field and then to remanence by reducing the field to zero. All the images were scanned in the same area; (b) same as in (a) for the $Ni_{80}Fe_{20}$ nanowire array D = 70 nm.

Actually, the measurements performed by a magnetometer are sensitive to the entire volume of the sample whereas the MFM measurements are not sensitive to it since it is a surface and local imaging technique. This difference is illustrated in

Figure 4.6. The switching of the half volume of a NW is not measured as H_c by AGFM which is the case for MFM. From the good agreement between both kinds of measurements, it can be assumed that the scanned area ($20 \times 20\ \mu m^2$) is large enough to ensure that the effect of NW volumes distribution is taken into account. In addition, MFM allows mapping the local magnetization curves for the NW arrays with very low packing density where the volume magnetic moment is too weak to be measured by bulk magnetometry.

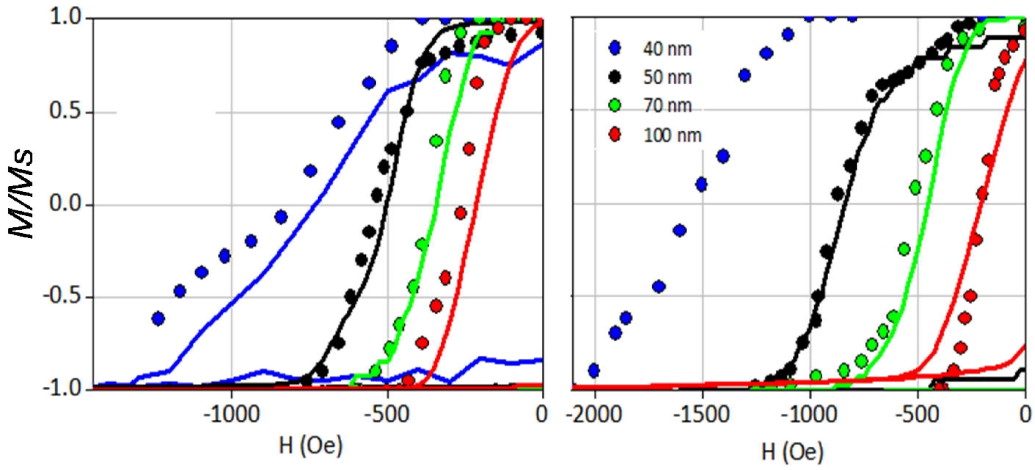

Figure 4.5: MFM-magnetization curves (solid dots) and bulk magnetization curves (continuous lines) for the different arrays of $Ni_{80}Fe_{20}$ NWs (left) and $Co_{55}Fe_{45}$ (right)

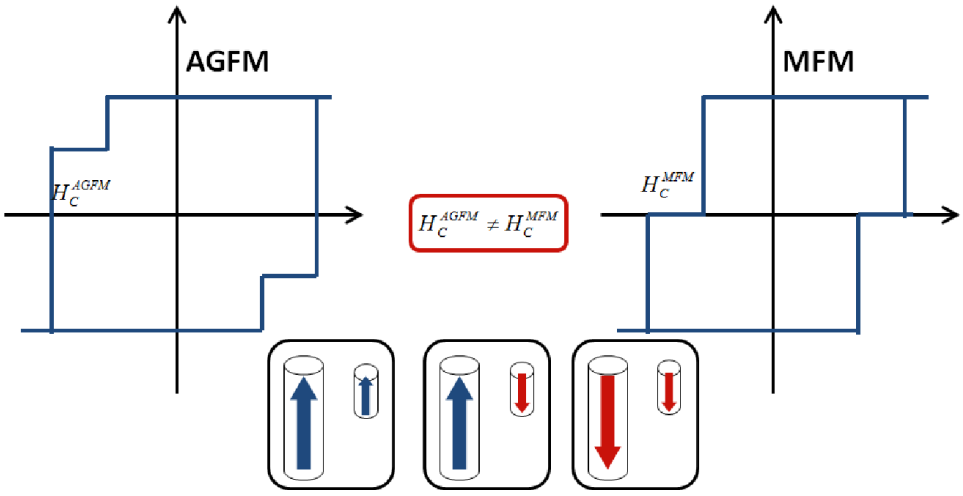

Figure 4.6: Schematic curves of switching of two wires detected by AGFM and MFM. AGFM is sensitive to the whole volume whereas MFM is sensitive to the signal emanating from top of magnetic NWs so showing two coercivities.

From the images presented in Figure 4.2 to Figure 4.4, we observe that the magnetization reversal of the NW is nearly random. This supports the assumption of weak dipolar interactions. Indeed, in AAO arrays of NW [Nielsch 2001, Navas 2005] exhibiting strong dipolar interactions, the switching of one NW is strongly influenced by the magnetization state of its neighbors.

In addition, the demagnetized state of AAO NW arrays presents a labyrinth domain pattern, as expected for a hexagonal array to maintain neighboring bits with antiparallel magnetization and to minimize the inter NW dipolar field energy [Nielsch 2001]. The demagnetized state of the present arrays corresponds roughly 50% of black (resp. white) spots, randomly distributed (Figure 4.7) which is consistent with an array presenting negligible dipolar interactions.

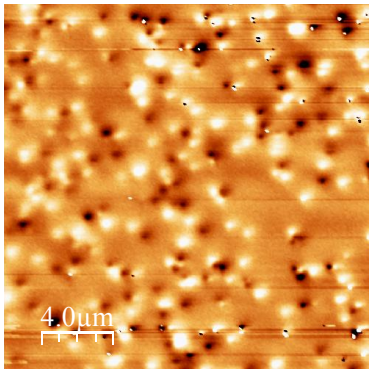

Figure 4.7: MFM image of demagnetized state of 100 nm $Co_{55}Fe_{45}$ NWs arrays.

4.2.2 Dependence of coercive field on diameter

The coercive field measured by MFM is reported in Figure 4.8a as a function of NW diameter. It increases with decreasing *D* for the two sets of NW arrays. This variation can be well fitted using a D^{-2} law (solid lines in Figure 4.8a). Magnetization reversal analytical models of an infinite cylinder have been used to qualitatively explain this dependence [Ferré 1997]. The dependence of H_c on the diameter of the nanowires in the curling model is given by $H_C = 6.78 A (M_S R^2)^{-1}$, where *A* is the exchange stiffness and *R* the radius of the NW. It is in qualitative agreement with the experimental observations. However, the values found with this model are approximately two times larger than the experimental ones. Such difference has

already been found in previous studies where the *D*-dependence of the coercive field of non-interacting Ni NWs embedded in PC membranes has been experimentally determined and compared to micromagnetic simulations and analytical models [Ott 2009]. Shape deviations from the ideal cylinder [Chen 2012b] like structural defects at the extremity of the NW can play the role of nucleation sites for the magnetization reversal and may be the origin of these differences. However, from the *D* dependence of the coercive field, it can be concluded that in these arrays of NW, the magnetization reversal follows the curling mode and not the coherent mode.

4.2.3 SFD in dense arrays of NWs

The SFD is linked with the number of switched NWs after each increment of the applied magnetic field. Extraction of SFD of NWs from MFM has been reported in section 3.2.3. The SFD width (δ_{SFD}) which corresponds to the field range between the magnetization reversal of the first NW and that of the last one is also found to be *D*-dependent (see Figure 4.8b). The δ_{SFD} obtained from densely packed NW arrays are also reported in Figure 4.8b for comparison [Wang 2008, Hellwig 2007, Nielsch 2001, Salem 2010, Fodor 2003, Dobrynin 2009, Aravamudhan 2009, Liu 2005, Xu 2008, Cho 2010, Kou 2009.,Shomski 2000]. These values are at least 3 times larger than the ones obtained in this study .For instance, low density NiFe NWs array of 100 nm has δ_{SFD} of only 300 Oe whereas it is more than 4000 Oe for the high density NW arrays (see extreme right of Figure 4.8b).

In the dense arrays, the dipolar interactions are strong and lead to a broadening of δ_{SFD} [Nielsch 2001], whereas, in the present study δ_{SFD} is essentially due to intrinsic effects and no complex calculation is required to discriminate between the intrinsic and dipolar contributions to the switching field distribution. Wang et al. [Wang 2008] reported the intrinsic SFD in an array of Co NW (D = 30 nm) embedded in AAO membranes by evaluating and subtracting the total dipolar field present in this array. Even after subtracting the effect of this dipolar field, an intrinsic SFD width of about 4 kOe was estimated (i.e. about one order of

magnitude larger than in the present study) which confirms the complexity of such an analysis. The deviation of δ_{SFD} from an ideal Dirac function may be due to parameters such as the distributions of diameter and length, the non-uniformity of the shape, random wire distribution, inhomogeneities in the microstructure and chemical composition of the NW.

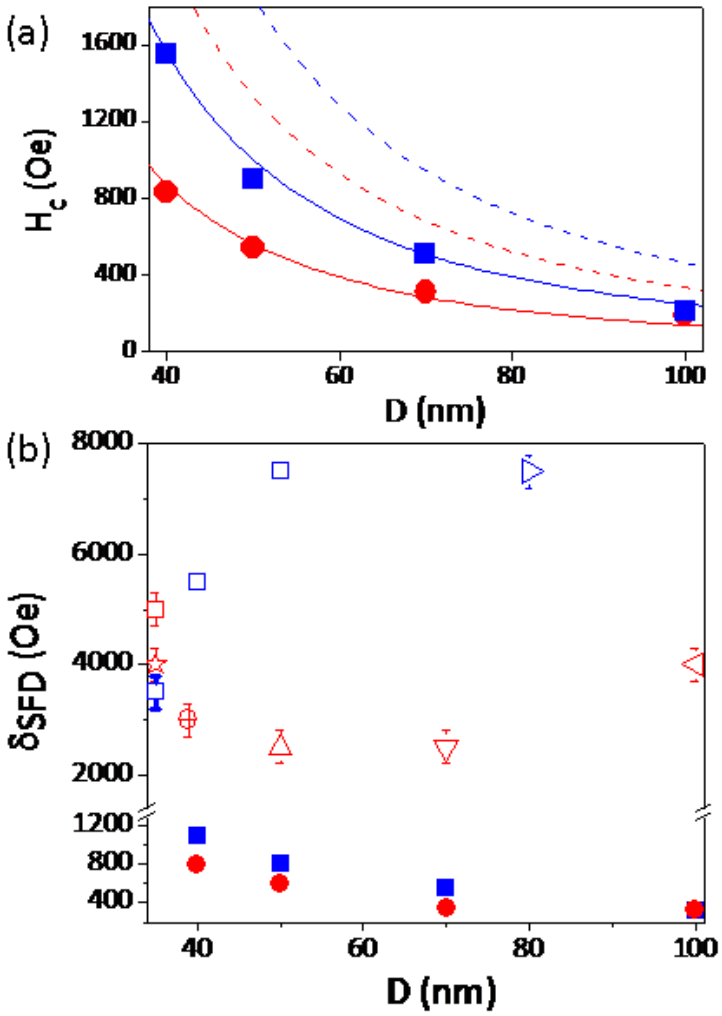

Figure 4.8: (a) Variation of the average coercive field as a function of diameter for the $Ni_{80}Fe_{20}$ (●) and $Co_{55}Fe_{45}$ (■) NW arrays; the dashed lines showing a D^{-2} variation are calculated by using the analytical formula of H_C in the curling model [Aharoni1958, Skomski2000]; the continuous lines are the fits obtained by using a D^{-2} law ,(b) Variation of the switching field distribution width of $Ni_{80}Fe_{20}$ and $Co_{55}Fe_{45}$ NW arrays (filled circles and squares, respectively) as a function of D and comparison with previous results obtained on NW arrays embedded in AAO templates; blue open symbols represent $Co_{55}Fe_{45}$ NWs whereas the red open symbols represent $Ni_{80}Fe_{20}$ NW: ⊕ ☆ △ ▽ ◁ □ [Aravamudhan 2009, Liu 2005, Xu 2008, Cho 2010, Kou 2009.,Shomski 2000] and ▷ □ [Fodor 2003, Dobrynin 2009].

4.2.4 Extracting SFD from AGFM

SFD can also be extracted from bulk magnetization curves (AGFM curves) averaged on a large area compared with MFM. In order to validate the MFM results, the SFD values obtained using AGFM and MFM have been compared and are shown in Figure 4.9.

As seen in the Figure 4.9, the SFD determined from these different measurements shows a good agreement and allows to state that they are equivalent. This suggests that in an assembly of non-interacting particles, the SFD corresponds to the intrinsic distribution of the assembly of particles and the measured distribution is independent of the measuring technique or protocol.

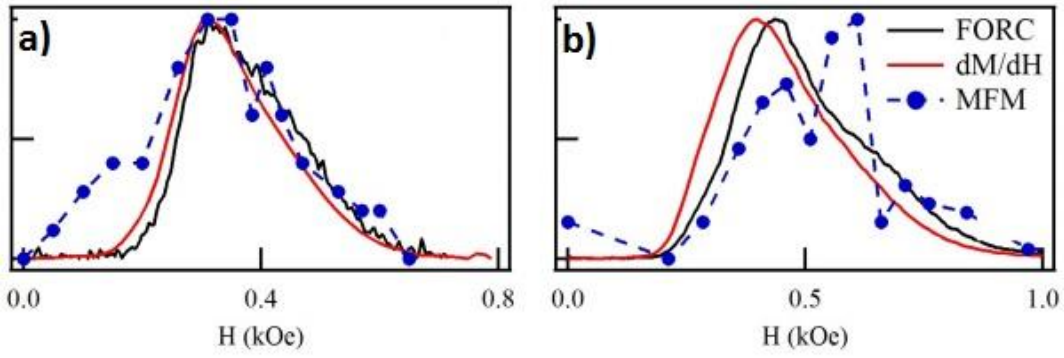

Figure 4.9: The SFDs measured using the FORC diagram, the (d*M*/d*H*) of bulk AGFM curve and MFM are shown for $Ni_{80}Fe_{20}$ (a) and $Co_{55}Fe_{45}$ (b) of 70 nm, respectively.

4.2.5 Effect of diameter size distribution on SFD

The SFD as a function of diameter for $Ni_{80}Fe_{20}$ NWs arrays is reported in Figure 4.10a. It decreases with increasing *D*, from 800 Oe for *D* = 40 nm to 320 Oe for *D* = 100 nm. These values are smaller than the ones determined for densely packed NWs grown in alumina templates where δ_{SFD} was more than 2 kOe (for *D* around 40 nm) [Carignan 2007, Nielsch 2001, Sorop 2003] and where strong dipolar interactions were present. It has been shown that the dipolar interactions in arrays of NWs with a fixed *D* and increasing *P* lead to a broadening of δ_{SFD} [Sorop 2004]. In our case, the packing density *P* is relatively low (< 1%) and decreases with

decreasing *D*, this mean that the broadening of δ_{SFD} with decreasing *D* is due to intrinsic effects and not from the dipolar interactions.

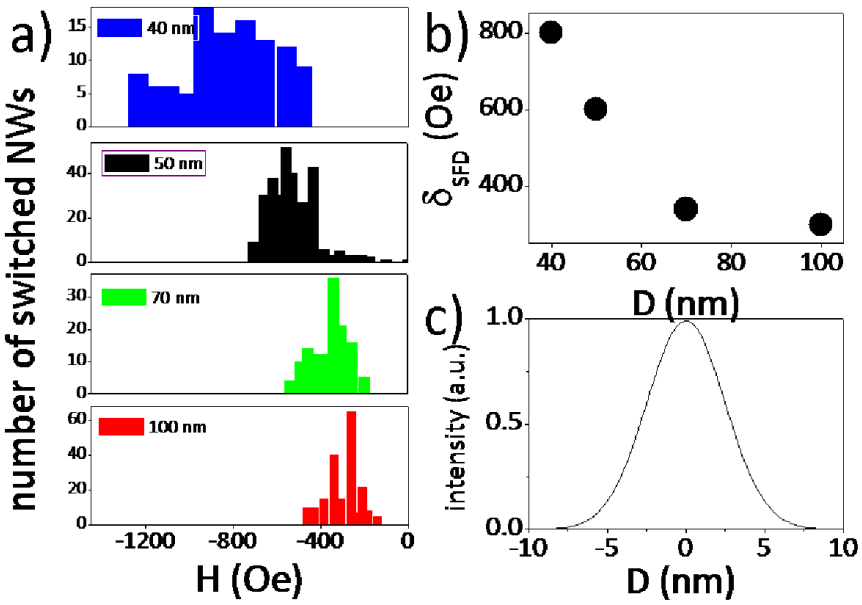

Figure 4.10: a) Switching field distributions of the different arrays of $Ni_{80}Fe_{20}$ NWs. b) Variation of the SFD width (δ_{SFD}) as a function of D. c) Gaussian distribution of the pores diameters.

Let us assume that δ_{SFD} is defined as $\delta_{SFD} = \delta^{D}_{SFD} + \delta^{0}_{SFD}$ where, δ^{D}_{SFD} is due to the size distribution of *D* and δ^{0}_{SFD} is due to the inhomogeneities in the structure and chemical composition of the NWs. We propose to separately determine δ^{D}_{SFD} and δ^{0}_{SFD} . For this purpose, we consider a Gaussian size distribution of the NWs diameter with a standard deviation of ± 5 nm (see Figure 4.10c). This assumption was taken into account after measuring the diameter size distribution of template pores and from the released NWs using SEM as shown in Figure 4.11.

Figure 4.12a presents the δ^{D}_{SFD} calculated in this way while Figure 4.12b shows that δ^{D}_{SFD} increases with decreasing *D* and is well fitted using a D^{-2} law. Note that the δ^{0}_{SFD} appears to be almost independent of *D* for the two NW arrays (triangles in Figure 4.12b) and is around the value of 350 Oe, which is quite low for our NW arrays in comparison with AAO NW arrays. This means that the significant contribution to the total SFD of AAO NW arrays and also of bit patterned media

[Chen 2012b] originates from non-intrinsic dipolar interaction effects. The δ_{SFD} measured in the present study is essentially intrinsic.

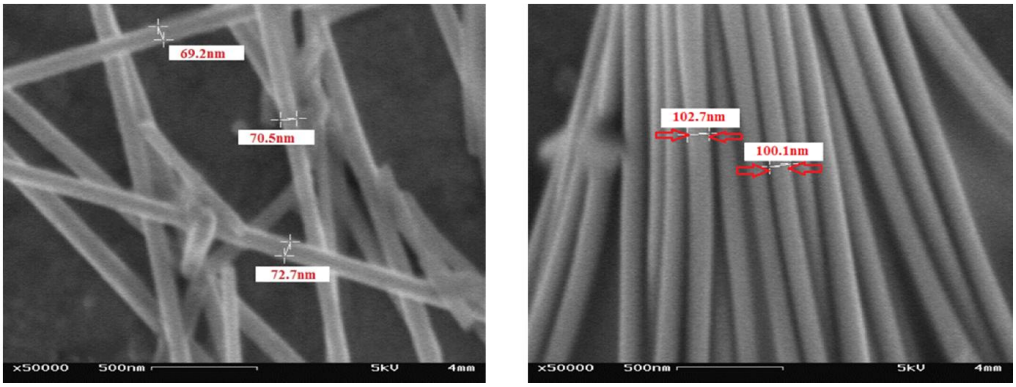

Figure 4.11: Diameter size distribution measured by SEM for 70 nm wires (left) and 100 nm wires released from the PC templates (right).

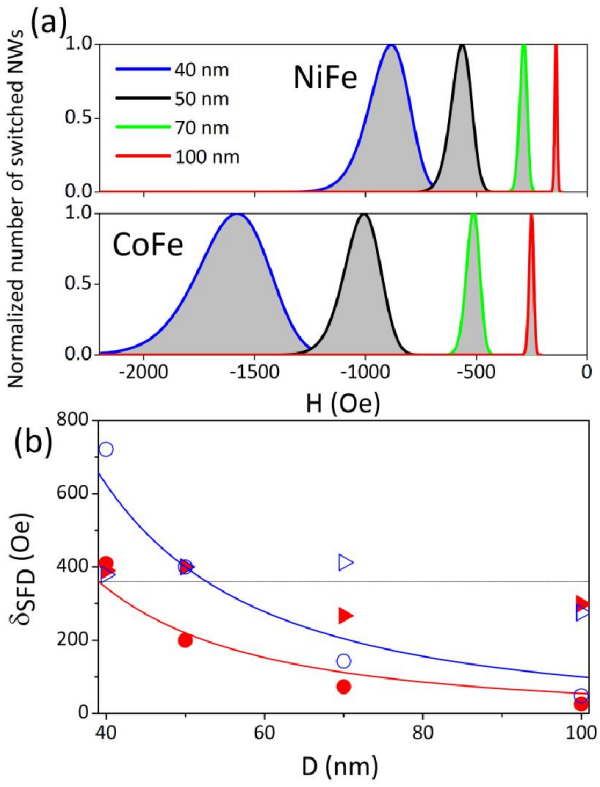

Figure 4.12: (a) Switching field distribution of $Ni_{80}Fe_{20}$ and $Co_{55}Fe_{45}$ nanowire arrays considering the Gaussian distribution of pore sizes for diameters in the range 40-100 nm; (b) Variation of the switching field distribution width as a function of diameter (circles) and its variation as obtained by separating the pore size distribution from the intrinsic contribution (triangles); the continuous lines are guide for the eyes, ▶●, ▷○; for $Co_{55}Fe_{45}$ and for $Ni_{80}Fe_{20}$ respectively.

For further differentiating the effects of intrinsic parameters and extrinsic parameters, MFM and FORCs have been performed on samples of same diameter but with various packing densities and the results are presented in chapter 5.

One may think that the broader δ_{SFD} for smaller diameters could be the consequence of an increased packing density and hence stronger dipolar interactions. Nevertheless, in the arrays under study, *P* slightly enhances with increasing *D* whereas δ_{SFD} is decreasing showing that influence of the σ_D on δ_{SFD} was more prominent for small *D.* If dipolar interactions were present, this would have led to the broadening of δ_{SFD} when *D* increases which is not the case in present measurements.

4.3 Conclusion

The magnetization reversal process in arrays of $Ni_{80}Fe_{20}$ and $Co_{55}Fe_{45}$ ferromagnetic NW embedded into low porosity nanoporous polycarbonate membranes has been studied systematically by *in situ* magnetic force microscopy. The fabricated NWs have high aspect ratio and negligible magnetocrystalline anisotropy, so the magnetization is expected to be parallel to the NW axis displaying bistable magnetic behavior. By analysing the numbers of NWs with magnetization up and down, local magnetization curves were obtained which agree well with bulk magnetization measurements from AGFM. The images taken under continuous magnetic field and in the remanent state were compared and found to be identical demonstrating that for these low density arrays there are weak dipolar interaction.

The influence of the diameter on the magnetization reversal and the SFD is shown. Regardless of the NW diameter, narrow SFD widths (δ_{SFD}) are observed compared to the ones generally obtained for densely packed NW arrays in AAO membranes. Moreover, an increase of δ_{SFD} with decreasing diameter is observed and is qualitatively explained by considering the diameter size distribution of the NWs.

Chapter 5

MFM investigation of arrays of nickel nanowires and nanotubes

The magnetic properties of arrays of nickel nanowires (NWs) of diameter ranging from 40 nm to 150 nm and nickel nanotubes (NTs) of diameter 150 nm, electrodeposited inside nanoporous polycarbonate membranes are investigated. The comparison of the nanoscopic magnetic force microscopy (MFM) imaging and the macroscopic behavior as measured by alternating gradient force magnetometry (AGFM) is made. It has been shown that MFM is a complementary technique that provides an understanding of the magnetization reversal characteristics at the microscopic scale of individual nanostructures. The local hysteresis loops have been extracted by MFM measurements. The influence of the shape of such elongated nanostructures on the dipolar coupling and consequently on the squareness of the hysteresis curves is demonstrated. It is shown that the nanowires exhibit stronger magnetic interactions than nanotubes. The non-uniformity of the magnetization states is also revealed by combining the MFM and AGFM measurements.

To analyse the effect of changing packing densities, NWs and NTs arrays of different packing densities were also studied by first order reversal curves (FORC). The quantitative analysis of the FORC measurements provides concrete information of the magnetic interactions and coercive field distribution in NWs /NTs arrays. A comparative MFM and FORC study was performed on varying packing density Ni NWs and NTs arrays. In an axial applied field on an array, each

entity is under the influence of the field emanating from the surroundings which strongly influences the magnetization reversal process. The results helped to differentiate the intrinsic and dipolar contributions for switching field distribution. Dipolar interactions were found to increase with the increase of packing density.

5.1 Effect of morphology on magnetization reversal of NWs/NTs

In chapter 4, effect of changing geometrical parameters has been discussed. Here we will elaborate, a) the effect of morphology i.e. filled vs hollow nanocylinders and b) effect of packing density on magnetic properties of NWs and NTs. Fabrication of NWs and NTs can be consulted in section 3.1.1 whereas sample preparation for MFM in section 3.1.2. Ni NWs and NTs have been employed to study the comparative behavior of wires and tubes. Table 3.2 gives the details of all the Ni samples used here.

In situ and *In field* MFM experiments (external applied field stays on during the measurements) have been performed under ambient conditions using an Agilent 5500 microscope (Agilent Technologies) equipped with a 100 µm closed-loop scanner, for high-precision control of the scanner position in *x* and *y* by attenuating the non-linear and hysteretic behavior of the piezo-positioners. So, in practice, we could scan the same area during all the measurements. The MFM probes, Asylum ASYMFMHC high coercivity (H_c = 5000 Oe) (Asylum) with a force constant around 2 $N.m^{-1}$ and a resonance frequency of about 70 kHz were used for this study. The use of high-coercivity probes allowed to avoid the magnetization reversal of the tip in the applied field range [-1000 Oe; +1000 Oe]. The experimental set up to perform *in situ* and *in field* MFM measurements has been presented in 3.2.3. The MFM-based magnetic hysteresis curves were obtained using equation 3.12.

Bulk magnetization curves were also obtained, using an alternating gradient field magnetometer (AGFM-Lakeshore) and were compared to the MFM-magnetization curves. The sample size was 2 x 2 mm^2 which contains a larger number of NTs and NWs. The AGFM measurements were performed on the same samples as for MFM

characterization, after the chemical etching of the Cr and Au layers which guarantees the same conditions for the arrays of NTs and NWs. Further, FORCs curves have been recorded using AGFM.

It is important to note that due to their different surface area, the effective packing density (*P*) for the NTs array is less than for the NWs array considering the same templates. Section 3.1.3 represents how to extract the *P*. PC templates of different *P* have been used. Ni NWs of diameters ranging from 40 nm to 100 nm were grown in templates of $P < 1\%$ and Ni NWs and NTs of diameter 150 nm in templates of $P \sim 6\%$ and ~ 10%. So, NTs have only been produced in medium density templates. Using equation 3.3 and by combining MFM and SEM images, the effective packing density in the NWs array is found to be $P_{NW} \sim 6\%$ *and* 10% *w*hereas, in NTs array it was $P_{NT} \sim 5\%$ *and* 9%.

After etching the cathode metals (Au and Cr) the NWs and NTs can be observed by SEM and MFM. For instance, NTs embedded in the PC membrane have been revealed as shown in Figure 3.3b. This surface corresponds to the one probed by MFM as well. Free NTs were also analyzed by SEM (see Figure 3.3c and Figure 3.3d). Figure 3.3d has been obtained from NTs electrodeposited in a PC membrane with a larger pore density ($P = 10\%$). From these images, the lengths of the studied NTs and NWs were found to be around 5 µm.

5.1.1 MFM images of NWs and NTs

Figure 5.1a present typical 10 x 10 μm^2 MFM images obtained at the top surface of the NWs array while in Figure 5.1b, images of the NTs array are presented. The corresponding topography images NWs and NTs samples are presented on top left of the Figure 5.1a and Figure 5.1b. The spot sizes (black or white) are larger than the nominal diameters (150 nm) of the NWs/NTs because the MFM tip measures their dispersive stray fields from the top and not their exact dimensions. One would expect NTs to have a non-uniform MFM signal because of their hollow inner core. The signal strength from NT (0.8 degrees) is weaker than the signal strength from NW (3.5 degrees) as shown in Figure 5.2. Nevertheless, from all the images, only

"uniform" white or black spots are distinguishable as a function of the applied magnetic field.

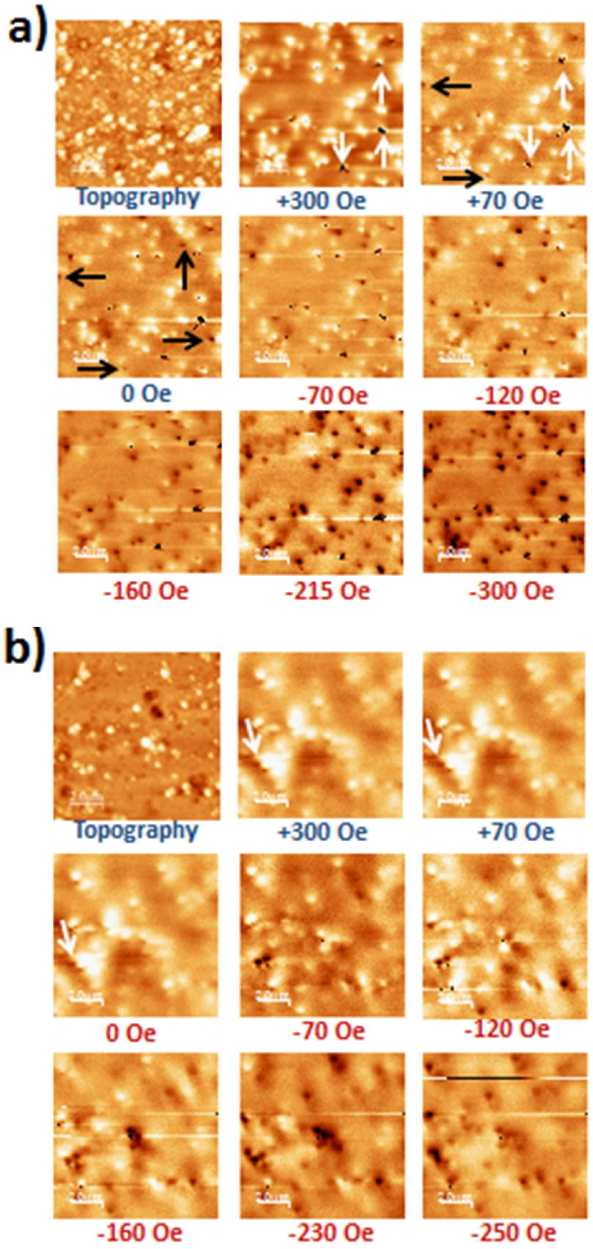

Figure 5.1: *In field* MFM images Ni NWs of diameter 150 nm and packing density ~ 6% (a) and Ni NTs of external diameter 150 nm and packing density ~ 5% (b) starting at saturation in a positive 300 Oe field and at various negative magnetic fields displaying the magnetization reversal progress. The images are scanned at a fix area (10 × 10 μm^2). The first image at top left of each series is the topographic image of the studied area (the height scale *z* ranges from - 50 to 110 nm). For the MFM images of the NW arrays at positive fields, white arrows point spots due to artifacts (VdW interactions) and black ones point to spots corresponding to switched NWs.

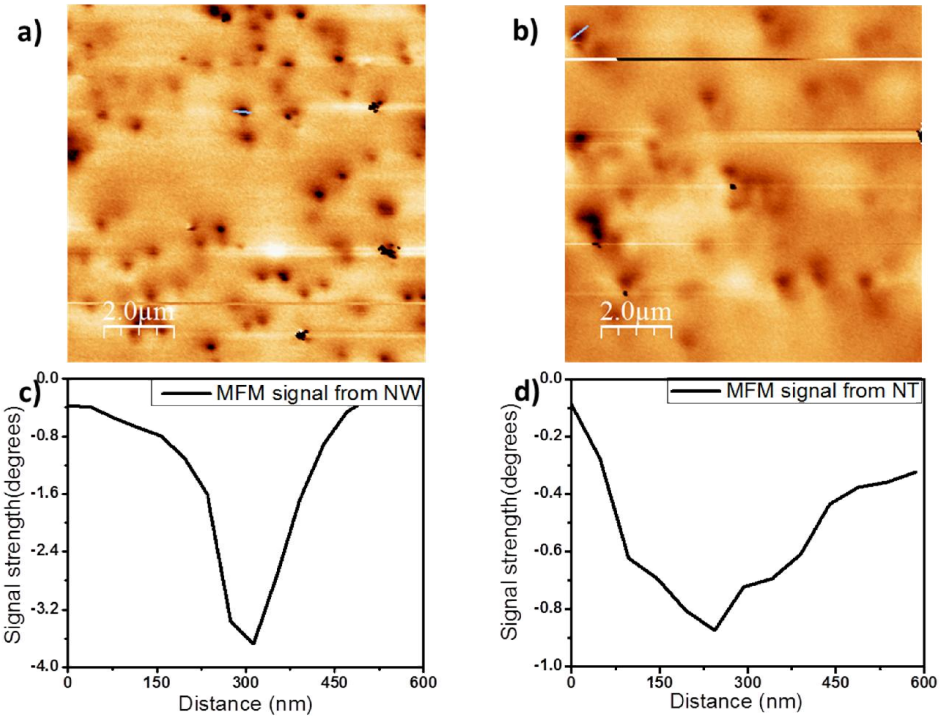

Figure 5.2: a) MFM image of an array of NiNWs (*D*= 150 nm) and b) MFM image of an array of NiNTs (*D*= 150 nm), c) and d) represent the corresponding MFM signals from a NW and a NT respectively. The NW has higher signal amplitude as it has more magnetic material (filled core) compared with NT (hollow core).

It has been demonstrated experimentally by MFM that the Ni NWs of 250 nm diameter show single domain structure whereas of 2µm diameter exhibit core-shell cylindrical domains [Sun 2009].The internal magnetic configurations could be complex but MFM measures only the stray field so it is not sensitive to give information on magnetic configurations of embedded magnetic nanostructures throughout the volume. Subsequently, the arrays of NTs and NWs have been treated as apparent bistable systems (uniform magnetization either parallel or antiparallel to the probe magnetization) to analyse the MFM images even if the magnetic moments distribution could be more complex. This behavior is discussed at the end of this section.

The second image (first rows) in Figure 5.1a and Figure 5.1b correspond to a state where all the NW/NT appear uniformly magnetized in a field H_0 = + 300 Oe along *+Oz* while the tip is magnetized along *-Oz*. Then, a series of magnetic fields along *–Oz* were applied. The successive switching of the NWs and NTs started around +200 Oe and - 70 Oe until the application of around -300 Oe and - 250 Oe

respectively. In contrast to the NTs, the switching of the NWs started even before reaching remanent state which results in some reversed NWs (dark spots) at zero applied field (pointed with black arrows).

In Figure 5.1b the black spots with horizontal straps from +300 Oe till 0 Oe (pointed with white arrows) are not due to the magnetic signals but to artifacts due to Van der Waals interactions acting on the tip that briefly touches the sample surface. These spots do not persist once the applied field and the tip stray field were in the same direction, Figure 5.1b from -70 Oe till -250 Oe.

Because only two contrasts (black or white spots) were identifiable from the MFM images, we made the assumptions that only two states are possible: “up” or “down”. Thus, the local- or MFM-hysteresis cycle has been calculated by counting the number of NWs (or NTs) with “up” states and “down” states and by using equation 3.22. The remanence was extracted from the image recorded at zero applied field. The (MFM)-coercive field was extracted from the image where the number of NWs/NTs with “up” and “down” states is same ($n_{up} = n_{down}$).

5.1.2 Hysteresis curves of NWs and NTs

Bulk magnetization curves with longitudinal applied magnetic field were also obtained by AGFM on a piece of the same sample used for MFM measurements. Figure 5.3 presents a comparison between the bulk magnetization curves for the NTs array (red continuous line) and for the NWs array (blue dashed line). These magnetization curves clearly reveal that the NTs curve is less tilted (more square) compared with the NWs curve. The remanence of the NTs array is about 0.8 while it is around 0.5 for the NWs array. Moreover, the saturation field for the NWs is about two times higher (~ 2000 Oe) than for NTs (~ 1000 Oe). These observations are, in first approximation, coherent with the observations made by MFM where the NWs reversal magnetization begins before and ends after the reversal of the NTs.

The difference of the two bulk magnetization curves could be understood solely in terms of the dipolar interactions and shape anisotropy contributions, since the

magnetocrystalline anisotropy contribution, in NWs and NTs, may be neglected [Encinas 2001,Wang 2005, Wang 2007]. Considering that the magnetization inside each NW and NT is uniform and because both NW and NT have the same symmetry with a large aspect ratio, the same mean field model used for NWs can be used for NTs, where the effective field H_{eff} in the saturated state is [Galvan 2014]:

$$H_{eff} = 2\pi M_s - 6\pi M_s P_{NW}(1-\beta^2) \quad (5.1)$$

where M_s is the saturation magnetization for Ni and P_{NW} is the effective packing density of the considered array. The first term of this equation corresponds to the shape anisotropy contribution which is same for both high aspect ratio NWs and NTs and the second term is the dipolar interactions contribution characterized by the effective packing density P_{NW} [Nam 2012, Fishbacher 2007]. It has already been discussed that due to their different volume, the packing fractions for NT (P_{NT}) is less than the NW (P_{NW}) which results in a weaker interaction field and thus a higher effective field and a strong uniaxial anisotropy for NTs. So, the key differences observed in their hysteresis loops arise from their respective effective fields.

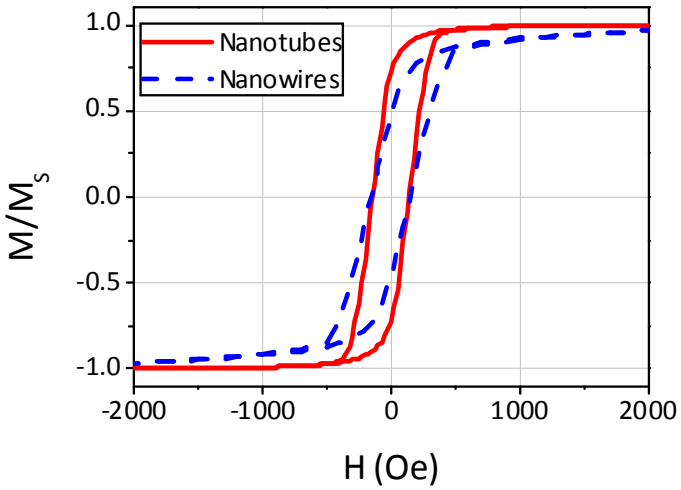

Figure 5.3: Normalized AGFM magnetization curves obtained with a magnetic field aligned along the revolution axis from the arrays of Ni NTs of external diameter 150 nm and packing density ~ 5% (red solid line) and Ni NWs of diameter 150 nm and packing density ~ 6 % (blue dashed line).

Moreover, the high packing value of the template results in strong dipolar interaction and broader switching field distribution (SFD) [Nielsch 2001, Navas

2005]. The shearing of hysteresis loops depends on the value of the dipolar interaction field so the hysteresis loops of NWs are more sheared than NTs [Sorop 2003].

5.1.3 Comparison between MFM and AGFM results

To predict the magnetic behavior of NWs/NTs similar approach as in previous chapters, comparing the MFM and AGFM curves was adopted. Unlike the results for low density NWs arrays of diameter below 100 nm, here the magnetometry and MFM hysteresis curves differ significantly, as presented in Figure 5.4 for the array of NWs (a) and for the array of NTs (b). The MFM hysteresis curves were obtained by analyzing the MFM images presented in Figure 5.1. From the MFM images, a remanence of 100 % was found in the case of NTs and around 80 % for the NWs while it reaches 80 % and 50 % from the AGFM curves, respectively.

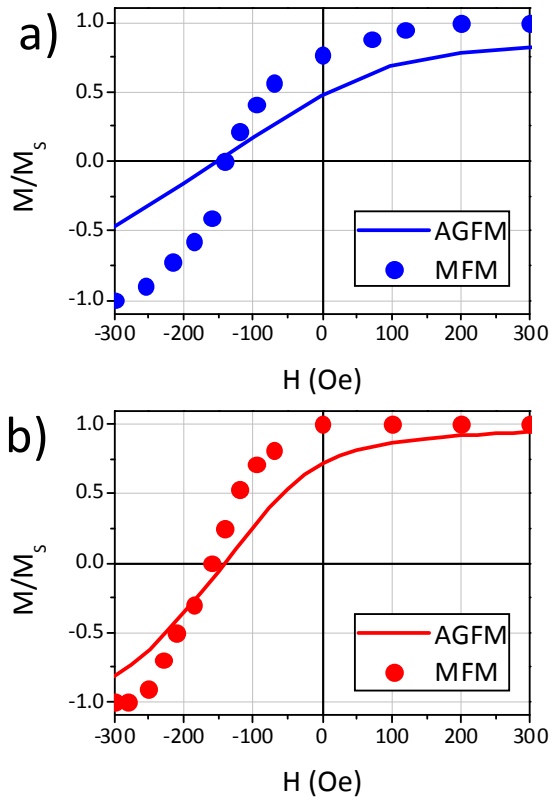

Figure 5.4: Comparison of the *in field* MFM magnetization curves with the ones obtained by AGFM measurements from the array of Ni NWs of diameter 150 nm and packing density ~ 5% (a) and Ni NTs of external diameter 150 nm and packing density ~ 5% (b), respectively.

Moreover, from MFM results a saturation field of 300 Oe is deduced in both investigations for NTs and NWs while from AGFM curves (Figure 5.3) it was found to be around 500 Oe and more than 2000 Oe for NTs and NWs arrays respectively. In contrast, the coercive field values obtained from MFM and AGFM curves are the same.

These comparisons show that the although MFM measurements presents only one binary state up/down for the NWs and NTs but internally there might be non-uniform magnetization states. It has recently been shown [Tabasum 2013] that a very good agreement between MFM and AGFM curves is found for arrays of ferromagnetic NWs in a state of uniform magnetization, i.e. single domain regimes for diameters less than 100nm. It is worth mentioning that different series of MFM images were taken at different areas of the samples and no significant changes were noticed on the resulting hysteresis loops. Hence, the antagonism between the local probing technique of the MFM approach compared with the bulk probing technique of AGFM can be excluded. In addition to being a local technique, MFM is a surface technique where the in-depth magnetic configuration cannot be probed whereas AGFM probe the whole volume of the NTs and NWs arrays (See schematic in Figure 4.6). The significant difference of the NWs/NTs AGFM curves and MFM curves could be due to a) dipolar interactions (as NTs have hollow structures so less magnetic materials volume to interact as compared to NWs) or b) due to non-uniform magnetization throughout their volumes. Further investigations to ensure that the mismatch between the bulk and local MFM hysteresis curves resulted from the non-uniform magnetization, *in situ* MFM measurements on the same areas (as in Figure 5.1) were performed. During these measurements the applied field was switched off during the MFM scan. The results obtained are presented in Figure 5.5. The NTs have remanence 1 whereas the NWs have 0.8 in both infield and *in situ* measurements. This fall of remanence of NWs compared with the NTs is an indication of stronger dipolar interactions. This has been further elaborated later in this chapter (section 5.2) that by increasing the packing density of NWs to 10% the remanence decreases to 0.35. It can been seen from the graphs

that the *in situ* and infield measurements in NTs coincide better than the NWs, further supporting that in NWs along with the non-uniform magnetic configurations dipolar interactions are stronger. This results in a bit of irregularity of the local switching events for *in field* and *in situ* MFM measurements.

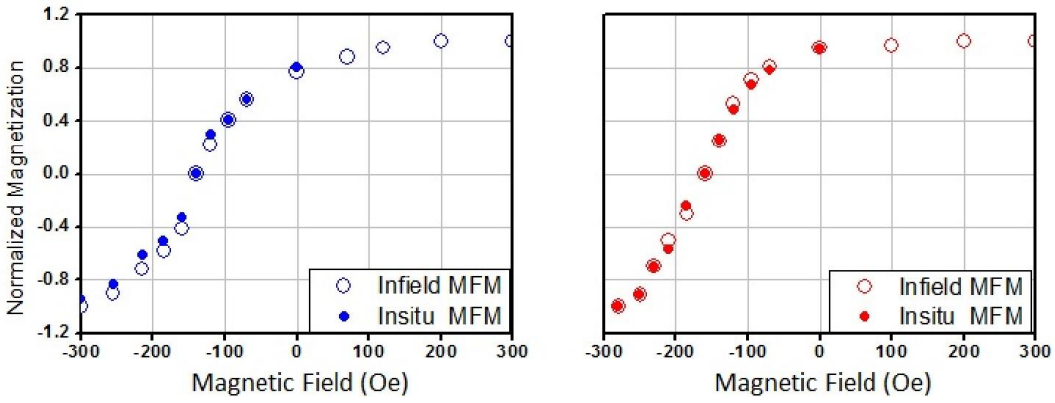

Figure 5.5: Comparison of the *in field* and *in situ* MFM magnetization curves for NWs of diameter 150 nm and packing density ~ 6% (left) and for NTs of external diameter 150 nm and packing density ~ 5% (right).

5.1.4 Non-uniform magnetic configurations

Indeed, the diameter of the studied NWs/NTs is around 150 nm which is far from the critical diameter below which a coherent rotation of the magnetization is expected for infinite Ni NW ($D_{coh} = 7.3\,\ell_{ex} \approx 54\,\text{nm}$ [Encinas 2001]) and non-uniform micromagnetic configurations could be present. This means that so apparently bistable configuration seen by MFM is not coherent in the whole volume of the NWs/NTs and complicated magnetic configurations may exist. Interestingly, from Figure 5.4, it can be seen that the mismatch between bulk and MFM measurements is less pronounced in the curves for the NTs array. This finding could be explained by the specific shape of the NTs compared to the NWs where the shell width is about 20 nm which prevents the presence of radial domains.

Therefore, from these comparisons, one can notice that in both cases, the micromagnetic configuration is certainly non uniform. To reinforce this argument, micromagnetic simulations for an isolated NT and for an isolated NW have been performed. The calculations have been performed using a flexible finite element micromagnetic simulation package [Fischbacher 2007] and the results are

presented in Figure 5.6. The numerical calculation method has been discussed briefly in section 3.7.

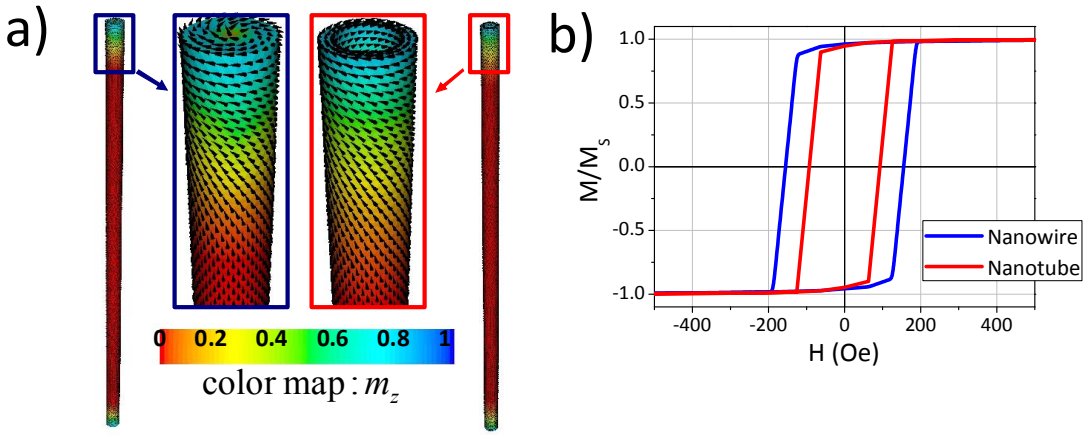

Figure 5.6: a) Magnetic moments distribution in an isolated NW and NT at zero applied field after applying a saturating field along the revolution axis. Colors encode m_z component of the magnetization (along the revolution axis). (b) Magnetization curves obtained for the isolated NW and the NT, respectively.

The dimensions used during simulations for the NWs are: length L = 5 µm and diameter D = 150 nm while for the NT L = 5 µm, outside diameter D_{out} = 150 nm and inside diameter D_{in} = 130 nm. Note that these geometrical dimensions are close to the experimental ones. The magnetic parameters: magnetization saturation $M_S = 0.48 \times 10^3$ emu.cm^{-3} and exchange stiffness $A = 1.0 \times 10^{-6}$ erg.cm^{-1} correspond to bulk values for Ni material. Indeed, it has been assumed that the electrodeposition method seems not to modify the intrinsic magnetic parameters [Ferré 1997, Staschkevich 2009]. The magnetic moments distributions at remanence (after saturating the NW and the NT along the revolution axis) are presented in Figure 5.6. It clearly depicts that the distribution at zero applied field is non uniform in both cases.

It is worth noting that contrary to the experimental hysteresis cycles (Figure 5.3), the calculated hysteresis cycles (Figure 5.6) are close one to each other (the coercive field of the NT is slightly weaker than the NW one) which strongly endorses that the main difference appearing between the experimental cycles is due to the higher dipolar interaction in NWs array, please see section 5.1.3. A quick overview of the already reported theoretical results further support these

observations that the magnetic domains and magnetization reversal inside an infinite NW and a NT of larger diameters is not homogeneous [Landeros 2007, Rozmann 2011, Chen 2012a, Lopez 2012]. In this work, this is indirectly shown experimentally by combining the MFM and AGFM measurements.

5.2 Effect of packing density on magnetization reversal of Ni NWs/NTs

Chapter 4 was devoted to present the effects of diameter size distribution in magnetic NWs on the SFD. The SFD widths extracted from our low packing density samples was very low when compared with the already presented values for high density samples. This section demonstrate the importance of using MFM coupled with the FORCs curves to get the in depth information of SFD width broadening due to intrinsic and extrinsic effects. To do so, the diameter of the samples (Ni NWs) is kept constant while the packing density is gradually increased.

5.2.1 Intrinsic SFD of low packing density Ni NWs

This section elaborates the method to obtain the intrinsic SFD from low packing density P < 1 % Ni NWs of diameters ranging from 40 nm to 100 nm (same as for NiFe and CoFe NWs in chapter 4). In such a low packing density of NWs, interwire distance is of the order of some hundreds of nm so the dipolar interactions can be neglected [Wang 2008, Tabasum 2013]. The length of the NWs was L = 4 µm with a standard deviation of ± 0.1µm as determined by SEM. The pores diameters (D) vary from 40 to 100nm with a standard deviation of the diameter σ_D of ± 5nm. It can be deduced from the MFM binary signals that high aspect ratio Ni NWs are expected to have single domain configuration below D_{cr} = 500 nm, see Figure 2.7 [Nielsch 2001, Sun 2005]. The domain wall width $\delta_{wall} = \pi\sqrt{A/K}$, where A is the exchange stiffness and K is the magnetocrystalline anisotropy, for Ni is 120 nm [Alberto 2009]. Consequently, two remanent states are expected to be seen by MFM and correspond to magnetization aligned along *+Oz* and *–Oz* (*+Oz* being the NW's axis direction). Figure 5.7 presents typical MFM images obtained from the array of Ni NWs (D = 100 nm). Before starting the experiments, the NWs arrays were

magnetically saturated along their axis (*+Oz*) under a magnetic field of *H* = + 2 kOe while the MFM probe tip's magnetization is in the opposite direction (*-Oz*). This resulted in attractive bright contrast for the NW on the MFM phase images (top left image of Figure 5.7). Then, the magnetic field was applied in the direction of the magnetization of the probes (*-Oz*) to switch the magnetization of the NWs. The successive switching of the NW started after the application of around - 140 Oe until the application of around - 500 Oe.

From the MFM images, it was confirmed that only two remanent states are stable inside each NW corresponding to single domain NW with "up" (along *+Oz*) and "down" (along *-Oz*) magnetisation directions. Consequently, the local hysteresis curve was calculated by counting the number of NW with "up states" and "down states". Thus, the normalised magnetization can be obtained using the equation 3.12.

The NWs have large aspect ratio; they have almost 100% remanence extracted from MFM images and 97% remanence obtained from AGFM curve. The lower remanence obtained from AGFM could be explained by considering that the size of the NWs is 100 nm so apparently single domain NWs (MFM scans) may have complicated and non-uniform magnetic configurations along their length. They reverse their magnetization via irreversible jumps as shown in MFM images. Nevertheless, MFM magnetization curve (solid dots) of 100 nm Ni NWs array shows a very nice match with the bulk AGFM cycle (line), plotted in Figure 5.7. The small deviations that appear between these two measurements can also be attributed to the fact that a limited number of NWs is probed using MFM (local study) while the whole set of NWs is probed using magnetometry measurements.

The MFM-magnetization curves, using the above mentioned procedures, have been obtained from the different Ni NW arrays (solid dots) and shown in Figure 5.8a. Similar to Figure 5.7 and results presented in Figure 4.5 for NiFe and CoFe NW arrays, the results from MFM and AGFM for NWs arrays of different diameters (40-70 nm) were in good agreement. The variation of H_C as a function of *D* is

represented in Figure 5.8b; it increases with decreasing *D.* It ranges from from H_C = 320 Oe for *D* = 100nm to H_C = 650 Oe for *D* = 40nm. In our previous works on low density NiFe and CoFe similar behavior was observed (chapter 4).

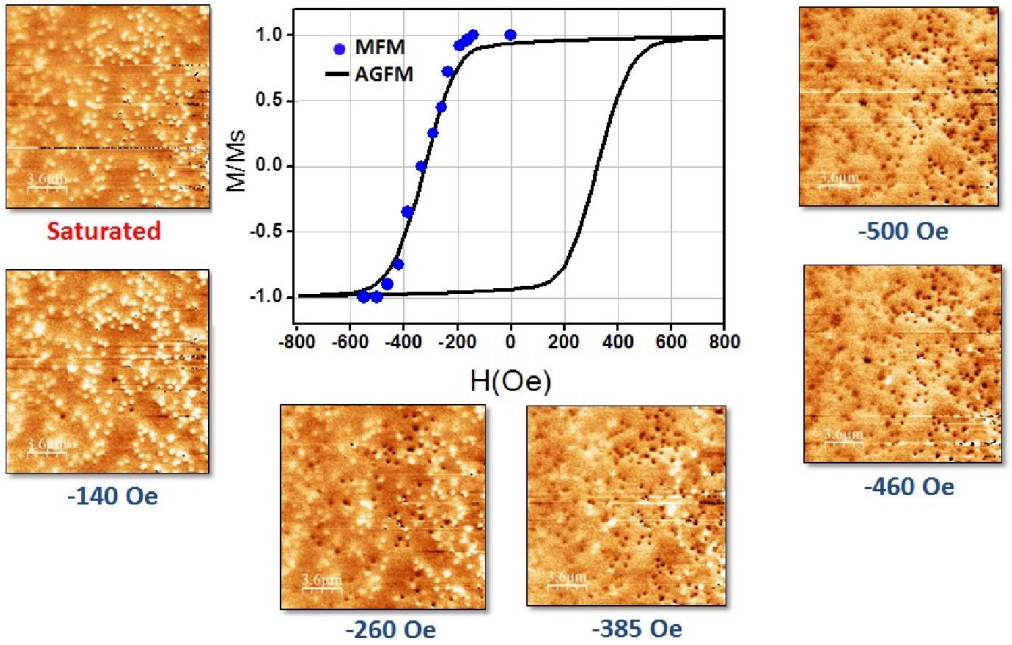

Figure 5.7: Array of Ni NWs of diameter 100 nm and packing density < 1%: series of MFM images (taken at zero applied field) indicating the progress of magnetization reversal after saturation in a positive field (H=+2 kOe) and for different negative applied fields.

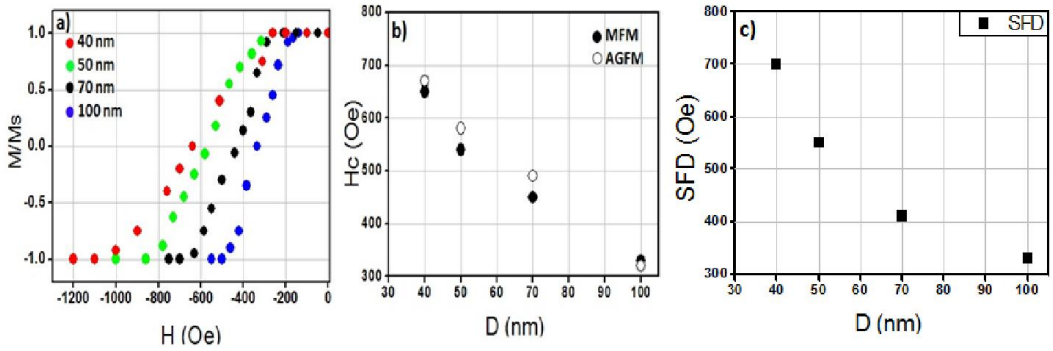

Figure 5.8: a) MFM-magnetization curves (solid dots) for the different arrays of Ni NWs of packing density < 1%, b) measured coercive field H_C and as function of D and c) measured switching field distribution SFD as function of D.

It is well know that the H_C of an infinite NW, of certain diameter called critical diameter, in the coherent rotation model is given by $H_C = 2\pi M_S$ and does not depend on the diameter. Nevertheless, our NWs are not infinite and have

diameters larger than $D_{coh} = 7.3\ell_{ex} \approx 54nm$ (ℓ_{ex} being the exchange length) which corresponds to the diameter beyond which non uniform reversal modes such as curling can occur, except for arrays of NWs of diameter 40 nm where coherent reversal is expected [Sun 2005, Aharoni 1958, Ferré 1997]. In curling mode, neighboring magnetic moments are not constrained to be parallel so there is no net magnetization along the hard axis hence minimizing the demagnetization energy (for details please consult section 2.8 and the sub sections therein).

As, it has been the subject of discussion in previous chapters that the SFD is linked with the number of switched NWs at each increment of the applied field and have been determined as a function of the applied fields. The SFD width (δ_{SFD}) corresponds to the difference between the field of first reversed NW and the last one. It decreases with increasing *D*, from 700 Oe for *D* = 40 nm to 360 Oe for *D* = 100nm (Figure 5.8c). These values have been obtained from similar MFM images as the one shown in Figure 5.7 for diameter 100nm. The broadening of δ_{SFD} for smaller *D* compared with the larger *D* is mostly due to intrinsic effects such as diameter size distribution and not from the dipolar interactions (as seen in chapter 4). As the arrays have low *P* < 1% hence interwire distance in the present systems is large enough to neglect the effects of dipolar coupling.

These values are smaller than the ones determined for densely packed NWs grown in alumina templates where δ_{SFD} was more than 2 kOe (for *D* around 40 nm) and where strong dipolar interactions were present [Asenjo 2006, Sorop 2003, Nielsch 2001]. Similar results, on low packing density NiFe and CoFe NWs have been reported in chapter 6, mentioning the detailed procedure how to extract the diameter size distribution dependence of intrinsic δ_{SFD} and illustrating that this contributes in broadening of SFD. The SFD of medium and high packing density systems will be understood in terms of intrinsic contributions and dipolar interactions contribution obtained using the FORC, in next sections.

5.2.2 Dipolar interactions in different packing density NWs arrays

Once the intrinsic contribution of broadening of the SFD is acquired in almost non-interacting NW arrays, it is sufficient to choose the array of NWs of any diameter and vary the packing density to learn the dipolar interactions contribution in the broadening of SFD width. This is done by measuring the several minor hysteresis curves on the samples and the FORC diagrams. NW arrays of diameter 100 nm but various packing densities i.e. $P < 1\%$ and $P \sim 4\%$ have been used.

5.2.2.1 FORC measurement

The goal of any FORC measurements (principle of these measurements has been explained in section 3.2.2) is to retrieve the coercivity H_c and interaction H_u parameters of arrays of interacting nanomagnets. Figure 5.9a and Figure 5.9c represent the FORC curves from arrays of $P < 1\%$ and $P \sim 4\%$ respectively.

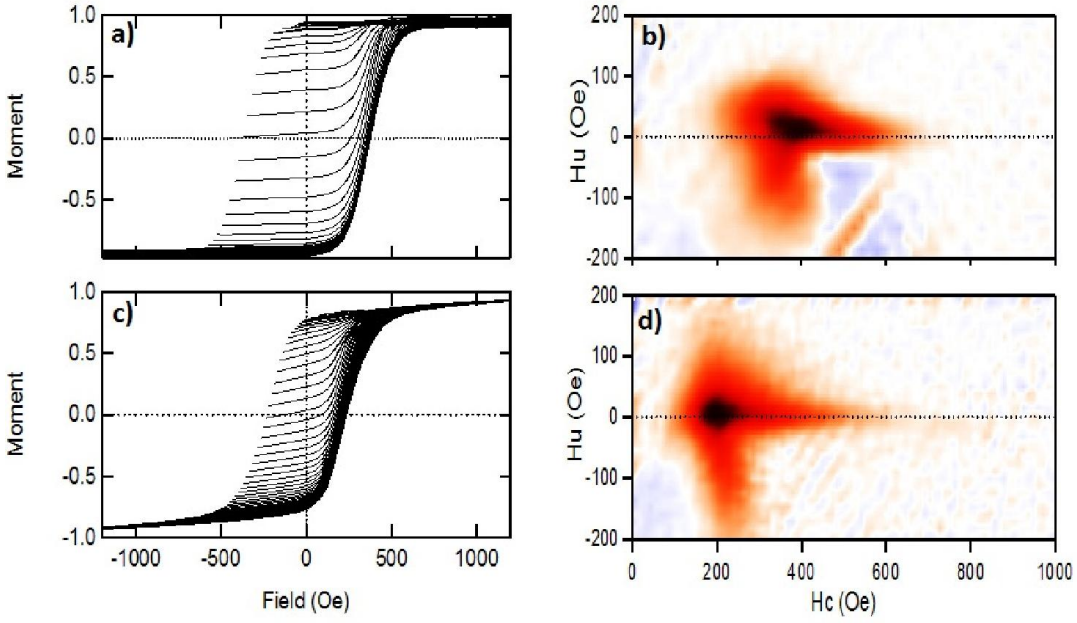

Figure 5.9: FORC curves of Ni NWs (100nm) $P< 1\%$ (a) and corresponding FORC diagram (b). FORC curves of Ni NWs (100nm) $P \sim 4\%$ (c) and corresponding FORC diagram (d).

The first impression of these curves demonstrate the decrease in remanence from 0.95 for $P < 1\%$ to 0.75 for $P \sim 4\%$ indicating that the switching of the wires in medium P arrays has started at remanence. As the diameter is same in both the cases so is the diameter size distribution which causes broadening of intrinsic SFD

(as shown in chapter 4). Therefore, it can be concluded that this decrease in remanence is due to the presence of the dipolar interactions. The distribution of the interaction fields and the coercive fields from the FORCs can be obtained using equation 3.7 and is presented in Figure 5.9b and Figure 5.9d from low and medium density NWs arrays, respectively.

5.2.2.2 Broadening of coercivity and interaction fields

By analyzing the FORC results one can observe that the FORC distribution along H_u axis in medium density (P = 4%) arrays is relatively pronounced. It has been reported that the half width of the FORC distribution along H_u axis (ΔH_u) can be used as an estimate of the dipolar interaction field between NWs at saturation which turns out to be 55 Oe in low P and 110 Oe in medium density arrays [Proenca 2013, Béron 2008]. For the 100 nm NWs arrays intrinsic δ_{SFD} was 360 Oe (see section 5.2.2.1). Ideally, the SFD width for non-interacting arrays was supposed to be mainly from diameter size distribution (as concluded from chapter 4) but the FORCs have shown a contribution of interaction field as well. In principle, in the samples of P < 1%, there should be no distribution along H_u axis as the magnetic entities are far enough to effect the nearest neighbors but in PC membrane, the random distribution of pores lead to the presence of random interwire distances and thus a minor H_u distribution. Quantitative calculations of interaction field depending upon the distance from the nearest neighbors have been performed in next chapter. This distribution is directly dependent upon the diameter and broadens with increasing packing density as shown in Figure 5.9d and the increase is more prominent for high density NWs arrays as depicted in section 5.2.2.3.

The coercivity distribution along with the possibility of obtaining the interaction field effects can be interpreted from FORCs. The width of H_c distribution is believed to be an outcome of not only intrinsic δ_{SFD} but also the mean field dipolar interactions [Pike 2005, Dobrota 2013]. This explains shearing of minor hysteresis curves (Figure 5.9c) and the broader H_c distribution (Figure 5.9d) in arrays of medium packing density. Generally the coercive field is same for the NWs arrays with same diameter but here it has unexpected higher mean value (Figure 5.9a and

Figure 5.9b) in so called non-interacting systems compared with weakly interacting arrays (Figure 5.9c and Figure 5.9d). The origin of this fact is quite controversial but different assumptions were made explaining that its origin lies in the interplay between shape anisotropy and the interaction field [Béron 2008, Dobrota 2013]. In densely packed NWs array the dipolar interaction reduces the coercivity significantly compared with an isolated wire. When the shape anisotropy dominates the demagnetizing interaction field in in-homogenously filled membrane the coercivity had higher values [Ferré 1997, Sorop 2003, Schlorb 2010]. Further it has been reported that a better control of the wire diameter results in very small dispersion of the coercive field values [Dobrota 2013].

5.2.2.3 Dipolar interaction in high density NWs and NTs

Figure 5.10 shows the FORC results obtained for NWs of *P*~10%. The shearing of the minor hysteresis curves and the broadening of the FORC distribution along H_u axis is solely the result of the dipolar interactions. The remanence, as observed from Figure 5.10 (left), is only 0.4 compared with 0.75 and 0.95 of the medium and low packing density arrays respectively. The distribution of the interaction field, Figure 5.10 (right), is increased significantly i.e. ten times more than the low packing density arrays. These observations testify already presented results in the previous section. Keeping the diameter same and increasing the *P* will enhance the proximity of the neighbors hence the strength of dipolar interactions. These interactions will tremendously increase the SFD width.

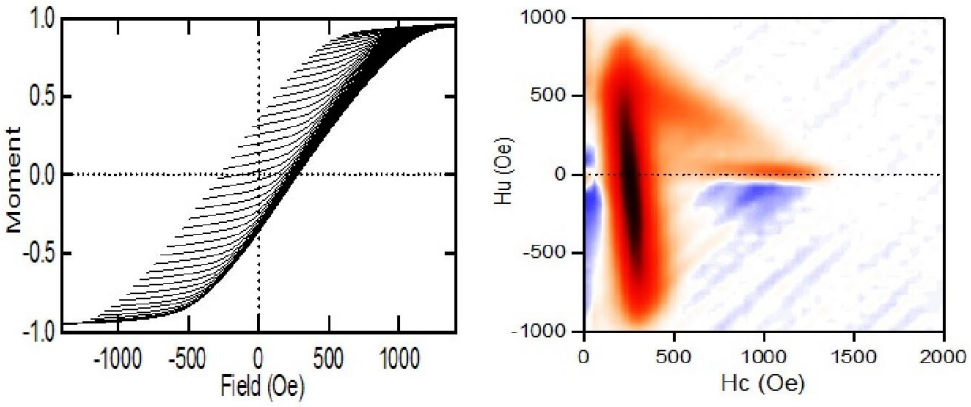

Figure 5.10: FORC curves of Ni NWs (100nm) P ~ 10% (left) and corresponding FORC diagram (right).

The SFD width which is the difference of start and end of switching events, of the low *P* samples (considered intrinsic SFD) is only 360 Oe (Figure 5.7), whereas for the *P* ~ 10% it is more than 3000 Oe (total SFD from Figure 5.10). Table 5.1 summarizes the effect of changing *P* on the SFD for Ni NWs and NTs arrays. It can be noticed that SFD increases with increasing packing density in NWs. However, NTs don't follow this trend (see section 5.2.2.4).

According to the best of our knowledge the FORCs have not been performed experimentally on arrays of NWs fabricated in PC membranes where the *P* can be as low as < 1% to differentiate the intrinsic and dipolar contributions for SFD broadening. In this work for the 100 nm Ni NWs array, the intrinsic contribution of the SFD is 300 Oe, from section 5.2.1 and 5.2.2. The broadening of the SFD ~700 Oe and ~2700 Oe for *P* ~ 4% and *P* ~ 10% respectively, come evidently from the dipolar interactions. This led the prominent stretch in H_u values from 200 Oe for non-interaction NWs arrays to 2000 Oe for strongly interacting. In case of NTs as the dipolar interactions are not very significant so SFD even for *P* ~ 5% is only 300 Oe and so does H_u. The coercive field for the same diameter NWs remains the same (250 Oe). But there is discrepancy observed for H_c values between low density and high density NWs arrays which has been discussed in section 5.2.2.2.

Table 5-1: Effect of packing density on SFD for arrays of Ni NWs and NTs.

Sample	Diameter (nm)	SFD (Oe)	P (%)	H_c (Oe)	ΔH_u (Oe)	Remanence	H_s (Oe)
Ni NW	100	360	< 1	350	200	0.95	500
--	100	~1000	~ 4	250	360	0.75	500
--	100	~3000	~ 10	250	2000	0.4	1500
--	150	~4000	~ 6	160	x	0.5	2000
Ni NTs	150	300	~ 9	160	300	0.65	500

5.2.2.4 MFM scans on high density NWs/NTs arrays

To investigate the effect of dipolar interactions, MFM scans which provides the information on magnetization reversal at nanoscale, have been performed on NWs and NTs. Figure 5.11 presents typical *in situ* MFM images obtained from the array

of Ni NW of *P* ~10 % (*D* = 100 nm). Before starting the experiments, the NWs arrays were magnetically saturated along their axis (*+Oz*) under a magnetic field of *H* = + 2 kOe while the MFM probe tip's magnetization is in the opposite direction (*-Oz*). In fact, when the applied field is removed, if there are no dipolar interactions and reversible switching phenomena of NWs, this should result in attractive bright contrast for the NW on the MFM phase images as in the top left images of Figure 5.1 and Figure 5.7. The observed image at remanence (top left of Figure 5.11) showed that many of the wires have been switched from white contrast to black when the applied field was removed. The observed image is in agreement with Figure 5.10a where the remanence is drastically dropped as compared to low density samples. This means that the nearest neighbors had a strong influence which resulted in favourable antiferromagnetic switching of many of the wires [Nielsch 2001, Schlorb 2010].

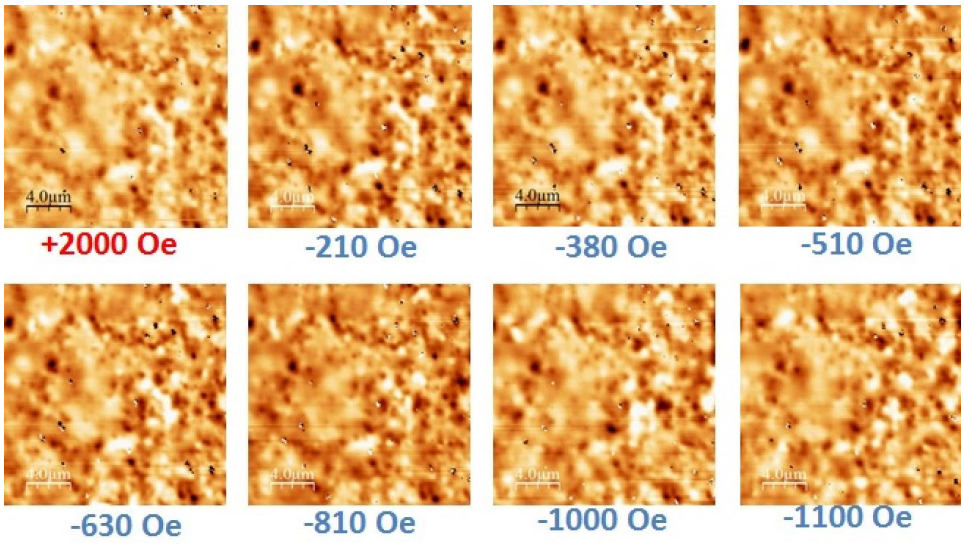

Figure 5.11: Array of Ni NWs with *D*=100nm and P ~ 10 %: series of MFM images (taken at zero applied field) indicating the progress of magnetization reversal after saturation in a positive field (H = +2 kOe) and for different negative applied fields.

In addition the incremental magnetic field in the direction of the magnetization of the probes (*-Oz*) to switch the magnetization of the NWs indicated that there will be a reversible switching of wires in the absence of the fields (at remanence) supporting once again the presence of stronger dipolar interactions modifying the switching behavior of the array. As the NWs switch in the absence of the field, so

using the *in situ* MFM measurements it is not possible to extract the hysteresis curves. The same is true for *in field* MFM measurements as the probes which could be used for *in field* measurements set up are not appropriate for high packing density NW arrays.

In order to investigate and compare the influence of the dipolar interactions in high packing density NWs/NTs, MFM and AGFM measurements have been done on the Ni NT in PC membrane of pore density ~ 10% and effective packing density of *P* ~ 9% calculated using equation 3.3. The results obtained have been shown in Figure 5.12. At 0 Oe i.e. at remanence there are only some NTs which have already switched their magnetization directions and then the reversal of the rest of the tubes happened at certain incremental negative applied fields till the application of the -400 Oe field. This indicates that the interaction field in NTs is weaker than the NWs and has been further proved by FORC measurements shown in Figure 5.13. It is worth noting that the magnetic contrast in NTs is less than NWs due to their hollow magnetic structure, thus weaker stray fields.

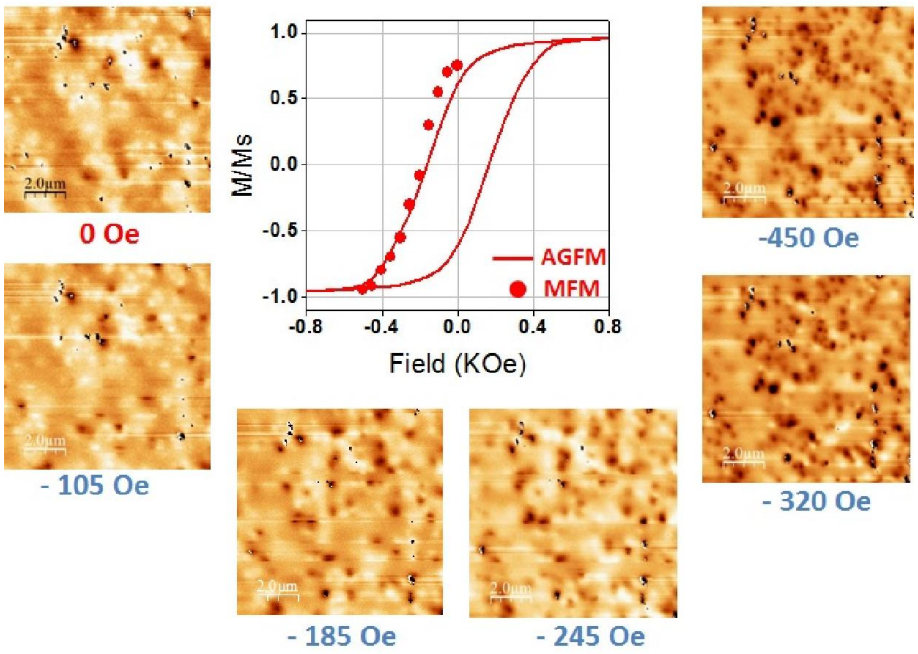

Figure 5.12: *In situ* MFM images of Ni NTs of P ~ 9% starting at remanent state, 0 Oe, and at various negative magnetic fields displaying the magnetization reversal progress. The images are scanned at a fix area (10 × 10 μm^2).The graph showing the MFM (solid spheres) and AGFM measurements (solid lines).

The shearing of the minor hysteresis curves and the broadening of the FORC distribution along H_u axis is not glaring when assessed with respect to NWs (see Figure 5.10). The remanence as observed from Figure 5.12 and Figure 5.13 (left), is more (0.65) than for NWs of same diameter where it was only 0.4. One should note that diameter of the NTs is 150nm so for the same packing density (~ 10 %), NTs are less densely packed than NWs. Thus, the distribution of the interaction field in NTs, Figure 5.13 (right), was very narrow and was comparable with medium packing density (P ~ 4 %) NWs arrays.

Using the analytical models developed by Béron et al. and Proença et al. and matching them with our experimental results on NWs and NTs, it is straight forward that distribution along H_u axis in NTs is mainly from the intrinsic effects and not very significant from inter tube interactions [Béron 2008, Proenca 2013]. This is further reinforced by the MFM results on high density NWs and NTs, showing the interaction field is very low in NTs. Furthermore, the SFD in NTs is lesser, a factor of 3, than in NWs as observed from Figure 5.13 (left) and Figure 5.10 (left). In recent reports on MFM investigation of medium density NWs and NTs, similar behavior has been observed [Tabasum 2014].

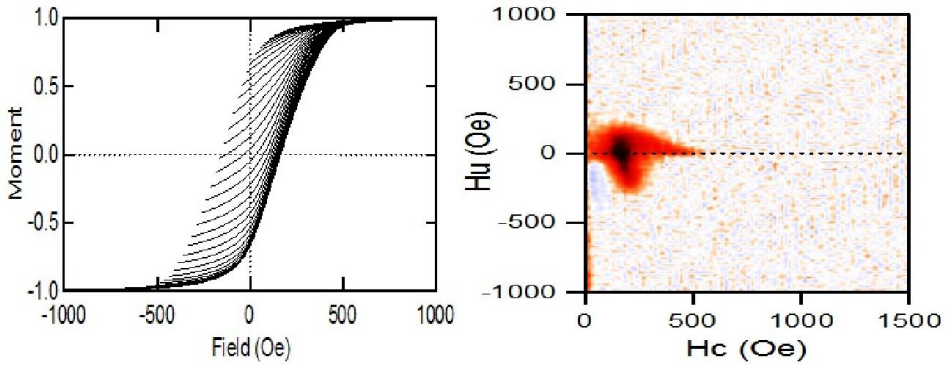

Figure 5.13: FORC curves of Ni NT (150nm) P ~ 9% (left) and corresponding FORC diagram (right).

In addition, the diameter of the studied NWs is around 100 nm which is far from the critical diameter below which a coherent rotation of the magnetization is expected for infinite Ni NW ($D_{coh} = 7.3\ell_{ex} \approx 54$ nm). Therefore, more complicated reversal mechanisms, e.g. vortex reversal could be present in NWs than in NTs (hollow internally) leading to the better and sharper defined coercivities in NTs. It

has been shown in a comparative study on NWs and NTs that the magnetization in the NW arrays is found to reverse by the nucleation and propagation of a transverse-like domain wall. On the other hand, for the NT arrays a non-monotonic behavior occurs above a diameter of 50 nm, revealing a transition between the vortex and transverse reversal modes [Proenca 2013]. Based on the method presented by Han et al. [Han 2009] and Wang et al. [Wang 2011] Ni NTs of different diameters from 25 nm to 220 nm, the decrease in coercivity and remanence with increase in diameter were ascribed to the stronger dipolar interactions (as the pitch was reduced with increasing diameter) and formation of polycrystalline structures.

The vortex domain wall formation is more favorable in NWs than NTs at higher diameters. This finding could be explained by the specific shape of the NTs compared to the NWs where the shell width is about 20 nm which prevents the presence of radial domains, see Figure 5.6 [Tabasum 2014]. The small distribution along the H_u axis in NTs under study is expected to be mainly from intrinsic effects such as, diameter distribution, non-parallel NTs in PC template and non-uniform micromagnetic configurations.

5.3 Conclusion

The magnetization reversal process of Ni NWs and NTs arrays in PC template have been investigated using MFM and AGFM. By comparing the magnetization curves obtained from both techniques, it has been demonstrated that they are complementary if one wants to get an insight of the dipolar coupling and the magnetization reversal process. The presented results helped us understanding their magnetization reversal. For instance the mismatch of the magnetization curves in both cases reveals that the micromagnetic configurations inside the NWs and NTs are not coherent. This means that hysteresis curves obtained using AGFM are accurate globally as they take into account the magnetization of the whole nanostructure whereas MFM gives the information of the local switching events in binary signals from the measured stray field of magnetic NWs and NTs (up/down magnetization).

A comparative MFM and FORC study on varying packing density Ni NWs arrays and high packing density Ni nanotubes has also been presented. The analysis of the FORC measurements provides information of the magnetic interactions and coercive field distribution in magnetic entities. This work provides a method to get an insight into the intrinsic SFD of magnetic particles using MFM and the contribution of the dipolar interactions in their total SFD by employing FORC. It has been shown that the intrinsic SFD represents only a fraction of the total non-intrinsic contributions (dipolar interactions) in the high packing density NWs. MFM provided the footprints of magnetic dipolar interactions for individual magnetic NWs/NTs in the arrays. Comparison of the high packing density NWs with the NTs exhibited significantly low dipolar interactions fields in NTs, hence narrow SFD. This shows that high density NTs arrays with strongly reduced switching field distribution can be achieved.

In future, NW/NTs are expected to be used in various applications such as nanobarcodes, sensors and patterned media. The precise control over the inside cavity by modifying the wall thickness opens the possibility of getting negligible interaction fields in NTs which is interesting for applications where this parameter needs to be minimized. Controlling geometric parameters such as diameter, length, tube thickness and pitch in NWs/NTs can be useful to tune the magnetic properties of high density magnetic structures. Furthermore, MFM scans may be used to distinguish the magnetization reversal behavior of isolated and individual entities of controlled dimensions in assemblies before their implementation in novel devices is realized.

Chapter 6
Quantitative measurement of dipolar interaction field by MFM

6.1 Introduction

The dipolar interaction field (IF) plays an important role in the magnetic properties of particle arrays such as the effective magnetic anisotropy and the broadening of the SFD [Richter 2006]. In parallel arrays of NWs, it tends to demagnetize or reverse the magnetization of individual neighboring wires and by increasing the packing density of the arrays, there is a decrease in the effective shape anisotropy of individual magnetic entities leading to a less stable magnetic configuration and even to the magnetization easy axis reversal [Encinas 2001, Schlorb 2010]. The IF can be obtained from the DC demagnetization (DCD) remanence curve and the isothermal remanent magnetization (IRM) curve and first order reversal curves (FORC) averaged over a large nanowire or nanotube arrays [Proenca 2013, Martinez 2013, Galvan 2014]. Magnetic force microscopy (MFM) has been found to be an interesting approach to probe locally and supply valuable information about the magnetization reversal process [Nielsch 2002, Wang 2008, Yuan 2008]. In some conditions, MFM may also be used to locally manipulate the magnetization in arrays of ferromagnetic NW [Kyali 2004]. It has been shown in recent studies that due to its lateral resolution, MFM imaging is complimentary to perform magnetic characterizations along with other magnetometry techniques [Tabasum 2013a, Tabasum 2013b, Tabasum 2014].

In this contribution, MFM has been used to quantitatively determine the local and

environmental dependent as well as the average interaction field in arrays of $Co_{55}Fe_{45}$ NWs. It is shown that the value of the local interaction field can be extracted directly using MFM by measuring the shift along the field axis of hysteresis curve of a single magnetic wire. Local nanoscale analysis considering different areas of the samples allows visualizing the effects of the particular environment. In particular, the dependence of the interaction field with the first neighbor inter-wire distance. Moreover, it is shown that the average of the locally measured interaction fields tends towards the mean field value as the number of measurements considered in the average is increased. The good agreement obtained by comparing with the values of the interaction field determined from a macroscopic measurement, micromagnetic simulations and a mean field model, validates the MFM approach while it provides a clear interpretation of the measurements.

6.2 Experimental Details

Arrays of $Co_{55}Fe_{45}$ NWs with diameters of 70 nm and 40 nm have been fabricated by standard 3-probe electrodeposition into the nanopores of track-etched polycarbonate (PC) membranes with porosities of 0.2% and 3%, respectively. Details of NWs fabrication can be found in section 3.1.1. The sample preparations for MFM and SEM have been detailed in sections 3.1.2 and 3.2.1 respectively.

To show the entire shape of the NWs by SEM, PC membranes have been dissolved in dichloromethane. Droplets of the dichloromethane suspension were spread on a substrate (membrane filters from Millipore) to well dissolve the PC membrane, leaving only the exposed NWs. *In situ* MFM experiments have been performed under ambient conditions using Dimension Icon (Bruker®). The scan size, was 10 x 10 μm^2 containing some tens of NWs in samples of $P \sim 0.2\%$ and 5 x 5 μm^2 of $P \approx 3$ % containing hundreds of NWs. The MFM probes, Asylum ASYMFMHC high coercivity ($H_c = 5000$ Oe) (Asylum™) with a force constant around 2 $N.m^{-1}$ and a resonance frequency of about 70 kHz were used for this study. The choice of high-coercivity probes allowed to avoid the magnetization reversal of the tip in the

applied field range [- 1000 Oe; + 1000 Oe] of the experiments. MFM principle has been described in section 3.2.3.

AGFM measurements were carried out with the magnetic field applied parallel to the NWs to obtain the DCD and IRM magnetization curves using an alternating gradient field magnetometer from Lakeshore®. Section 3.2.2 illustrates how these curves are measured. The sample size was 2 x 2 mm^2 and the measurements were done at room temperature. The value of the interaction field, IF can be obtained from IRM and DCD remanence curves using the following formula [Martinez 2012, Galvan 2014],

$$\mathrm{IF} = H_{int} = 2\,(H_r^{0.5} - H_d^0) \qquad (6.1)$$

where $H_r^{0.5}$ is the field value at which normalized IRM curve is equal to 0.5 and H_d^0 is the field value at which the normalized DCD curve is zero.

6.3 Results and discussion

6.3.1 SEM characterization of NWs

After dissolving the PC membranes as described in the experimental section the released NWs from low and medium packing density arrays have been shown in Figure 6.1a and Figure 6.1b, respectively. A smooth surface where all the nanowire tips are close to the surface on one side, allowing the microscopy analyses, was observed for low and high density NWs and is shown in Figure 6.1c and Figure 6.1d. The high aspect ratio NWs presented in this study have a mean length (*L*) of around 4 μm with a standard deviation of ± 0.1 μm and diameter with a standard deviation of σ_D = ± 5 nm measured using SEM.

6.3.1 AGFM measurements

The start of IRM curves measurement is indicated with a solid arrow whereas the start of the DCD curves with a dotted arrow (Figure 6.2a and Figure 6.2b). Visual observation of the width between the dotted lines to indicate $H_r^{0.5}$ and H_d^0 shows that IF value is more in medium *P* samples is. Using equation (6.1), the interaction

field values found for $Co_{55}Fe_{45}$ samples of low packing density was 27 Oe and for medium packing density it turned out to be 340 Oe.

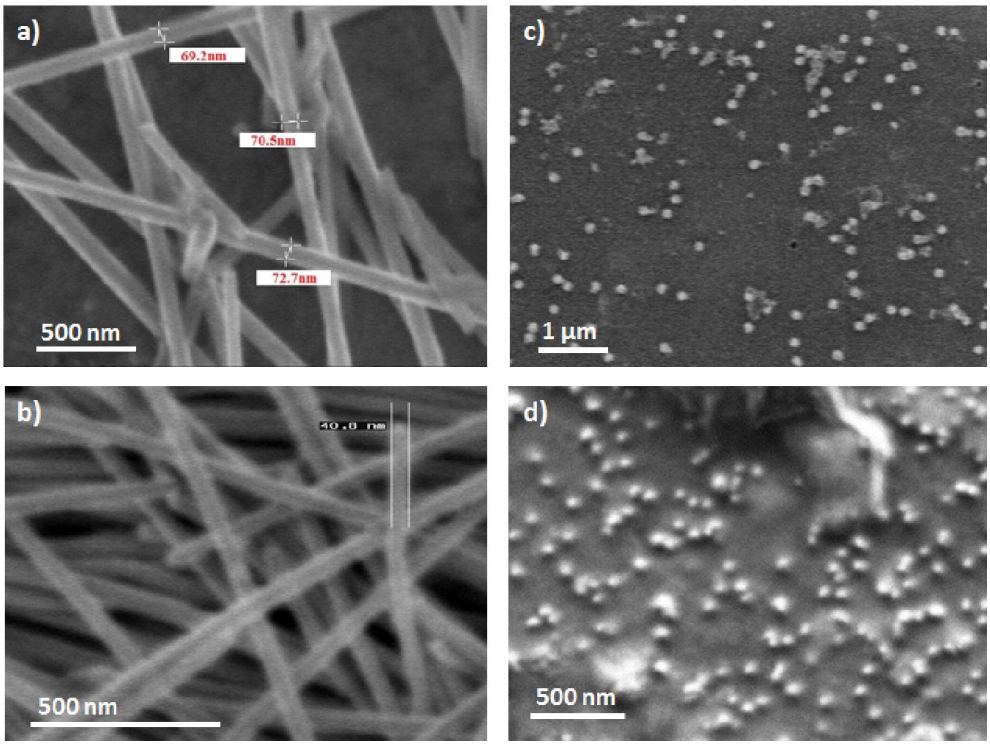

Figure 6.1: SEM micrographs of the CoFe NWs released from the templates of low packing density (*P* ~ 0.2% and *D* = 70 nm) (a) and medium packing density (*P* ~ 3% and *D* = 40 nm) (b). The corresponding SEM micrographs of the sample surface after removal of the cathode, on the low density (c) and medium packing density (d) NWs embedded in the PC templates.

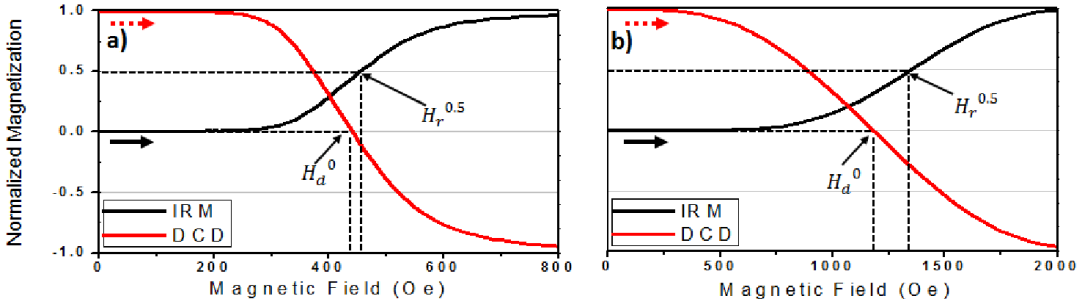

Figure 6.2: Normalized IRM and DCD remanence curves where the field value at which the normalized IRM curve is equal to 0.5, $H_r^{0.5}$, and the field value at which the DCD curve is zero, H_d^0, are indicated. It can be seen that for (a) low density NWs (P ~ 0.4% and *D* = 70 nm) the interaction field is very small (left) whereas for (b) medium density NWs (P ~ 3% and *D* = 40 nm) it is larger (right).

6.3.2 MFM interaction field in the low packing density array

It has been shown in the section 2.9.2 that the effects of inter particle magnetic interactions have been measured using the hysteresis curve of a single particle or few coupled particles in the dense arrays [Sorop 2003, Yuan 2008, Chen 2012b]. In the present study, the low packing fraction magnetic NWs have been chosen to study the dipolar interaction field and its dependence on the distance from nearest neighbors. The first sample analyzed corresponds to $Co_{55}Fe_{45}$ NWs with a diameter of 70 nm and a packing fraction of 0.2%. The NWs have large aspect ratio; they have 100% remanence, as seen from the DCD remanence curves, and reverse their magnetization via irreversible jumps. Before commencing the MFM experiments, the NWs arrays were magnetically saturated along their axis (*+Oz*) under a magnetic field of H = + 2 kOe while the magnetization of the MFM probe tip is in the opposite direction (*-Oz*). This resulted in attractive bright contrast for the NW on the MFM phase images (Figure 6.3a). Then, the magnetic field was applied in the direction of the magnetization of the probe (*-Oz*) to switch the magnetization of the NWs.

This procedure was continued with incremental magnetic field steps of 10 Oe until the field was sufficient to switch the first wire from white contrast to black, as shown in Figure 6.3b. This field is the measured coercivity where the NW switches from the parallel to the antiparallel configuration with respect to its neighbors, H_{c1}, and in this case, H_{c1}= -230 Oe. Once the first wire has switched, an increasing positive magnetic field in (*+Oz*) is applied to switch the same wire back to bright contrast, which in this sample, took place at +330 Oe and can be denoted by H_{c2} (Figure 6.3c). The corresponding schematic hysteresis curve is presented as well (Figure 6.3d) indicating the interaction field of the wire switching from white contrast to black (IF_{wb}) and vice versa. Additionally, in all the measurements, the inter-wire distance to the nearest neighbor was determined from the up and down peaks of the graph shown in Figure 6.3e, in the present case, I_{D} = 350 nm.

The quantification of IF from these measurements was done as follows. First, in the absence of an interaction field, the hysteresis loop of the first wire to switch should

be symmetrical with $H_{c1} = -H_{c2}$. In the presence of an interaction field, the nanowire is subjected to an additional magnetic field, which causes the hysteresis loop to shift along the field axis with $|H_{c1}| \neq |H_{c2}|$.

The field shift produced by the interaction field on the hysteresis loop of the first wire to switch, follows from the measured values of H_{c1} and H_{c2}, in particular:

$$IF = H_{int} = \frac{H_{c1} - H_{c2}}{2} \qquad (6.2)$$

From the above equation it can be shown that the interaction field of the wire (Figure 6.3e) was H_{int} = - 50 Oe. The negative sign implies that the interaction field is antiferromagnetic.

From a mean field perspective, the interaction field can be expressed as $H_{int} = \alpha m$, where $m = M(H)/Ms$, is the normalized magnetization and Ms is the saturation magnetization. From this expression it follows that by measuring the hysteresis loop of the first NW that switches, we probe the interaction field when the system leaves and re-enters the saturated state, this is, when m≈1. So the shift along the field axis of the hysteresis loop of the first switched NW corresponds to the maximum value of the interaction field and $H_{int} = \alpha$.

A very attractive feature of MFM is its ability to perform local analysis at the nanoscale. The 2D arrays of randomly distributed NWs considered in the present study are interesting since different scan areas are likely to provide different local environments where both, the inter-wire distance and the interaction field could vary significantly. In order to analyze the local environment dependence of the interaction field, similar measurements over 10 μm^2 scan areas were done at different places on the same sample and in each case, H_{c1}, H_{c2} and the inter-wire distance was noted.

The results obtained from five different scanned areas are presented in Table 6.1. The interaction field decreases at larger inter-wire distances. The largest value of the interaction field for this sample was - 50 Oe for I_D =350 nm in area A and a minimum of - 15 Oe was measured for I_D =650 nm in area E. In all cases the interaction field is antiferromagnetic. The average value of the interaction field is - 30 Oe with a standard deviation of 13.22 Oe. The average inter-wire distance is

520 nm with a standard deviation of 120.4 nm.

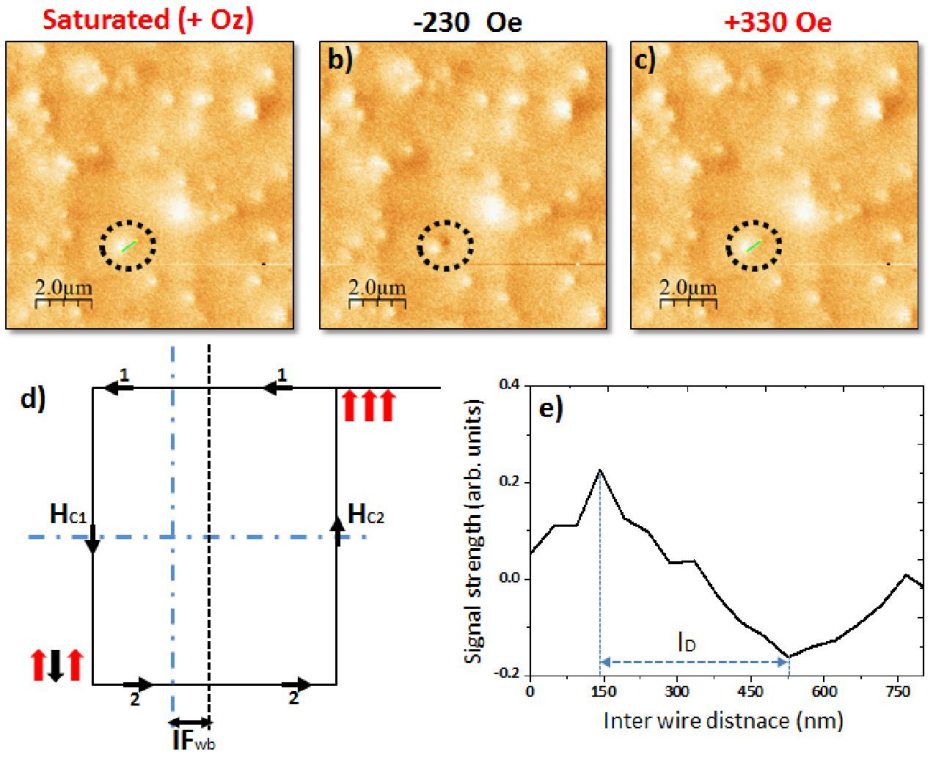

Figure 6.3: 10 x 10 µm^2 MFM images of the CoFe NW arrays (*P* ~ 0.2% and *D* = 70 nm) in saturated state (a), when one of the wire has been switched from up to own magnetization state at a field of -230 Oe (b), the same wire switched back by applying +330 Oe field (c), the schematic hysteresis cycle of this wire (d) and cross section showing the inter-wire distance of the switched wire with its nearest neighbor

This low-density array of NWs presents a weak average interaction field of ~30 Oe. From the results one can also appreciate the resolution of MFM since as seen in Table 6-1, changes as small as 10 Oe in the interaction field are detected. In this case, the stray field of the MFM tip is not expected to play any role in this type of measurements since these are done in the remanent states. Indeed, during the MFM scans, the external field is switched off and the tip height is fixed at a distance of 60 nm from the sample. Even if the tip is always magnetized in the negative (*-Oz*) direction, it will have no effect on the measured coercive fields of the first switched NW, regardless of it's initial magnetization state.

In order to confirm this argument, scans were performed on the same scan area with the tip magnetized in the negative direction (*-Oz*) and with the sample initially saturated in the positive (*+Oz*) direction [Figure 6.4a)], and negative (*-Oz*) direction

(Figure 6.4d). This resulted in an attractive white contrast and a repulsive black contrast for the NW on the MFM phase images, as seen in Figure 6.4 a) and d). Scanning the same area ensures that the inter-wire distance is the constant (l_D ~ 650 nm). The switching events occurred at ± 230 Oe (Figure 6.4b and Figure 6.4e) and ± 260 Oe (Figure 6.4c and Figure 6.4f) in both the cases. From equation (1), it follows that both measurements yield the same value of the interaction field (-15 Oe). Thus, confirming that the tip's stray field has no influence on the switching of individual NWs [Jaafar 2008].

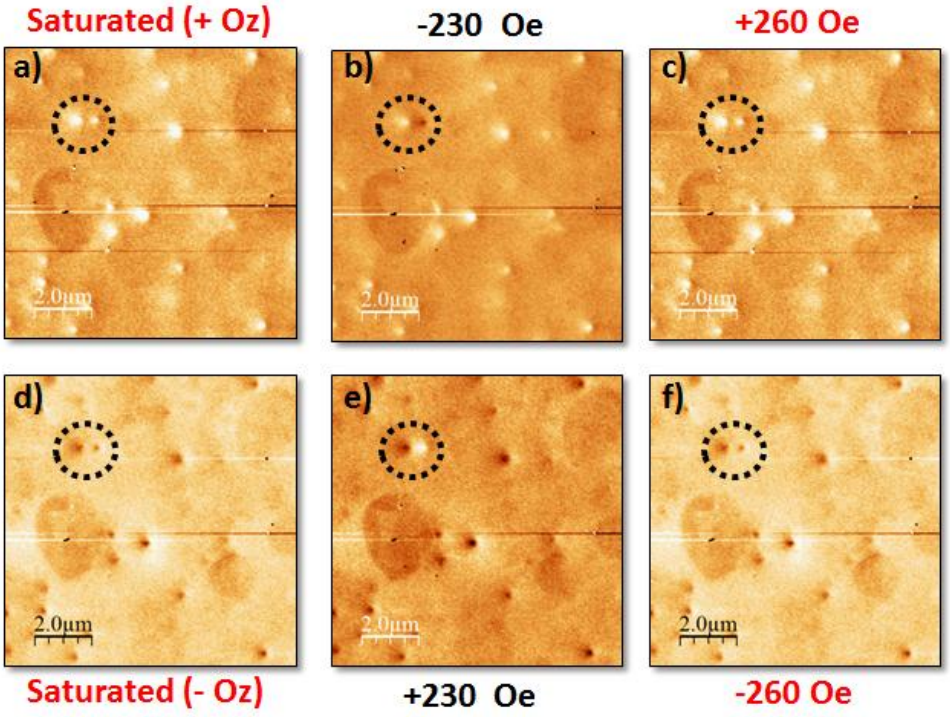

Figure 6.4: 10 x10 µm^2 MFM images of the same area of the CoFe NW array (P ~ 0.2% and D = 70 nm). Top: up state with (a) saturated state, (b) when one of the wire has been switched from up to down magnetization state, (c) when the same wire switched. Down: down state with (d) saturated state, (e) when one wire switched from down saturation to up and (e) when the same wire switches back to down.

Now, to be more precise to get the average values of IF, additional measurements were done scanning different areas of the sample with the NWs initially saturated in the negative direction/black contrast (-*Oz*), the results are presented in the Table 6.1. Once again, very similar hysteresis curves of individual NWs were obtained

with a very low interaction field. As seen from the values of H_{c1} and H_{c2}, the field required to switch a wire from parallel to antiparallel (H_{c1}) is always smaller than the field needed to switch the magnetization from antiparallel to parallel (H_{c2}), consistent with a dipolar antiferromagnetic interaction field. The largest value was -45 Oe for I_D = 400 nm while the lowest value was 0 Oe for I_D = 1000 nm.

Table 6-1: Switching fields H_{c1} and H_{c2}, interaction fields *IF* and nearest neighbor inter-wire distance I_D measured on different areas of the CoFe NW array with P ~ 0.2% and D = 70 nm. Two set of measurements. Upper part of the table represent start of the switching from up "black saturation" and lower part of the table from down " white saturation" states.

Scanned area	$\|H_{c1}\|$ (Oe) (White to black)	$\|H_{c2}\|$ (Oe) (Black to white)	IF_{wb} (Oe)	I_D (nm)
A	230	330	-50	350
B	160	230	-35	450
C	280	330	-25	550
D	210	260	-25	600
E	230	260	-15	650
Scanned area	$\|H_{c1}\|$ (Oe) (Black to white)	$\|H_{c2}\|$ (Oe) (White to black)	IF_{bw} (Oe)	I_D (nm)
A	260	350	- 45	400
B	330	400	-35	500
C	210	260	-25	600
D	230	260	-15	650
E	230	230	0	1000

The average value of the interaction field for the five measurements done with the sample initially saturated in the negative (*-Oz*) direction is -24 Oe and a standard deviation of 17.5. The average inter-wire distance is 630 nm, with a standard deviation of 228. This value is in good agreement with the one found when the sample initially saturated in the positive (*+Oz*) direction, which was -30 Oe.

As mentioned before, since there is no difference on the value of the interaction field measured from either, positive or negative, initial saturation state, both sets of data can be used to determine the average and standard deviation of the interaction field and the inter-wire distance. From the data given in Tables 6.1, the average value of the interaction field is - 27 Oe with a standard deviation of 14.9, while the average inter-wire distance is 575 nm, with a standard deviation of 181.4. These values are discussed in more detail in the following sections.

6.3.3 Interaction field in intermediate density NWs

The second sample considered is an array of $Co_{55}Fe_{45}$ NWs with a diameter of 40 nm and packing fraction of 3%. As the NWs density is higher and the diameter is smaller in this sample, 5 x 5 μm^2 areas were scanned in order to have a better resolution. If the images are taken on larger scan areas than 5 x 5 μm^2, identification of individual NWs is very difficult. For this sample, the measurements have been carried out always with the tip and the sample initially saturated along the (*-Oz*) direction. This resulted in black contrast for the NW on the MFM phase images, as seen in Figure 6.5a).

The magnetic field was then applied in the direction opposite to the magnetization of the sample (*+Oz*) to switch the magnetization of the NWs. The switching field H_{c1} of the first wire was +230 Oe (Figure 6.5b), whereas to switch the same wire back to its initial state a quite higher field H_{c2} = - 900 Oe (Figure 6.5c) was needed. The switched wire has been encircled. Using equation (6.1), the calculated interaction field is - 335 Oe. The corresponding topography image is presented in Figure 6.5d. Comparing the topography image with the magnetic image, it is clear that the switching event happened for a NW that is part of a group of several wires where the local packing density was quite elevated.

Contrary to the low packing fraction sample analyzed in the previous section, in this sample there is more than one neighbor influencing the reversal of the first wire to switch. In order to take into account with more accuracy the influence of nearest neighbors, instead of the simple arithmetic mean, the geometric mean of the I_D was calculated using the relation

$$^1/_{I_D} = {}^1/_N \sum_{i=1}^{N} {}^1/_{di} \qquad (6.3)$$

where d_i represents the distance of the switched wire with its i-th neighbor and N is the number of neighbors. It has been shown above that the neighboring wires at a distances more than 600 nm do not influence the magnetization switching of the wire under study (Table 6.1). Therefore the average inter-wire distance was calculated only for the neighbors that are not far than 600 nm. In addition, as the NWs are randomly distributed so this I_D is not the statistical average of the distance of the nearest neighbors. The calculated average inter-wire distance I_D of this area for the nearest neighbors was ~243 nm and from one of the nearest neighbors is shown in Figure 6.5e.

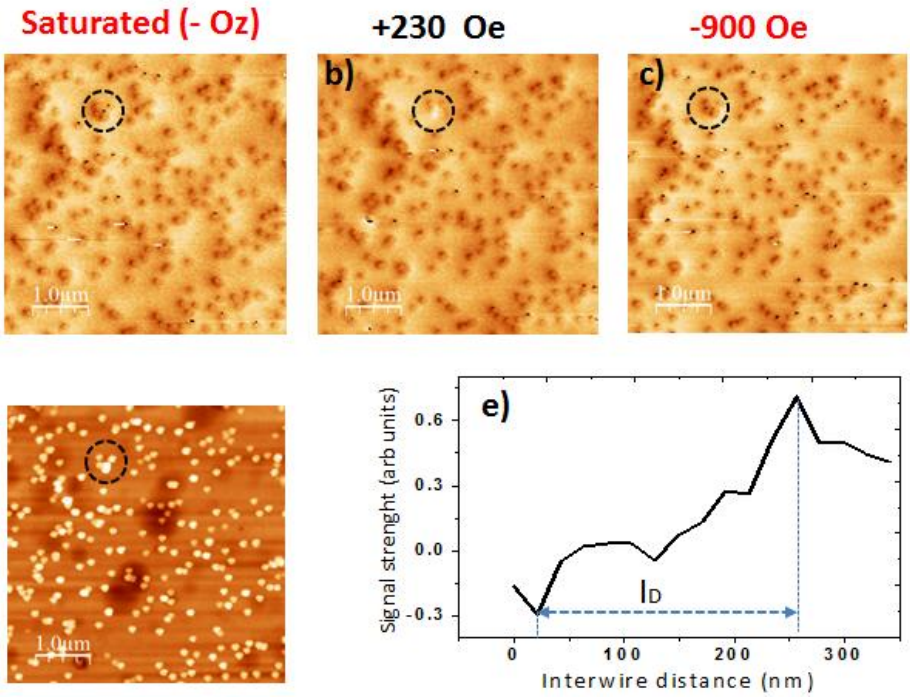

Figure 6.5: 5 x 5 µm^2 MFM images of the CoFe NW arrays (P ~ 3% and D = 40 nm) in saturated state (a), when one of the wire has been switched from down to up magnetization state at a field of + 230 Oe (b), the same wire switched back by applying - 900 Oe field (c), the corresponding topography (the height scale z ranges from - 77 to 113 nm) and (d) cross section showing the inter-wire distance of the switched wire with its nearest neighbor which is 230 nm.

Measurements performed on three different areas in this medium density sample yielded the following values for the interaction field and the inter-wire distance: -300 Oe for I_D = 260 nm, -330 Oe for I_D = 243 nm and -370 Oe for I_D = 200 nm. To

calculate I_D, only the nearest neighbors (distance below 600 nm from the wire under study) were always taken into account. As expected, in all cases the interaction is antiferromagnetic and the value of the interaction field decreases as the inter-wire distance increases. From these values, the average interaction field is -333 Oe (standard deviation 35.11) with an average inter-wire distance of 234 nm (standard deviation 30.9). Comparing with the results obtained in the previous section for the low packing fraction NW array, a substantial increase of the interaction field is observed. Indeed, the interaction field increases from -27 to -333 Oe. This is a consequence of the increasing NW density and thus the reduced inter-wire distance, which decreases from 575 to 234 nm.

6.3.4 Micromagnetic simulations of the interaction field

In order to complement the results obtained by MFM, model micromagnetic simulations have been performed using NMAG [Fischbacher 2007], and these results are compared to the experimental ones. The dimensions and magnetic parameters chosen during calculations are close to the experimental ones. Specifically, the wire length is fixed to $L = 2$ µm while the diameter is fixed to $D =$ 40 nm and 70 nm; the magnetization at saturation, $M_s = 1.9\times10^3$ emu.cm^{-3}, and the exchange stiffness, $A = 1.2\times10^3$ erg/cm, which are the bulk values for the $Co_{55}Fe_{45}$ alloy [Maclaren 1999, Liu 2008]. Determination of the interaction field from micromagnetic simulations is quite straight- forward. Indeed, a first magnetization curve is calculated along the revolution axis of an isolated NW. Then, N neighboring (and interacting) NWs are placed at a distance I_D from the initial NW and its magnetization curve is recalculated. The interaction field is calculated from the field shift observed between both magnetization curves. This is illustrated in Figure 6.6a, where the dashed line represents switching of isolated 70 nm diameter NW and the continuous line corresponds to the switching in presence of one additional identical NW placed at a distance $I_D =$ 90 nm.

Figure 6.6b presents the variation of the interaction field as function of the inter-wire distance I_D for two different NW diameters (40 nm and 70 nm). For the simulations, two geometrical arrangements have been chosen. The first one

corresponds to a row of three interacting NWs, while the second one corresponds to a hexagonal array of 7 NWs.In both cases the interaction field is determined for the central NW. The three-wire system is used to simulate the sample with a low packing density, whereas the 7 wires simulates the medium density sample.

The results clearly confirm that the interaction field increases exponentially when I_D decreases, from values around below 50 Oe when I_D is around 500 nm to values in the order of 500 Oe when I_D is reduced to 50-80 nm. Furthermore, it is interesting to note that these values are of the same order of magnitude than those found experimentally (27 Oe for I_D around 570 nm and 330 Oe for I_D around 200 nm). Finally, it can be seen that the inter-wire distance (I_D) for which the interaction field is close to zero is diameter dependent [Schlorb 2010]. This means that the samples with similar interwire distance will have different IF depending upon the diameter of the NWs in an array.

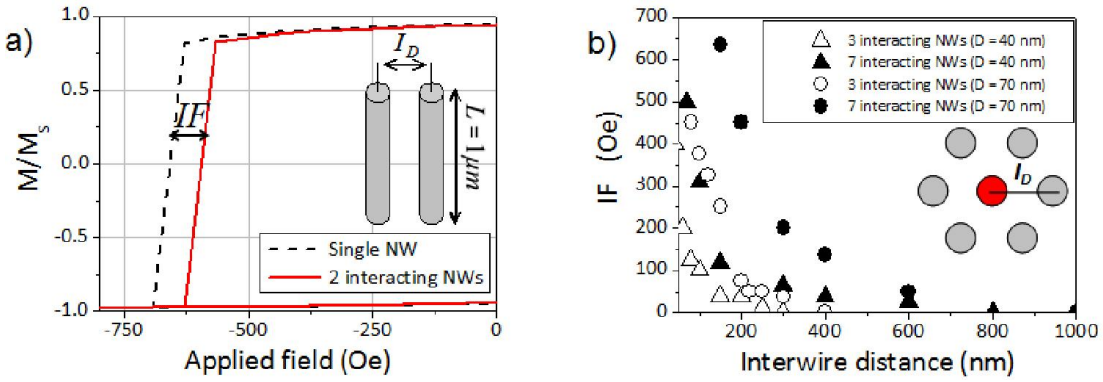

Figure 6.6: a) Magnetization curve calculated on an isolated 70 nm NW (dashed line) and on the same NW in presence of one neighbor NW. The difference between the coercivities of two cycles gives access to the IF. b) Calculated IF of a NW surrounded either by 2 neighboring NWs (open symbols) or 6 neighboring NWs (closed symbols). These calculations have been performed for two different diameters: 40 nm (triangles) and 70 nm (circles); lines are a guide for the eyes.

The results presented show that the interaction field in 2D arrays of parallel NWs is antiferromagnetic and causes the coercive fields of individual wires to shift in a way that less field is required to switch a single wire from parallel to antiparallel and larger fields are needed to switch the wire from antiparallel to parallel. Moreover, both the experimental results and the simulations show that the strength of the

interaction field decreases with an increase in the inter-wire distance.

As mentioned previously, the interest in the first wire to switch is that we probe the effects of the interaction field at saturation where $m = M(H)/Ms = 1$. This allows to relate the measured value of the interaction field with the mean field interaction field coefficient, α, commonly used to express the magnetization dependent interaction field as $H_{int} = \alpha m$.

In this study these measurements have been done by MF on the same samples (CoFe NW arrays of D = 70 nm and D = 40 nm for P ~ 0.2% and P ~ 3% respectively) but on individual nanowires. The interaction field values measured by magnetometry in the low and moderate packing fraction samples were - 27 and - 340 Oe, respectively. These values are in very good agreement with the average values obtained by MFM on different NWs, namely - 27 (standard deviation ~15Oe) and 334 (standard deviation ~ 35Oe). This agreement between the macroscopic measurement and the average obtained over a given number of local measurements is not surprising. Considering the values of the interaction field measured in the low packing fraction sample, given in Tables 6-1, one can see that, for 10 measurements, the lowest/highest interaction field values range from 0 to - 50 Oe, respectively. These values are a consequence of the variation of the local environment of the characterized nanowires.

Since the NWs in PC membranes have a random distribution, when a 10 x 10 μm^2 area is scanned very different local environments are found in each scanned area. Nevertheless, the values of the interaction field averaged on different measurements are in good agreement with the macroscopic values. The agreement found between the average of the interaction field values measured by MFM and the macroscopic measurements done using IRM and DCD remanence curves provide further evidence that these values are correct.

Regarding the interpretation of the interaction field coefficient, a previous mean-field study showed that the interaction field measured from magnetometry using Eq. (6.1) corresponds to the component along the wire axis of the magnetization dependent interaction field, which for very tall nanowires is given by $\alpha = 2\pi M_s P$ [Martinez 2013]. Then, the average value of the interaction field

determined from MFM physically corresponds to this quantity. Figure 6.7 compares the interaction field for both samples (P = 3 and 0.2%) determined from the individual values of the interaction field and inter-wire distances determined by MFM (black circles), the average interaction field as a function of the average inter-wire distance, obtained from AGFM measurements (crossed square), the theoretical interaction field, $\alpha = 2\pi M_s P$, with M_s = 1900 emu/cm3, (horizontal dotted lines) and the experimental value of the interaction field determined from the IRM/DCD remanence curves (horizontal dashed lines). The lines simply represent the expected values and are not the exact description of IF dependence on I_D.

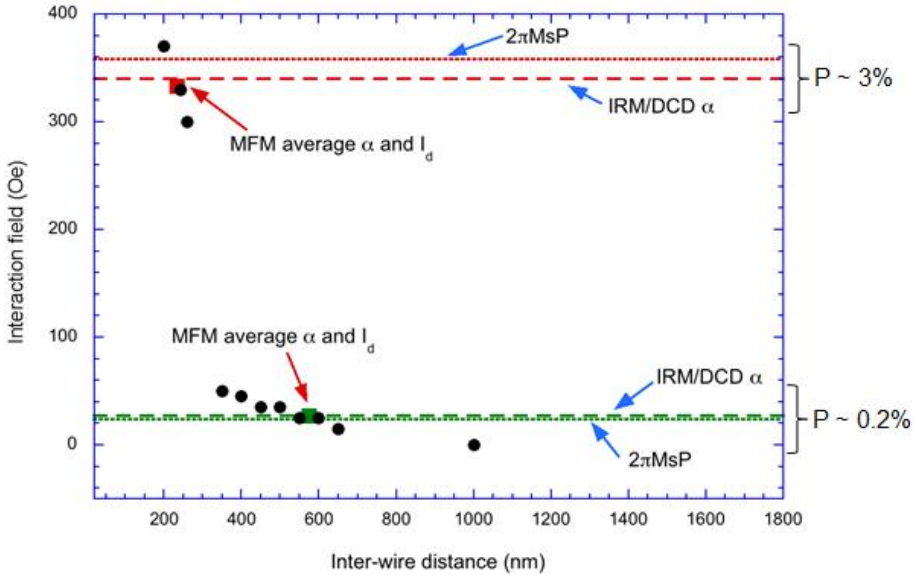

Figure 6.7: Interaction field for both samples (P = 3 and 0.2%) determined from the individual values of the interaction field and inter-wire distances determined by MFM (black circles), the average of these measurements (crossed square), the theoretical value, $\alpha = 2\pi M_s P$, (horizontal dotted lines) and the experimental value determined from the IRM/DCD remanence curves (horizontal dashed lines).

As seen from these results, the individual MFM measurements show a variation that reflects the dependence of the interaction field with the inter-wire distance, as confirmed by the results obtained from micromagnetic simulations. On the other hand, the average interaction field and inter-wire distance, of both samples, derived from the MFM measurements are very consistent with the macroscopic average values obtained experimentally as well as theoretically.

From these results it follows that the interaction field determined from MFM

corresponds to the component along the NW axis of the magnetization dependent interaction field. Furthermore, these results show that MFM is a powerful and versatile tool capable of providing the value of the interaction field at the micro/nanoscale as well as those observed macroscopically. This methodology provides another experimental approach to quantify the dipolar interaction field, which is applicable to other systems as long as it is possible to measure the field shift of the first particle to switch.

6.4 Conclusion

An experimental methodology for the quantification of the dipolar interaction field based on MFM has been developed and tested using two-dimensional arrays of NWs. This method allows the measurement of the interaction field on individual NWs. It has been shown that the interaction field can be determined by MFM by measuring the coercive field shift in the minor loop of the first wire to switch, and this value corresponds to the axial component of the magnetization dependent interaction field. The technique has a good resolution, capable of detecting variations of 10 Oe in the interaction field strength. MFM provides detailed information of the local environment and, as shown here, the local dependence on the inter-wire distance, which cannot be done by standard magnetometry techniques. The average values of the interaction field determined from MFM have been validated by the good agreement found when comparing with the results derived from the macroscopic value of the interaction field determined from magnetometry, micromagnetic simulations and the mean-field model.

Chapter 7
Conclusions and perspectives

MFM has been used to characterize the low density and medium density arrays of magnetic NWs and NTs manufactured by electrodeposition in nanoporous PC membranes. First the AFM equipment modified with external electromagnets to allow "*in situ*" and "*in field*" MFM analyses. The optimal MFM working parameters, in particular the suitability of various commercially available cantilevers for various samples, were studied.

The the magnetization reversal process in arrays of various ferromagnetic NWs such as Ni, $Ni_{80}Fe_{20}$ and $Co_{55}Fe_{45}$ was systematically investigated by AGFM and *in situ* MFM. The NWs had high aspect ratio (diameter ranging from 40-100 nm for length ~ 4 μm) and negligible magnetocrystalline anisotropy, so they displayed bistable magnetic behavior. By analyzing the numbers of NWs with magnetization up and down, local magnetization curves were obtained which agreed well with bulk magnetization measurements from AGFM. The images taken under continuous magnetic field and in the remanent state were compared and found to be identical demonstrating that for these low density arrays the remanent state is identical to the *in field* state due to the weak dipolar interaction.

The influence of the diameter on the magnetization reversal and the SFD was studied. An increase of the SFD width, δ_{SFD} , with decreasing diameter was observed and was qualitatively explained by considering the size distribution of the template nanopores. This demonstrates that the control of NWs diameter is critical for the use of very small diameter NWs in practical applications. Narrower SFD

widths (δ_{SFD}) were observed in the low packing density samples compared to the ones generally obtained for densely packed NW arrays in AAO membranes. The enhanced SFD in high density NW arrays is thus clearly from the increase in packing density i.e. reduced interwire distances.

Then a comparative MFM and FORC study was performed on arrays of Ni NWs with varying packing density. Analysis of the FORC measurements provided solid information of the magnetic interactions and coercive field distribution in magnetic entities. Besides extracting the intrinsic SFD of magnetic particles using MFM the contribution of the dipolar interactions in the total SFD has been evaluated by employing FORC. It has been shown that the intrinsic SFD represents only a fraction of the total non-intrinsic contributions (dipolar interactions) in the high packing density NWs.

Moreover, when comparing the influence of geometry on magnetic behavior of NWs and NTs it has been emphasized that coupling MFM with bulk magnetometry techniques provides in depth information on the individual and global behavior of magnetic nanostructures. Smaller SFD widths and thus lower dipolar interactions were observed in NT arrays compared to NW arrays. The precise control over the inside cavity by modifying the wall thickness opens the possibility of getting negligible interaction fields in NT arrays which is interesting for applications where this parameter needs to be minimized. This shows that high density NTs arrays with negligible SFD and interaction distribution can be achieved.

MFM has been used to extract quantitatively the interaction field by observing the switching of single NWs. Similar values of IF have been obtained with IRM and DCD remanence curves to validate the MFM results on the high remanence arrays of the magnetic NWs. It has been shown that the methodology of employing MFM to assess the IF at nanoscale is a unique way to have information on interaction fields of single magnetic particles which is very useful for magnetic logic devices and patterned magnetic media. The dependence of the IF on interwire distance has been studied and shown that the IF increases exponentially for I_D less than four

times the diameter of the nanostructure and vanishes at I_D ~ 10 times the diameter. A simple and straight forward approach has been used to evaluate the influence of the tip's stray field on the *in situ* MFM measurements.

In future, NW and NTs are expected to be used in various applications such as nanobarcodes, sensors and patterned media. This study demonstrates that controlling geometric parameters such as diameter, length, tube thickness and pitch in NWs and NTs is critical to tune the magnetic properties of high density magnetic structures. Furthermore, it has also been shown that MFM is a valuable tool to investigate the magnetic behavior of such nanostructures.

Compared with AGFM where sensitivity is a limit, MFM has the capacity to map the stray field emanating from single isolated magnetic entities which makes this instrument very useful to study the magnetic properties of the single-isolated magnetic particles (see Figure 1 and 2 in the annex). MFM should also allow the magnetic characterization of isolated NWs and NTs released from the templates to get information about their magnetic configuration (Figure 3 and 4 in the annex).

The mystery of understanding the field value emanating from the magnetic tip which may influence the switching process can also be solved. We have devised a simple way to measure the influence of the tip stray field (chapter 6). The procedure can be used as a reference to evaluate the influence of tips stray fields of the other commercially available tips at a desired lift scan height.

IF from the dense arrays of magnetic nanowires can be calculated using the procedure mentioned in chapter 6. The idea behind this is: staring from the isolated magnetic particles of precisely controlled diameter to measure the SFD and IF, change their pitch and measure interaction fields. By playing with the parameters such as length, diameter and pitch it will be possible to find out the high density magnetic arrays of negligible IF for data storage applications and logic devices. However, for high packing density samples (Figure 5 and 6 in the annex) just by measuring the I_D from MFM images will not be sufficient. Therefore, methods like Voronoi diagrams may be used to analyse the images efficiently. In

addition, recently in certain studies the NTs have shown low IF in bulk and MFM measurements, their use to get a high density non interacting array of controlled diameter and pitch will be fruitful.

References

Adeyeye, A. O., S. Goolaup, N. Singh, W. Jun, C. C. Wang, S. Jain, and D. Tripathy, IEEE transaction on magnetic, 44, 7 (2008)

Aharoni A. and S. Shritkman, Phys. Review, 109, 1522 (1958)

Aigouy L.,Y. De Wilde, and C. Frétigny. Les nouvelles microscopies: à la découverte du nanomonde. Belin, (2006)

Alberto P. G, Principles of Nanomagnetism, Springer-Verlag, Berlin (2009)

Albrecht T. T., J. Schotter, C. A, Kästle, N. Emley, T. Shibauchi, L. Krusin-Elbaum, K. Guarini, C.T. Black, M.T. Tuominen and T. P. Russell, Science, 290, 2126 (2000)

Aravamudhan S., J. Singleton, P. A. Goddard and S. Bhansali, J. Phys. D: Appl. Phys. 42, 115008 (2009)

Aravena D. S., R. M. Corona, D. Goerlitz, K. Nielsch and J. Escrig, J. Magn. Magn. Mater, 346, 171 (2013)

Asenjo A., J. M. Garcia and M.Vazquez, Magnetic Force Microscopy: Recent Res. Devel. Magnetics, 2, 21 (2001)

Asenjo A., M. Jaafar, D. Navas, and M. Vázquez, J. Appl. Phys. 100, 023909 (2006)

ASYMFMHC, http://www.asylumresearch.com/Probe/ASYMFMHC,Asylum, accessed in October (2014)

Aune D., E. Riedel, and B. Thibadeau, Future of intelligent storage, Seagate, (2006)

Bao J., C. Tie, Z. Xu, Q. Zhou, D. Shen, and Q. Ma, Adv. Mater. 13, 21 (2001)

Belle B.D, F. Schedin, N.Pilet, T.V Ashworth, E.W. Hill, P.W. Nutter, H.J Hug, and J.J Miles, J. Appl. Phys. 101, 09F517 (2007)

Belliard L., J. Millat, A. Thiaville, S. Dubois, J.L Duvail and L. Piraux, , J. Magn. Magn. Mater. 190, 1(1998)

Béron F., L. Clime, M. Ciureanu, D. Ménard, R. W Cochrane and A. Yelon , J. Nanoscience and Nanotechnology, 8, 2944, (2008)

Binning, G., Rohrer, H., Gerber, Ch., & Weibel, E. Appl. Phys. Lett, 40, 178 (1981)

Binning, G., Rohrer, H., Gerber, Ch., & Weibel, E. Phys. Rev. Lett, 50, 120 (1983)

Blackblaze: https://www.backblaze.com/blog/farming-hard-drives-2-years-and-1m-later/ accessed December (2014)

Bonnel D. A., Scanning Probe Microscopy and Spectroscopy, Theory, Techniques, and Applications. Wiley-VCH, (2001)

Bouhnik Electromagnet, http://www.bouhnik.com/actualites.html, accessed in July (2014)

Brown W. F., and F.E Luborsky, J. Appl. Phys. 39, 993, (1968)

Cao G., Nanostructures and nanomaterials, Synthesis, Properties, and Applications, Imperial College Press, (2004)

Carignan L.P., C. Lacroix, A. Ouimet, M. Ciureanu, A. Yelon and D. Menard, J. Appl. Phys. 102, 023905 (2007)

Chen A. P., J. Gonzalez and K.Y. Guslienko, J. Magn. Magn. Mater, 324, 3912 (2012a)

Chen Y.H, J. L Duan, H.J Yao, D. Mo, T. Q Liu, T.S Wang, M.D Hou, Y.M Sun and J. Liu, Physica B 441, 1 (2014)

Chen Y.J., T.L. Huang, J. Z. Shi, J. Deng, J. Ding, W.M. Li, S.H. Leong, B.Y. Zong, Hnin Yu Yu Ko, S.B. Hu and J.M. Zhao, J. Magn. Magn. Mater, 324, 264 (2012b)

Cho S.G., B. Yoo, K. H. Kim and J. Kim, IEEE Trans. Magn. 46, 420 (2010)

Choi D., J. Park, S. Kim, D. Gracias, M. Cho, Y. Kim, A. Fung, S. Lee, Y. Chen, S. Khanal, S. Baral, and J.Kim, J. of Nanoscience & Nanotech., 8, 1 (2008)

Coey J. M. D., Magnetism and magnetic materials, Cambridge University Press, New York, (2010)

Coulon A., MFM probes and parameters optimization to characterize magnetic nanowires, Master's thesis, Université Catholique de Louvain, June (2014)

Cullity B. D. and C. D. Graham., Introduction to magnetic materials, IEEE Press. Wiley, (2009)

Darques M., J. Spiegel, J. De la Torre Medina, I. Huynen and L. Piraux , J. Magn. Magn. Mater, 321, 2055 (2009)

Darques M., S. Michote, F. Elhoussine, A. Encinas, J. De la Torre Medina, and L. Piraux, J. Phys. D: Appl. Phys. 39, 5025 (2006)

Daub M., M. Knez, U. Goesele, and K. Nielsch, J. Appl. Phys.101, 09J111 (2007)

Dobrota C. I. and A. Stancu, J. Appl. Phys. 113, 043928 (2013)

Dobrynin A. N., M. T. S. Barthem and D. Givord, Appl. Phys. Lett. 95, 052511 (2009)

Eftekhari, A., Nanostructured Materials in Electrochemistry, Wiley-VCH, (2008)

Encinas A., M. Demand, L. Piraux, I. Huynen, U. Ebels, Phys. Rev. B 63, 104415 (2001)

Encinas A., L. Vila, M Darques, J M George and L Piraux, Nanotechnology, 065705 (2007)

Endo Y., Y. Matsumura, R. Nakatani, and M Yamamoto, J. of Phys, 106, 012006 (2008)

Escrig J., D. Altbir, M. Jaafar, D. Navas, A. Asenjo and M. Vázquez, Phys. Rev. B 75, 184429 (2007a)

Escrig J., P. Landeros, D. Altbir, E.E. Vogel and P. Vargas, J. Magn. Magn. Mater, 308, 233 (2007b)

Favier F., E.C Walter, M. P Zach, T. Benter, and R.M. Penner, Science, 293, 2227 (2001)

Fert A. and L. Piraux., J. Magn. Magn. Mat., 200:338–358, (1999)

Ferain E. and R. Legras. Nucl. Instr. and Meth. in Phys. Res. B, 208:115, (2003)

Ferré R., K. Ounadjela, J. M. George, L. Piraux, and S. Dubois, Phys. Rev. B 56, 14066 (1997)

Feifei T., Mingyun Guan, Yuan Jiang, Jianmin Zhu, Zheng Xu, and Ziling Xue, Adv. Mater. 18, 2161 (2006)

Fischbacher T., M. Franchin, G. Bordignon and H. Fangohr, IEEE Trans. Mag. 43, 2896 (2007)

Fodor P. S., G. M. Tsoi, and L. E. Wenger, J. Appl. Phys. 93, 7438 (2003)

Folk L., M.E Best, P.M Rice, B.D Terris, D.Weller and J.N Chapman, Appl. Phys. Lett. 76, 909 (2000)

Frei E. H., S. Shtrikman, and D. Treves, Phys. Rev., 106, 3 (1957)

Galvan Y. V., J. M. Martınez-Huerta , J. De La Torre Medina,Y. Danlee , L. Piraux and A Encinas, J.Phys.Condens. Matter, 26, 026001(2014)

Garcia J. M., A. Thiavill and J. Millat, J. Magn. Magn. Mater. 249, 163 (2002)

Ghaddar A., F. Gloaguen, J. Gieraltowski, and C. Tannous, Physica B, 406, (2011)

Hamoir G., L Piraux, I Huynen, IEEE Transactions on Magnetics, 49, 4261 (2013)

Han X.F., S. Shamaila, R. Sharif, J.Y. Chen, H.R. Liu,and Dong-Ping Liu, Adv. Mater. 21, 4619 (2009)

Hao L., D. Cox, P. See, J. Gallop and O. Kazakova, *J. Phys. D: Appl. Phys.* 43, 474004 (2010)

Harrison R. J. and J. M. Feinberg, Geochem. Geophys. Geosyst. 9, Q05016 (2008)

Hellwig O., A. Berger, T. Thomson, E. Dobisz, Z. Z. Bandic, H. Yang, D. S. Kercher and E. E. Fullerton, Appl. Phys. Lett. 90, 162516 (2007)

Henry Y., K. Ounadjela, L. Piraux, S. Dubois, J.M. George and J.L Duvail, Eur.Phys. J. B, 20, 35, (2001)

Iglesias-Freire O., M. Jaafar, L. Pérez, O de Abril, M. Vazquez, A. Asenjo, J. Magn. Magn. Mater. 355, 152 (2014)

Imre A., G. Csaba, L. Ji, A. Orlov, G.H. Bernstein, and W. Porod, Science, 311, 205 (2006)

Jaafar M., A. Asenjo, and Manuel Vazquez, IEEE transactions on nanotechnology, 7, 245 (2008)

Jaafar M, J. Gomez-Herrero, A. Gil, P. Ares, M. Vazquez and A. Asenjo, Ultramicroscopy. 109, 693 (2009)

Karim S., and K. Maaz, Mat. Chem. Phys. 130:1103, (2011)

Kawamori M., S. Yagi and M. Matsubara, J. Electrochem. Soc. 158, E79-E83 (2011)

Keithly J. F., The story of electrical and magnetic measurements from 500 B.C. to the 1940s, IEEE Press, Willey, (1999)

Khan H. R., and K. Petrikowskia, Mat. Sci. Eng. C 19, 345 (2002)

Kou X., X. Fan, R. K. Dumas, Q. Lu, Y. Zhang, H. Zhu, X. Zhang, K. Liu and J. Q. Xiao, Adv. Mater. 23, 1393 (2011)

Kyali M. A., and W. M. Saslow, Phys. Rev. B 70, 174404 (2004)

Landeros P., S. Allende, J. Escrig, E. Salcedo, and D. Altbir, Appl. Phys. Lett.90, 102501 (2007)

Lee J., D. Suess, T. Schrefl, K. H. Oh, J. Fidler, J. Magn. Magn. Mater, 310, 2445 (2007)

Lee S.B., D.T. Mitchell, L. Trofin, T.K. Nevanen, H. Soderlund, C.R. Martin, Science, 296, 2198(2002)

Li. J., C. Papadopoulos, and J. M. Xu, Appl. Phys. Lett. 75 367 (1999)

Liu J., F. Wang, J. Zhai and J. Ji, J. Elect. Chem. 642, 103 (2010)

Liu Q., J. Wang, Z. Yan and D. Xue, Phys. Rev. B 72, 144412 (2005)

Liu X., and M. Akimitsu, J. Appl. Phys.103, 07E726 (2008)

Lopez-Lopez J. A., D. Cortés-Ortuno and P. Landeros, J. Magn. Magn. Mater, 324, 2024 (2012)

Maclaren J.M., T.C. Schulthess, W.H Butler, R. Sutton and M. McHenry, J. Appl. Phys.85, 4833 (1999)

Martin C.R.; Kohli, P. Nature Reviews Drug Discovery, 2, 29 (2003)

Martin C. R., and L.A. Baker, Science, 309, 67 (2005)

Martin Y. & Wickramasinghe H. K. Appl. Phys.Lett. 50, 20, 1455 (1987)

Martınez-Huerta J. M., J. De La Torre Medina, L. Piraux and A. Encinas, J. Appl. Phys.111, 08391 (2012)

Martınez-Huerta J. M., J. De La Torre Medina, L. Piraux and A. Encinas, J. Phys, Cond. Matt 25, 226003 (2013)

Medina J. De La Torre, L. Piraux and A. Encinas, App. Phys. Lett. 96, 042504 (2010)

Meeker D. C., Finite Element Method Magnetics (http://www.femm.info), used the package in (2014)

MESP-HM. https://www.brukerafmprobes.com/Product.aspx?ProductID= 3311, accessed in October (2014)

MESP-LM. https://www.brukerafmprobes.com/Product.aspx?ProductID= 3315, accessed in October (2014)

Meyer E., Hug H.J., and Bennewitz R. Scanning Probe Microscopy: The Lab on a Tip. Springer, (2004)

Murray B. J., E. C. Walter, and R. M. Penner, Nano Lett., 4(4), 665 (2004)

Nam B., J. Kim and J.J Hyeon, J. Appl. Phys., 111, 07E347(2012)

Navas D., A. Asenjo, M. Jaafar, K.R. Pirota, M. Hernandez-Velez, R. Sanz, W. Lee, K. Nielsch, F. Batallan M. Vazquez, J. Magn. Magn. Mater, 290, 191 (2005)

Neel L., Compt. Rend, 228,664 (1949)

Nicoleta L., Electrodeposited Nanowires and Their Applications, Intech, Olajnica (2010)

Nielsch K., R.B Wehrspohn, S.F Fischer, H. Kronmiller, J. Kirsehner and U.Gosele, Mater. Res. Soc. Symp. Proc., 9, 636 (2001)

Nielsch K., R. B. Wehrspohn, J. Barthel, J. Kirschner, S. F. Fischer, H. Kronmüller, T. Schweinböck, D. Weiss, U. Gösele, J. Magn. Magn. Mater. 249, 234 (2002)

Nobelprize.org. (1986). The Nobel Prize in Physics Ernst Ruska, Gerd Binnig, Heinrich Rohrer, http://www.nobelprize.org/ nobel_prizes/physics/laureates/1986/, accessed May (2012)

Nysten B., MAPR2631: Analyse et traitement des surfaces solides - scanning probe microscopies. lecture notes, (2013)

Ott F., T. Maurer, G. Chaboussant, Y. Soumare, J.-Y. Piquemal and G. Viau, J. Appl. Phys. 105, 013915 (2009)

Pei W.L., G.W. Qin, Y.P. Ren, S.Li, T. Wang, H. Hasegawa, S. Ishio, and H. Yamane, Acta Materialia,59, 4818 (2011)

Pike C. R, C. A Ross, R.T Scalettar and G. Zimanyi, Phys. Rev. B, 71, 134407 (2005)

Piramanayagam S.N., and Tow C. Chong, Developments in data storage, IEEE Press, Wiley, (2012)

Piraux L., A. Encinas, L. Vila, S. Mátéfi-Tempfli, M. Mátéfi-Tempfli, M. Darques, F. Elhoussine and S. Michotte, J. Nanosci. Nanotechnol. 5, 372 (2005)

Piraux L., V. A. Antohe, F. Abreu Araujo, S. K. Srivastava, M. Hehn, D. Lacour, S. Mangin, and T. Hauet Appl. Phys. Lett.101, 013110 (2012)

Porthun S., Abelmann L., & Lodder C. J. Magn. and Magn. Mater, Vol. 182, No. 1-2, 238 (1998)

PPP-LC-MFMR. http://www.nanoandmore.com/PPP-LCMFMR.html, accessed in October (2014)

Proenca M. P., C. T. Sousa, J. Escrig, J. Ventura, M. Vazquez and J.P Araujo, J. Appl. Phys.113, 093907 (2013)

Richter H.J. et al. IEEE Trans. Magn. 42, 2255 (2006)

Rosa W.O., M. Jaafar, A. Asenjo, and M. Vázquez, J. Appl. Phys. 105, 07C108 (2009)

Rozman K. Z. , D. Pecko, L. Suhodolcan, P. J. McGuiness, S. Kobe, J. Alloy.Comp. 509, 551 (2011)

Rozmann K.Z, Fabian Rhein, Ulrike Wolff and Volker Neu, Acta Materialia 81, 469 (2014)

Ryan M., Platinum Metals Rev., 54, 244 (2010)

Salem M. S., P. Sergelius, R. Zierold, J. M. M. Moreno, D. Gorlitz and K. Nielsch. J. Mater. Chem. 22, 8549 (2012)

Schlorb H., V. Haehnel, M. S. Khatri, A. Srivastav, A. Kumar, L. Schultz, and S. Fahler, Phys. Status Solidi B247, 10, 2364 (2010)

Sharif R., S. Shamaila, M. Ma, L. D. Yao, R. C. Yu, X. F. Han, and M. Khaleeq-ur-Rahman, Appl. Phys. Lett.92, 032505 (2008)

Sharif R., S. Shmaila, F. Shaheen, J.Y Chen, M. Khaleeq-ur-Rahman and K. Hussain, Appl. Phys. Lett.102, 013114 (2013)

Skomski R., H. Zeng, M. Zheng, and D. J. Sellmyer, Phys. Rev. B 62, 3900 (2000)

Sorop T. G., C. Untiedt, F. Luis, M. Kröll, M. Rasa, and L. J. de Jongh, Phys. Rev. B 67, 014402 (2003)

Sorop T. G., K. Nielsch, P. Goring, M. Kroll, W. Blau, R. B. Wehrspohn, U. Gosele and L. J. de Jongh, J. Magn. Magn. Mater. 272, 1656 (2004)

Stoner E. C. and Wohlfarth E. P., Phil. Trans. Roy. Soc. A240:599, (1948)

Sun S.H., C.B. Murray, D. Weller, L. Folks, and A. Moser, Science, 287, 1989 (2000)

Sun L., and Q. Chen, J. Phys. Chem. C 113, 2710 (2009)

Sun L., Y. Hao, C. L. Chien and P. C. Searson, IBM J. Res. and Dev., 49, 1 (2005)

Sui Y.C., R. Skomski, K.D. Sorge, and D.J. Sellmyer, Appl. Phys. Lett.84, 1527 (2004)

Tabasum M. R, F. Zighem, J. De La Torre Medina, L. Piraux, B. Nysten, J. Superconduct. Novel Magn., 26, 1375 (2013a)

Tabasum M. R, F. Zighem, J. De La Torre Medina, A. Encinas, L. Piraux and B. Nysten, J. Appl. Phys., 113, 183908 (2013b)

Tabasum M. R, F. Zighem, JDLT Medina, A Encinas, L Piraux and B Nysten, Nanotechnology 25, 245707 (2014)

Thomas, J.M., E.T Simpson, T. Kasama, R.E Dunin-Borkowski, Acc. Chem. Res, 41, 665 (2008)

Usov N. A., A. Zhukov and J. Gonzalez, J. Magn. Magn. Mater, 316, 255 (2007)

Van Schendel P. J. A., H.J. Hug, B. Stiefel, S. Martin and H.-J. Güntherodt, J. Appl. Phys. 88,435 (2000)

Vazquez M., M. Hernandez-Velez, K. Pirota, A. Asenjo, D. Navas, J. Velazquez, P. Vargas and C. Ramos, Eur. Phys. J. B40, 489 (2004)

Vazquez M., K. Pirota, J. Torrejon, D. Navas and M. Hernandez-Velez, J. Magn. Magn. Mater. 294, 174 (2005)

Wang Q., G. Wang, X. Han, X. Wang and J.G. Hou, J. Phys. Chem. B, 109, 23326 (2005)

Wang S.X. and M.A Taratorin, Magnetic information storage technology, Academic press, San Daigo, CA, (1999)

Wang X. W., G. T. Frei, L. Chen, X. J. Xu, and L. D. Zhang, Electrochem. Solid State Lett. 10, E1-E3, (2007)

Wang T., Y. Wang, Y. Fu, T. Hasegawa, H. Oshima, K. Itoh, K. Nishio, H. Masuda, F. S. Li, H. Saito, and S. Ishio, Nanotechnology, 19, 455703 (2008)

Wang X.W., Z.H Yuan, B.C Fang, Mat. Chem. and Phys. 125, 1 (2011)

Wiesendanger R. Scanning Probe Microscopy and Spectroscopy: Methods and Applications. Cambridge University Press, (1994)

Xu J. and K. Wang, Journal of Wuhan University of Technology-Mater. Sci. Ed., 23, 472 (2008)

Young, R., Ward, J., & Scire, F. The Rev. Sci. Inst, 43, 999 (1972)

Yuan J., W. Pei, T. Hasagawa, T. Washiyaa, H. Saito, S. Ishio, H. Oshima, Ken-ichi Itoh, J. Magn. Magn. Mater, 320, 736 (2008)

Yin H.Q. and W.D Doyle, J. Appl. Phys., 91, 7709, 2002

Zhang X., H. Zhang , T. Wu, Z. Li, Z. Zhang and H. Sun, J. Magn. Magn. Mater, 331, 162 (2013a)

Zhang H.M., X.L Zhang, J. J Zhang, Z. Y Li and H. Y Sun, J. Magn. Magn. Mater. 342, 69 (2013b)

Zhu J.G., X. Zhu, Y. Tang, IEEE Trans. Magn.44, 125–131, (2008).

Annex

Instruments such as SQUID and AGFM are used extensively to study the magnetic behavior of arrays of nanostructures. Like any other technique, they suffer from sensitivity limits. For instance the signals from AGFM, for a very dilute array of magnetic $Ni_{20}Fe_{80}$ NWs (10^6 NWs/cm^2) shown in Figure7.1. In this sort of very low density arrays the signal is too weak to be detected by AGFM.

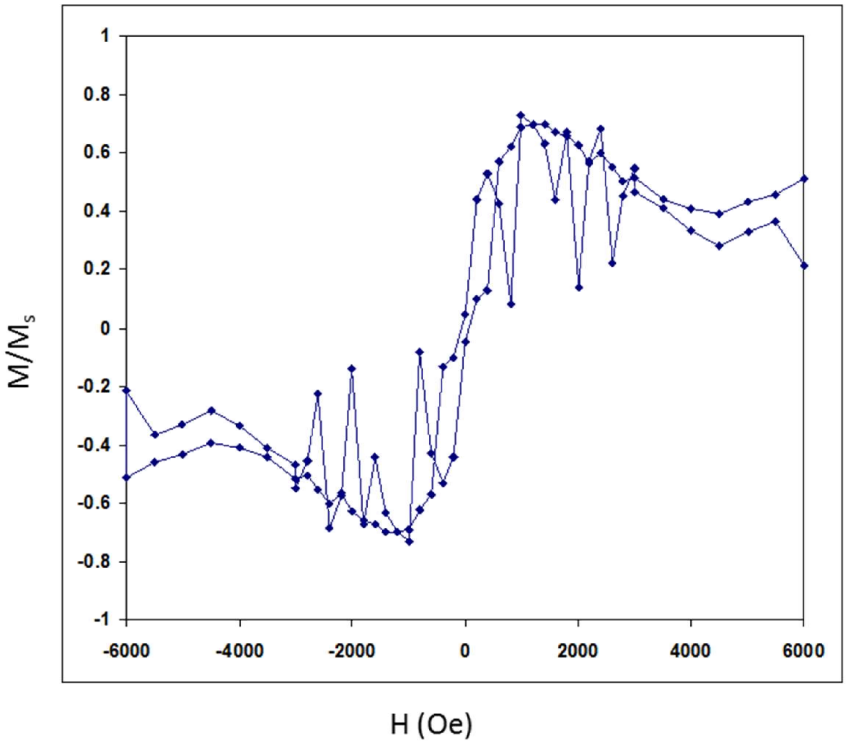

Figure7.1: AGFM signal from a very dilute (10^6 NWs/cm^2) array of 50 nm $Ni_{80}Fe_{20}$ NWs.

On the other hand MFM has the capacity to map the stray field emanating from single isolated magnetic entities which makes this instrument very useful to study the magnetic properties of the single-isolated magnetic wires, dots and nanotubes, see in particular chapter 6. The same sample of very low density $Ni_{80}Fe_{20}$ NWs when scanned with the MFM probe, clear magnetic signal was detected from one wire as shown in Figure 7.2. Although difficult to find a magnetic nano structure of tens of nm in size in an area of some μm^2, using common magnetometry instruments, MFM is a promising tool for their magnetic characterization.

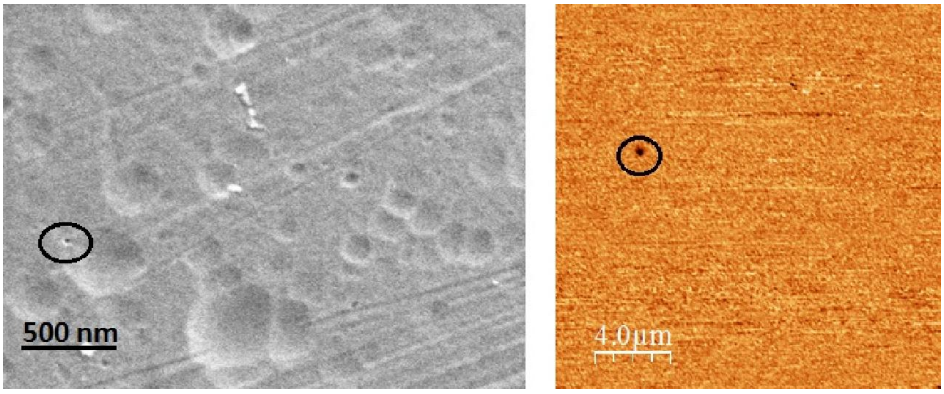

Figure 7.2: SEM image showing pores, encircled, of the very low density membrane (left). MFM signal of a single NW, encircled, in a very dilute (10^6 NWs/cm^2) array of 50 nm $Ni_{80}Fe_{20}$ NWs (right).

An attempt to characterize isolated NWs and NTs released from the templates to get information about the magnetic configuration has been made. Since, magnetic NWs/NTs behave like small magnets, once released from the template they prefer to accumulate making the process of getting the individual and isolated NWs/NTs quite tedious as shown in Figure 3.8 and here in Figure 7.3.

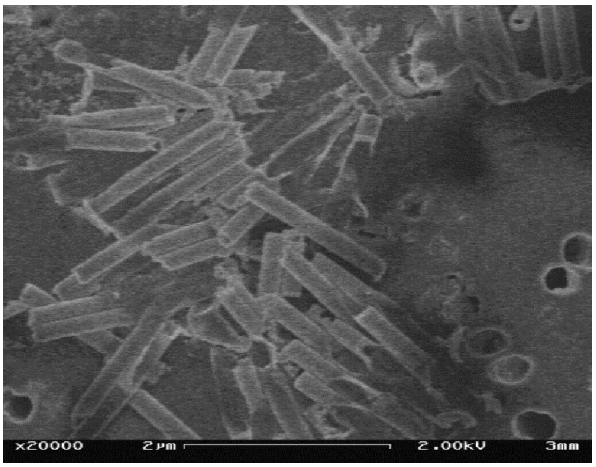

Figure 7.3: Ni NTs of diameter 150 nm released from PC templates.

During the process of membrane dissolution and NWs/NTs release some of them were broken resulting in lengths smaller than originally produced as shown in topography images (Figure 7.4a and Figure 7.4b) for NWs and NTs respectively. The corresponding MFM phase images are presented in Figure 7.4c and Figure 7.4d. One would expect to see the wire and tube as nano magnets with magnetization emitting from one side and returning back to the other as was observed for single

domain magnetic NWs/NTs of diameters less than 80 nm [Belliard 1998]. The wires and the tubes used in this study were 150 nm in diameter which favours the formation of vortex domains and the non-uniformity of the magnetic configuration inside the wires and tubes, especially when they are broken and have aspect ratio < 10, as shown in Figure 4c and 4d. This is evident from these figures that at this diameter, NWs and NTs are not having uniform magnetization throughout their lengths. Simulations done on magnetic NTs of different aspect ratio have already showed that some new form of domain walls, in addition to vortex and transverse branch fashion and horse-saddle walls appeared with decreasing aspect ratio L/R of the tubes [Daub 2007, Chen 2012a, Lopez 2012].

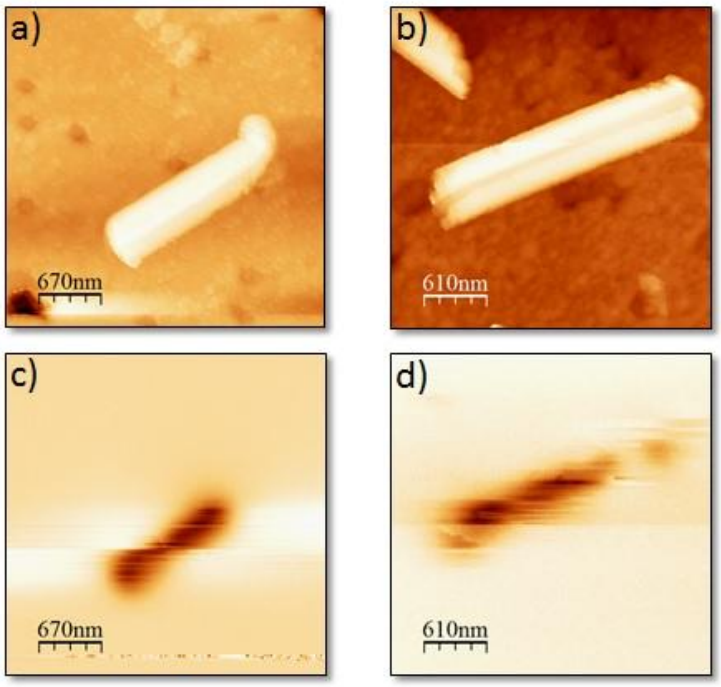

Figure 7.4: Topographical images of 150 nm Ni NWs (a) and NTs (b) respectively. MFM phase images of Ni NWs (c) and NTs (d) respectively. The wire and tube are released from the PC template.

In an attempt to find out the IF of a very high density sample i.e. NWs embedded in AAO templates, the sample surface after removing the cathode has been scanned. The phase image presented below (Figure 7.5-right) indicated no signal which was quite astonishing as AGFM have shown a very nice hysteresis curve from the same sample.

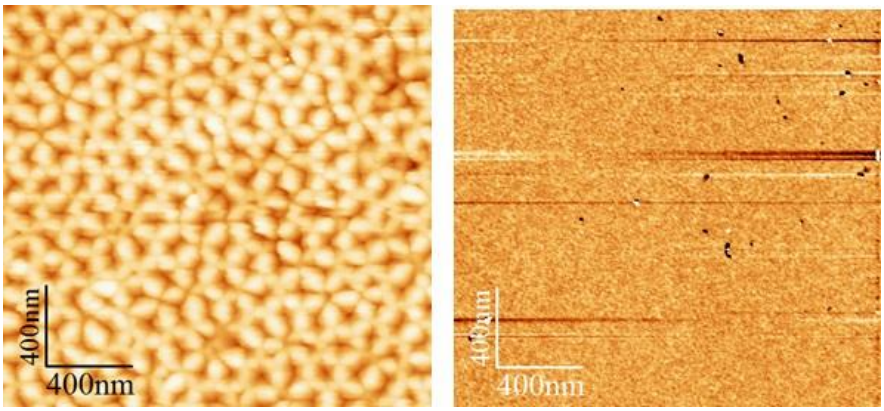

Figure 7.5: Topography of the NiFe NWs of *D* = 50nm embedded in AAO sample after removing the cathode layer (left) and the corresponding phase image (right)

From the topography image (Figure 7.5-left), it can be seen that the hexagonally arranged pores in AAO template are empty at the surface and appear as dark holes. This was further investigated by SEM as shown in Figure 7.6. From Figure 7.5 and Figure 7.6, it is evident that the NWs are deposited several tens of nm. To explain this, it was supposed that the cathode has deposited some nano meters inside the AAO template pores. As MFM can detect the stray fields emanating from the magnetic entities only at a certain distance, this explains why the phase images didn't show any signal. To allow the MFM characterization of such samples, the AAO template should be polished after removal of the cathode and before MFM analysis.

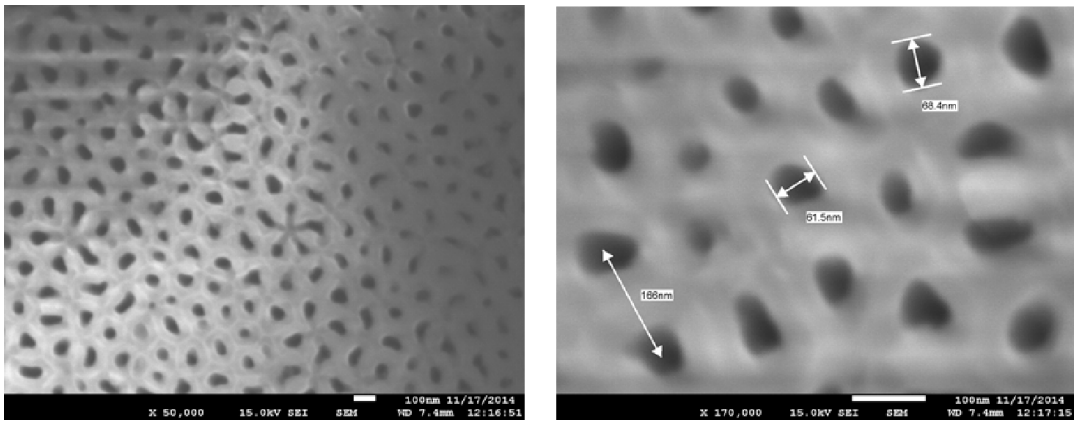

Figure 7.6: Top surface of the AAO template after cathode removal

Matlab code for r_{sd} calculation:

```
% (c) 2015 by Dr. Flavio Miguel ABREU ARAUJO. All rights reserved.
% https://www.flavio.be - abreuaraujo.flavio@gmail.com
function r_sd_vs_aspect_ratio
clc; tic
% Material parameters
A(1) = 0.86e-6; Ms(1) = 484; label{1} = 'Ni'; % Ni
A(2) = 1.98e-6; Ms(2) = 1714; label{2} = 'Fe'; % Fe
A(3) = 2.81e-6; Ms(3) = 1422; label{3} = 'Co'; % Fe
A(4) = 1.07e-6; Ms(4) = 813; label{4} = 'Ni_{80}Fe_{20}'; % Ni80Fe20
A(5) = 2.395e-6; Ms(5) = 1880; label{5} = 'Co_{55}Fe_{45}'; %
Co55Fe45
% a1 is the near-neighbor (lattice) spacing [cm]
a1(1) = 0.2942e-7; % Ni, [cm]
a1(2) = 0.2482e-7; % Fe, [cm]
a1(3) = 0.2507e-7; % Co, [cm]
a1(4) = 0.3392e-7; % Ni80Fe20, [cm]
a1(5) = 0.2852e-7; % Co55Fe45, [cm]
col = {'b','m','c','r','k'};
% mat_idx = 1;
% for mat_idx = 1:5
for mat_idx = [1, 4, 5]
Length = 10000e-7; % [cm]
% Diam = 40e-7; % [cm]
for Diam = [40, 50, 70, 100, 150]*1e-7
% Aspect ratio
c = Length/2; a = Diam/2; m = c/a; % m > 1 ! see model
% m = 2:1:600;
% Case of prolate spheroid!
%       Na       =       4*pi*m./(2*(m.^2-1)).*(m-1./(2*sqrt(m.^2-
```

```
1)).*log((m+sqrt(m.^2-1))./...
% (m-sqrt(m.^2-1))));
% % disp(['Na = ' num2str(Na)])
% Nb = Na;
% % disp(['Nb = ' num2str(Nb)])
Nc    =    4*pi*1./(m.^2-1).*(m./(2*sqrt(m.^2-1)).*log((m+sqrt(m.^2-
1))./...
 (m-sqrt(m.^2-1)))-1);
% disp(['Nc = ' num2str(Nc)])
RSD = @(rsd,Nc,i) sqrt(6*A(i)/(Nc*Ms(i)^2)*log(2*rsd/al(i)-1))-rsd;
rsd = (1:1:200e3)*1e-7; % guess!
r = zeros(1,length(Nc));
for i = 1:length(Nc)
[~, idx] = min(abs(RSD(rsd, Nc(i), mat_idx)));
r(i) = fzero(@(rsd) RSD(rsd, Nc(i), mat_idx),rsd(idx));
end
if length(Nc) > 1
 loglog(m, r/1e-7, col{mat_idx}, 'DisplayName', label{mat_idx});
hold on
% semilogy(m, r/1e-7, col{mat_idx}, 'DisplayName', label{mat_idx});
hold on
% plot(m, r/1e-7, col{mat_idx}, 'DisplayName', label{mat_idx}); hold
on
else
 disp([label{mat_idx} ': m = ' num2str(m,'%.1f') ' (c = '...
 unitForm(c/1e-7,'n','m',2) ', a = ' unitForm(a/1e-7,'n','m',2)...
 '), r_sd = ' unitForm(r/1e-7,'n','m',2)])
end
end
end
% xlabel('aspect ratio m = c/a')
```

```
% ylabel('r_{sd} (nm)')

% legend('show','location','best')

toc
```

Table 1: Magnetic quantities and units. To obtain the values of quantities in SI the corresponding CGS values should be multiplied with the conversion factors. [Cullity 2009]

Quantity	Symbol	CGS	SI	Conversion factor
Magnetic induction	**B**	G	T	10^{-4}
Magnetic field intensity	**H**	Oe	A m^{-1}	$10^3/4\pi$
Magnetization	**M**	erg G^{-1} cm^{-3} *or* emu cm^{-3}	A m^{-1}	10^3
Magnetic polarization	**J**	–	T	–
Magnetic moment	m	erg/G (≡ emu)	J T^{-1} (≡ A m^2)	10^{-3}
Susceptibility (volume)	χ	–	–	4π
Magnetic permeability	μ	G/Oe	H m^{-1}	$4\pi \times 10^{-7}$
Relative permeability	μ_r	–	–	1
Magnetic constant (vacuum permeability)	μ_0	G/Oe	H m^{-1}	$4\pi \times 10^{-7}$